NASA Grant NAGW-5224

Final Report

- Title: Inversion Schemes to Retrieve Atmospheric and Oceanic Parameters from SeaWiFS Data

- Principal Investigator: Robert Frouin, Scripps Institution of Oceanography, University of California San Diego, 9500 Gilman Drive, La Jolla, CA 92093-0221; Voice Tel.: 619/534-6243; Fax tel.: 619/534-7452; Internet: rfrouin@ucsd.edu

-Associate Investigator: Pierre-Yves Deschamps, Laboratoire d'Optique Atmosphérique, Université des Sciences et Technologies de Lille, 59655 Villeneuve d'Ascq, France

- Period: October 01, 1996-September 30, 1997

Abstract

Firstly, we have analyzed atmospheric transmittance and sky radiance data collected at the Scripps Institution of Oceanography pier, La Jolla during the winters of 1993 and 1994. Aerosol optical thickness at 870 nm was generally low in La Jolla, with most values below 0.1 after correction for stratospheric aerosols. For such low optical thickness, variability in aerosol scattering properties cannot be determined, and a mean background model, specified regionally under stable stratospheric component, may be sufficient for ocean color remote sensing from space. For optical thicknesses above 0.1, two modes of variability characterized by Angstrom exponents of 1.2 and 0.5 and corresponding to Tropospheric and Maritime models, respectively, were identified in the measurements. The aerosol models selected for ocean color remote sensing allowed one to fit, within measurement inaccuracies, the derived values of Angström exponent and "pseudo" phase function (the product of single scattering albedo and phase function), key atmospheric correction parameters. Importantly, the "pseudo" phase function can be derived from measurements of the Angström exponent. Shipborne sun photometer measurements at the time of satellite overpass are usually sufficient to verify atmospheric correction for ocean color.

Secondly, we have developed a bio-optical index to estimate phytoplankton pigment concentration from satellite-derived spectral marine reflectance, the Normalized Difference

Phytoplankton Index (NDPI). The NDPI is much less influenced by atmospheric correction errors than classic reflectance ratios, such as R443/R555 or R490/R555. Below 1 mgm^{-3}, the effect of atmospheric correction errors is reduced by a factor of up to 4. Another advantage of the NDPI is its linearity with respect to the logarithm of pigment concentration; there is no need to log-transform the index. Due to phytoplankton type variability, the performance of the NDPI, like that of simple ratios, is degraded. The degradation, however, is similar for all the indices, as shown theoretically and experimentally.

Thirdly, we have educated multi-layered networks to retrieve phytoplankton pigment concentration from satellite-derived spectral marine reflectance at 412, 443, 490, 510, and 555 nm (SeaWiFS wavelengths). Datasets of varied complexity were created, taking into account realistic atmospheric correction errors, radiometric noise, and phytoplankton type variability. The performance of the neural networks was compared to that of classic reflectance ratios. The neural networks provided much better results than the reflectance ratios in the entire range of pigment concentrations considered, 0.03-30 mgm^{-3}. Relative r.m.s. inaccuracies induced by atmospheric correction errors were reduced by a factor of 4-5. For the most complex dataset, (i.e., the dataset that included all error types), the relative r.m.s. inaccuracy was reduced by a factor of 2. Even though optimized for satellite data, the neural networks were tested with SeaBAM data and provided better results than reflectance ratios.

1. Verification of aerosol models

Direct atmospheric transmittance and sky radiance were measured at 440, 670, 870, and 1020 nm at the Scripps Institution of Oceanography Pier, La Jolla during the winters of 1993 and 1994. Additional measurements of atmospheric transmittance were made in 1994 on Catalina Island (about 40 km offshore) and during the CALifornia Cooperative Fisheries Investigation (CALCOFI) 1994 winter cruise. The total and aerosol optical thicknesses, and the spectral dependency of the aerosol optical thickness (Angström coefficient), were derived from the measurements of the direct atmospheric transmittance. The aerosol scattering "pseudo" phase functions, and their spectral dependency between 870 and 1020 nm, were derived from the measurements of the sky radiances at the scattering angles of 60°, 90°, and 120 °. The optical measurements were performed under varied atmospheric conditions and, therefore, in the presence of diversified aerosol types, including maritime, terrestrial, and urban.

This comprehensive data set on aerosol scattering properties was gathered with respect to two specific objectives. The first objective was to validate the selection of aerosol models used in the algorithms for the atmospheric correction of space-based ocean color observations, such as those of the SeaWiFS mission (Gordon and Wang, 1994). The second objective was to identify what type of atmospheric optics measurements should be performed to verify atmospheric correction algorithms.

The analysis of data and aerosol models has provided the following main findings and conclusions:

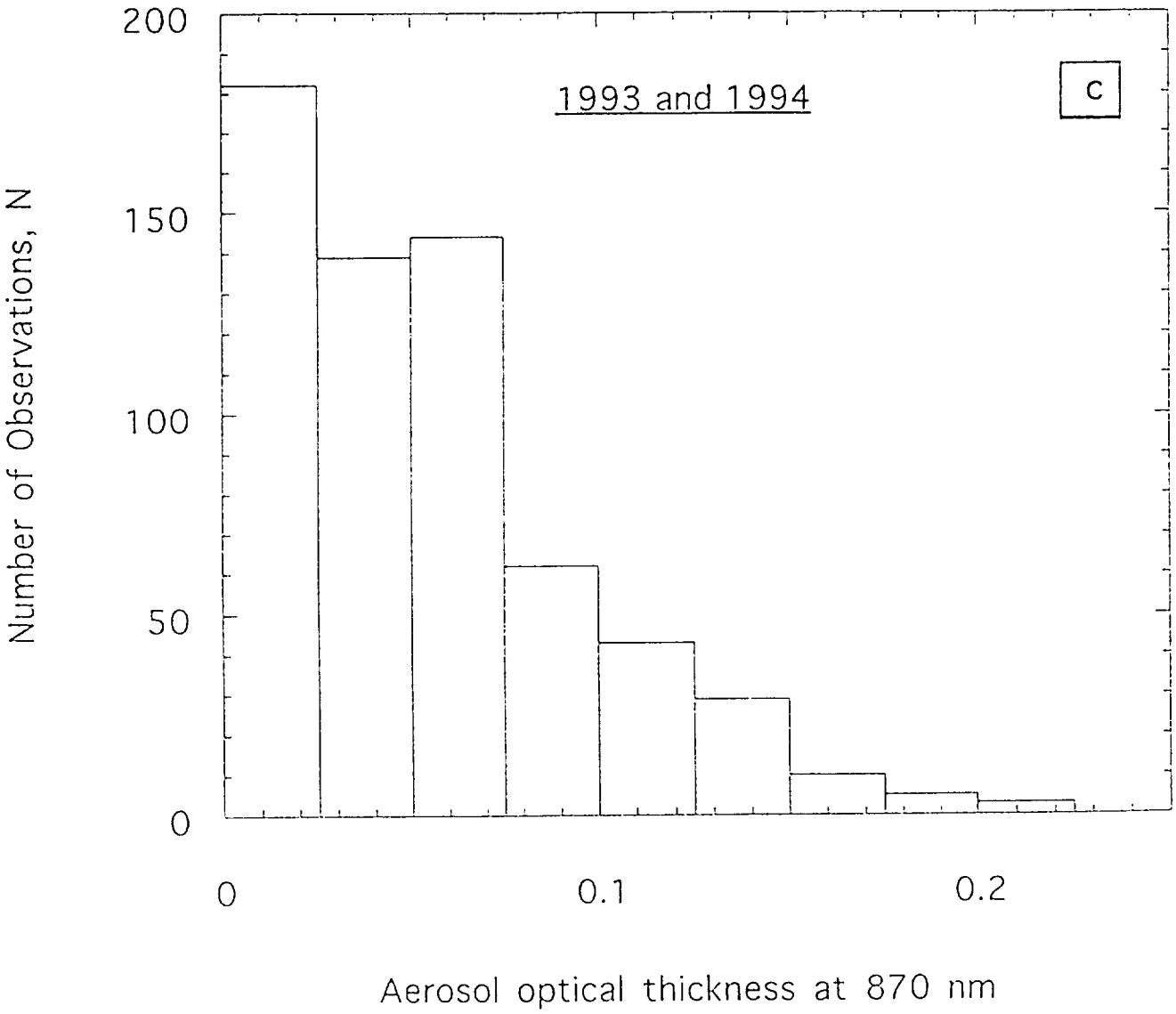

Fig. 1.1 Histogram of the aerosol optical thickness at 870 nm measured at the Scripps Institution of Oceanography pier during the winters of 1993 and 1994. The stratospheric component has been subtracted using SAGE observations.

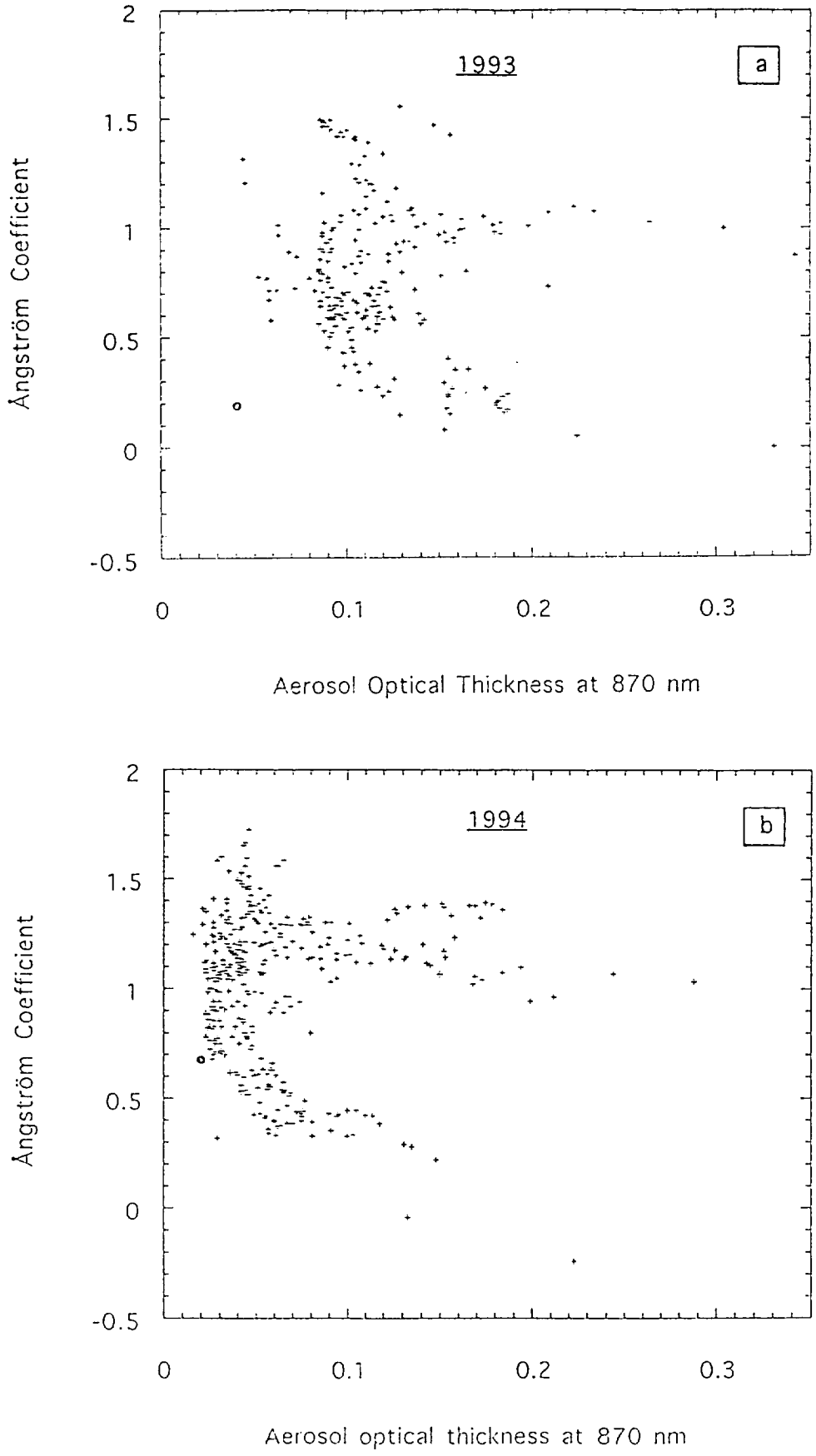

Fig. 1.2 Angström coefficient versus aerosol optical thickness at 870 nm: measurements (crosses collected in a) 1993 and b) 1994. The stratospheric component, given by SAGE data, is identified by a circle.

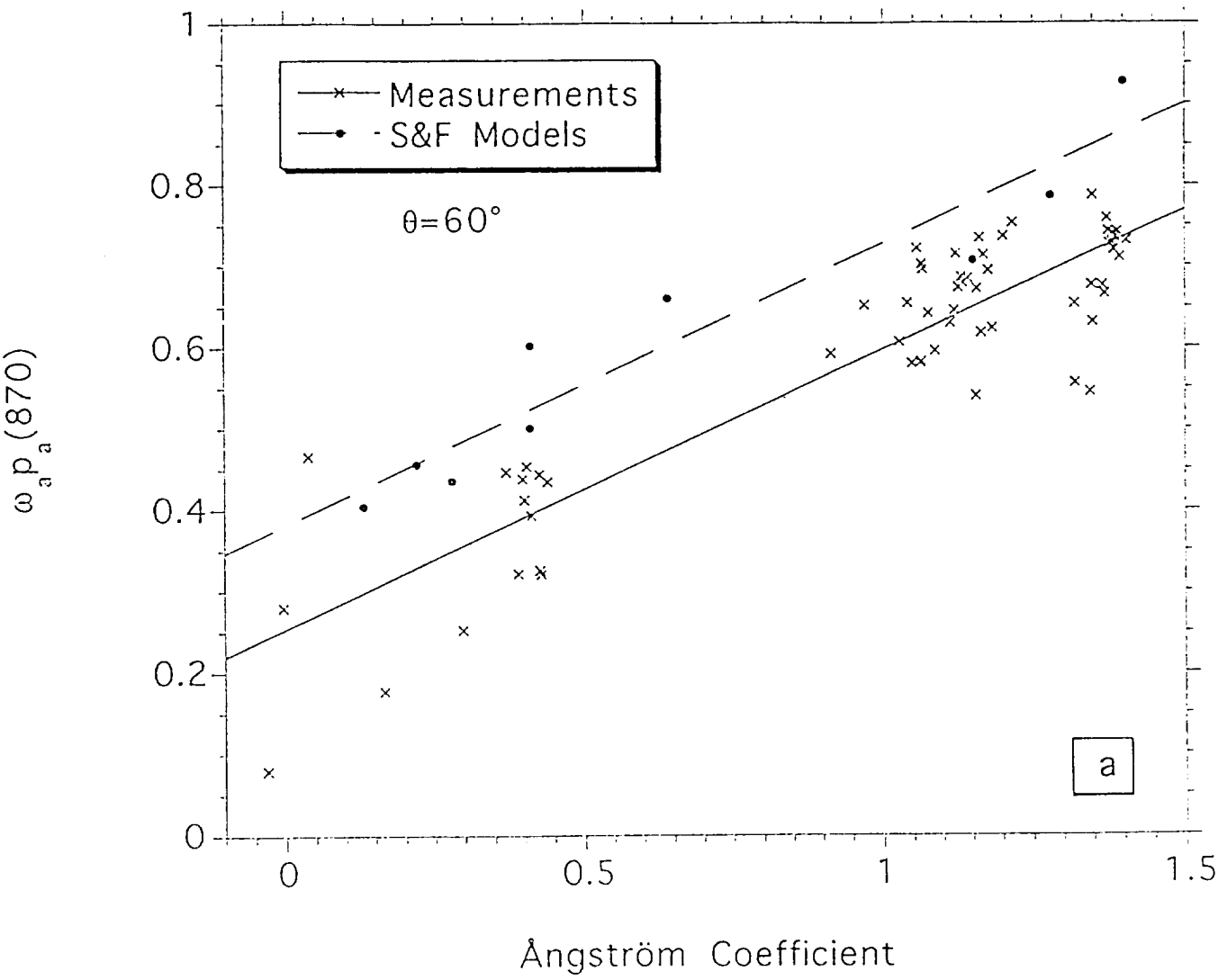

Fig. 1.3 Aerosol "pseudo" phase function versus Angström coefficient: models of Shettle and Fenn (solid circles) and measurements (crosses) at a scattering angle of 60 degrees.

(1) Low aerosol optical thickness, τ_a, has been observed in the study area, consistent with previous measurements over the oceans. The τ_a values are influenced by the stratospheric aerosol content, higher in 1993 than in 1994. After correction of the stratospheric content, most of the τ_a values, i. e. $\tau_{a,tropo}(870)$, are below 0.1 (Fig. 1.1). In such conditions, it is impossible to identify the variability in the aerosol scattering properties, and one has to rely on a mean background model including the stratospheric component in the atmospheric correction algorithms.

(2) Some variability of the aerosol scattering properties has been identified for high optical thickness, i. e. above 0.1 at 870 nm (Fig. 1.2). Two modes can be clearly identified. The first mode has an Angström coefficient, α, around 1.2, corresponding to a Tropospheric model. The second mode has α below 0.5 and tending to 0.2, corresponding to a Maritime model.

(3) Measurements confirm the relationship between "pseudo" phase function and α predicted by the models (Fig. 1.3). The dispersion, however, is larger in the measurements than in the model results. The agreement is not good for the relationship between the spectral dependence of the aerosol reflectance, ε, and α, partly because of the uncertainties in the derived ε values. These findings indicate that, within the accuracy of the measurements, the Shettle and Fenn (1979) models allow one to describe the observations of Angström coefficient and phase function. Additional models bring little more. Furthermore, and importantly from a practical point of view, the phase function can be predicted from measurements of α. Therefore, shipborne measurements of α appear sufficient to validate the aerosol model used in the algorithms. Such measurements were performed during the CALCOFI cruise and they proved reliable.

(4) There is no definite relationship between aerosol characteristics and meteorological conditions, but in some instances, small a values are associated with onshore airflow from the ocean and high a values with offshore flow from the land. Spatial variations of τ_a and α have been observed. In general, τ_a and α are lower offshore than along the coast, suggesting that the atmospheric correction offshore is much simplified.

More details about the study are given in the attached manuscript "Verification of Aerosol Models for Satellite ocean Color Remote Sensing" by Schwindling, Deschamps, and Frouin.

2. Normalized Difference Phytoplankton Index

Bio-optical algorithms to estimate phytoplankton pigment concentration from space, such as those using the ratio of reflectances in the blue and green, have been traditionally developed from in-situ measurements of water-leaving radiance and pigment concentration without consideration of atmospheric correction errors. It has been argued that these errors would somewhat compensate, at least partly, since they would have the same sign in the blue and green. The marine reflectance at 555 or 565 nm, however, is small, especially at low pigment concentrations, and the resulting errors in the reflectance ratios and, hence, pigment concentrations might be large.

a. Effect of Atmospheric correction Errors

To reduce the influence of atmospheric correction errors, we developed a new index, the Normalized Difference Phytoplankton Index (NDPI). The index is defined as (R443-R555)/R490 for SeaWiFS and MODIS and (R443-R565)/R490 for OCTS, POLDER, and GLI. To investigate the sensitivity of the NDPI to atmospheric correction errors, and to compare its performance with that of reflectance ratios, spectral marine reflectance was simulated using the model of Morel (1988), modified for Pope's (1993) water absorption. Realistic atmospheric correction errors of ±0.001 and ±0.002 on the marine reflectance in the blue and propagated to other wavelengths, typical radiometric noise, and uncertainties due to the transformation of above-water marine reflectance into below-water marine reflectance were used in the calculations. A set of about 3,000 points was constructed.

In Figs. 2.1-a through 2.1-c the NDPI and reflectance ratios are displayed as a function of pigment concentration, for atmospheric correction errors of ±0.001 on the marine reflectance in the blue. The NDPI is more linear than the reflectance ratios, which are plotted on a logarithmic scale. For a given reflectance ratio, there is a wide range of pigment concentrations possible below 0.1 mgm^{-3} and above 2-3 mgm^{-3} (Figs. 2.1-a and 2.1-b). For a given NDPI, however, the range of pigment concentrations possible is much reduced below 0.1 mgm^{-3}, suggesting more accurate pigment concentration retrievals using the NDPI (Fig. 2.1-c).

The resulting normalized r.m.s. errors on the pigment concentration are presented in Figs. 2.2-a and 2.2-b for atmospheric correction errors of ±0.001 and ±0.002 on the reflectance in the blue, respectively. At 0.03 mgm^{-3}, the error is reduced by a factor of 4 and 2 when using the NDPI instead of R443/R55 and R490/R555, respectively. At about 1 mgm^{-3}, the normalized r.m.s errors are small (on the order of 10%) and similar for the NDPI and reflectance ratios. This is explained by the values of R443, R490, and R555, which are similar at that pigment concentration, and the correlated errors in the blue and green almost compensate. Thus, the errors are much smaller for the NDPI below 1 mgm^{-3}, and the largest errors are obtained for R490/R555. Above 1 mgm^{-3}, the sensitivity of the various indices to pigment concentration decreases rapidly with increasing pigment concentration, and the atmospheric correction errors become relatively more important at 443 and 490 nm, resulting in large pigment concentration errors (>200% above 8-10 mgm^{-3}).

b. Effect of Phytoplankton Type Variability

To make sure that the NDPI, like the reflectance ratios, reduces adequately variability due to phytoplankton type, the three indices were tested with marine reflectances simulated for varied phytoplankton absorption and scattering coefficients (3,000 cases as before). The scattering coefficient was varied between 0.12 and 0.45, the spectral dependence of the scattering coefficient between 0 and 2, and the absorption coefficient by ±30%. In Fig. 2.3, the resulting normalized r.m.s. error is plotted as a function of pigment

Table 1-a Cubic regression statistics for R443/R555, R490/R555, and NDPI. 277 points acquired during CALCOFI cruises were used in the regressions. The NDPI is defined as (R443-R555)/R490.

Parameter	R443/R555	R490/R555	(R443-R555)/R490
corr. coef., r^2	0.81	0.89	0.84
rms dif. (mgm^{-3})	1.02	0.80	0.95
rel. rms dif. (%)	24.8	24.3	25.2

Table 1-b Same as Table 1-a, but using 565 nm instead of 555 nm (GLI case). 110 points acquired during CALCOFI cruises were used in the regressions. The NDPI is defined as (R443-R565)/R490.

Parameter	R443/R565	R490/R565	(R443-R565)/R490
corr. coef., r^2	0.83	0.86	0.84
rms dif. (mgm^{-3})	0.97	0.86	0.90
rel. rms dif. (%)	34.8	32.8	33.5

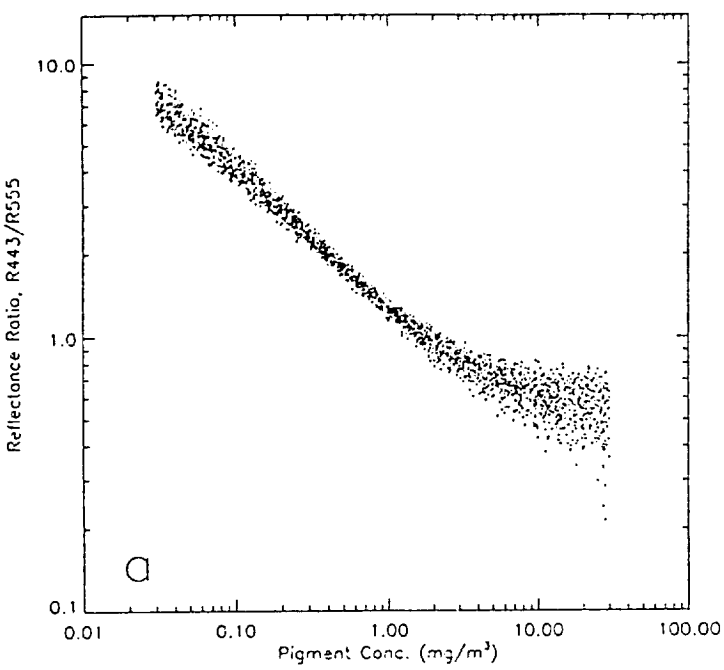

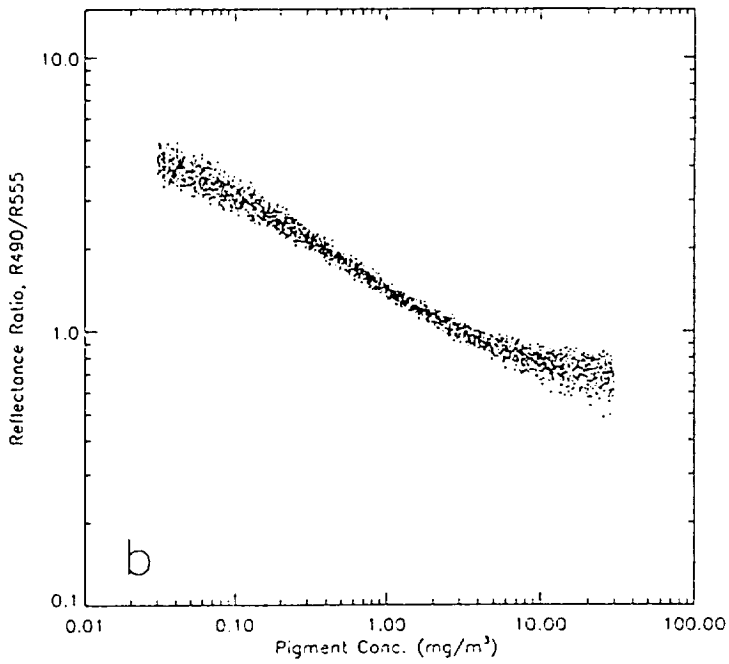

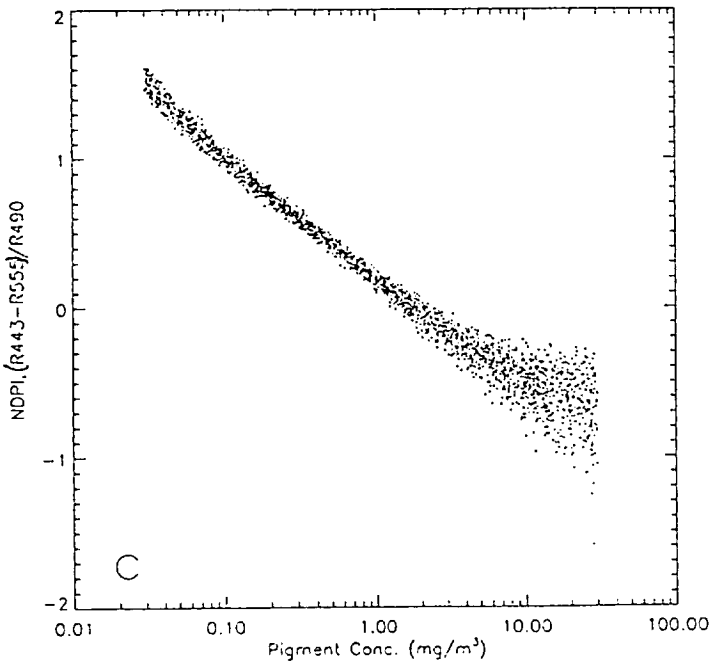

Fig.2.1 Effect of typical atmospheric correction noise (i.e. ±0.001 in the blue) on the R443/R555 and R490/R555 reflectance ratios (a and b, respectively), and NDPI (c).

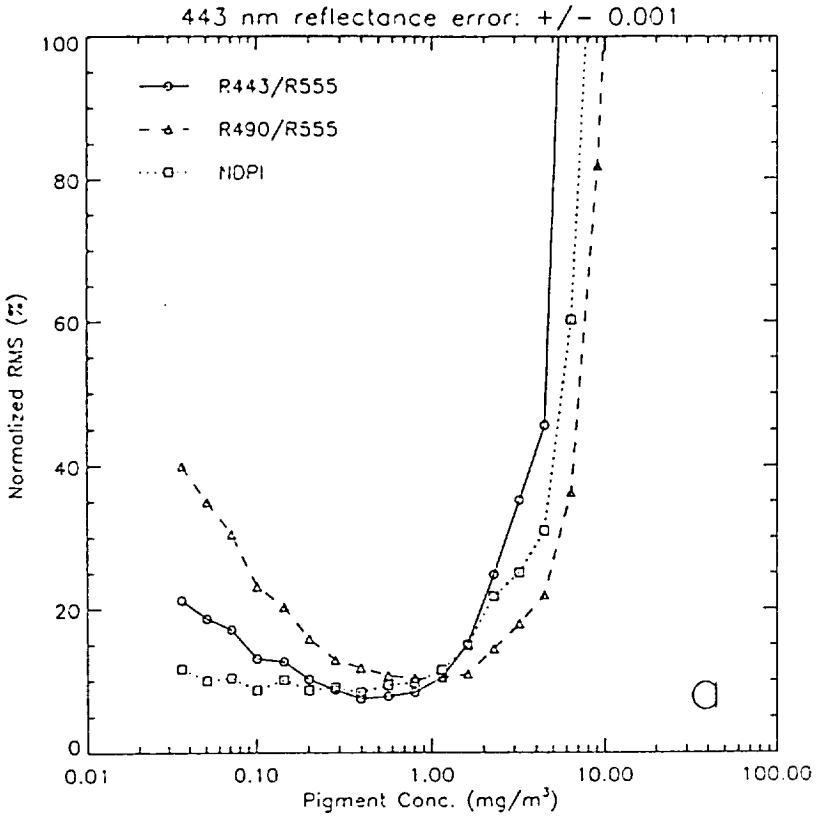

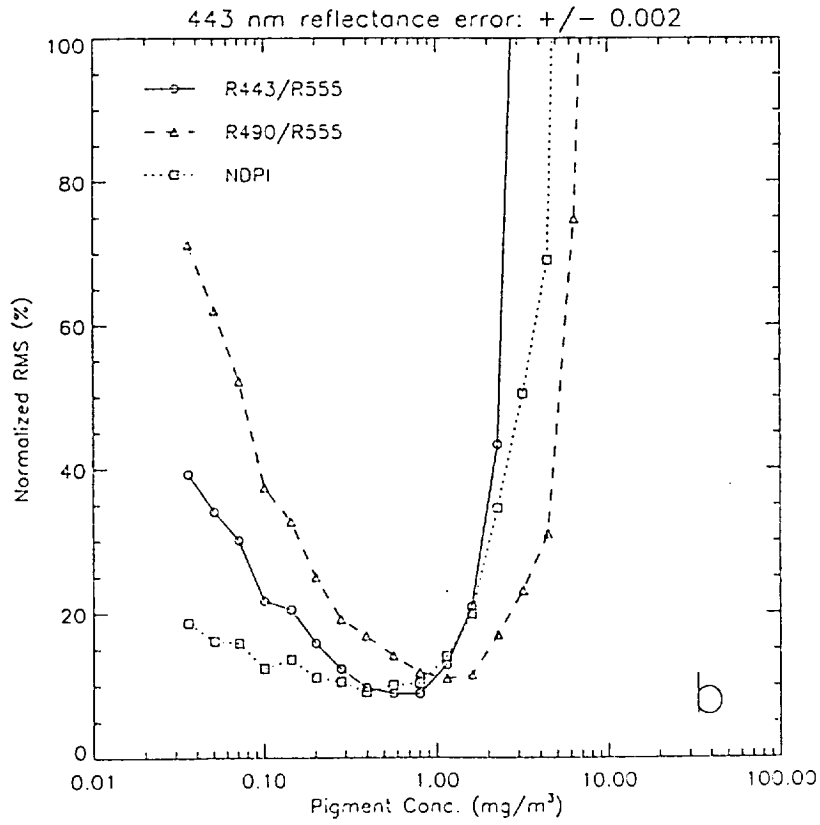

Fig.2.2Relative error on phytoplankton pigment concentration estimates due to atmospheric correction noise for R443/R555, R490/R555, and NDPI. The noise is ±0.001 and ±0.002 on the above-water reflectance in the blue (a and b, respectively).

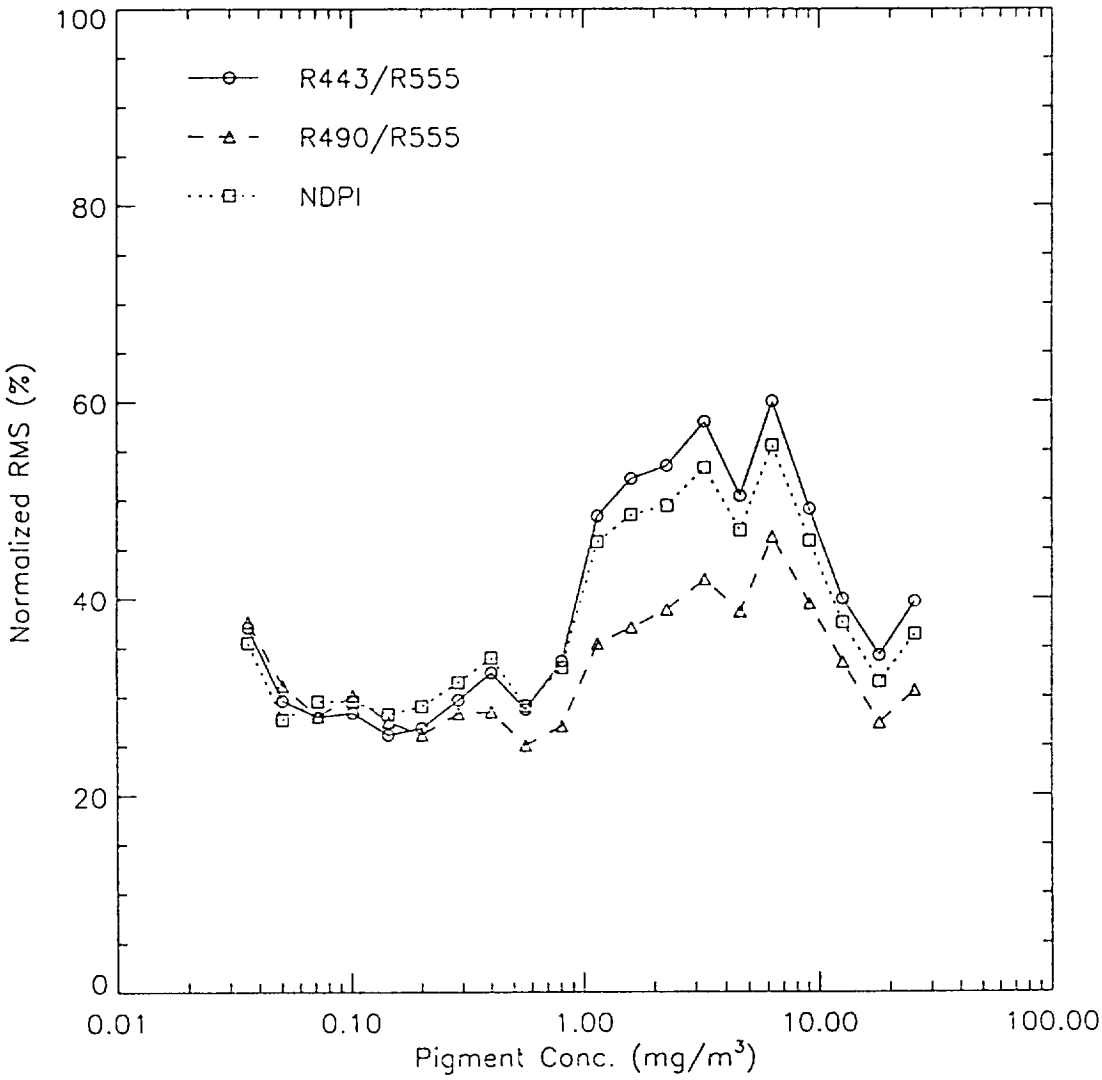

Fig. 2, 3 Relative error on phytoplankton pigment concentration estimates due to phytoplankton type variability for R443/R555, R490/R555, and NDPI.

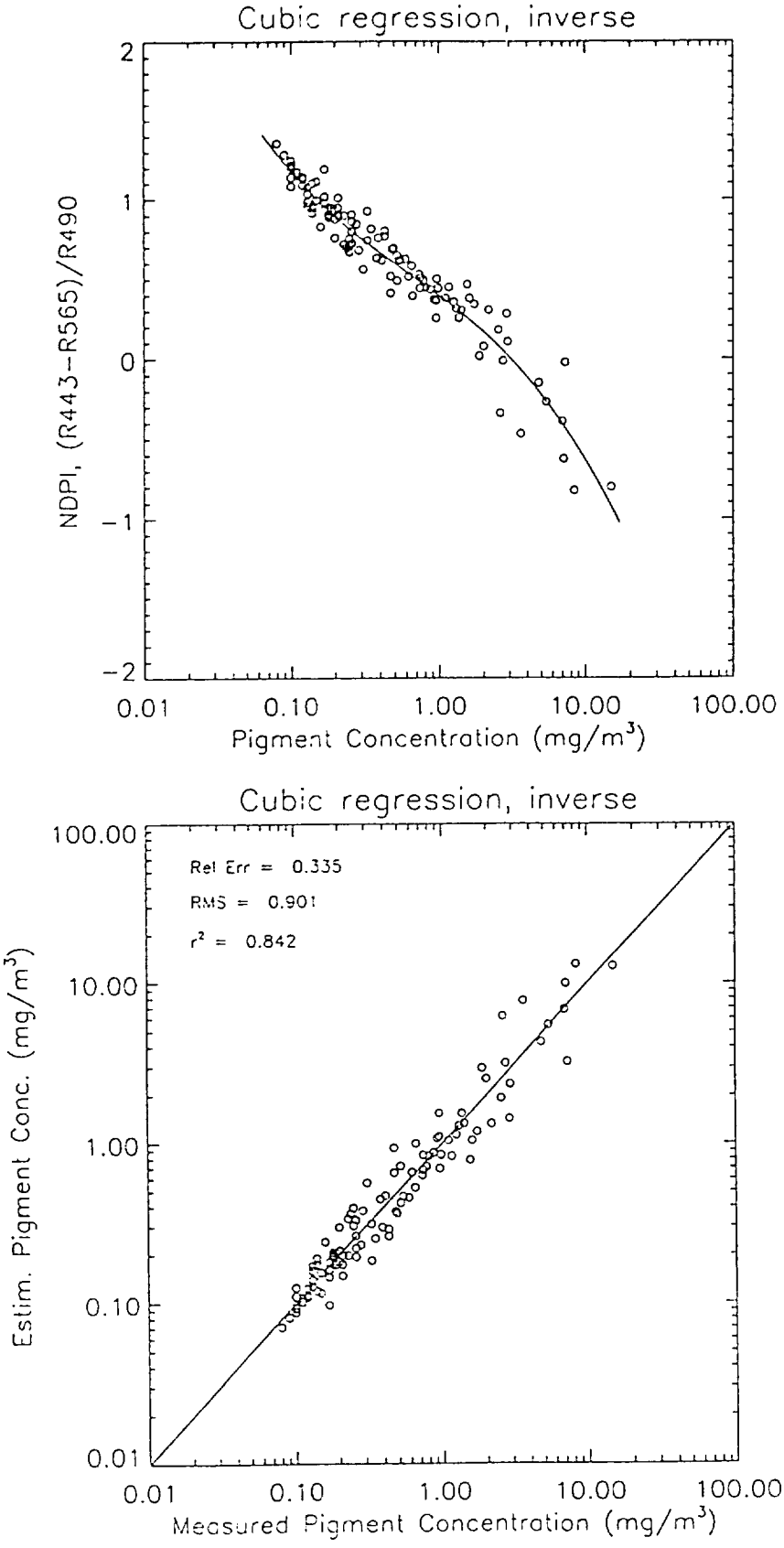

Fig. 2. NDPI versus pigment concentration (top) and estimated versus measured pigment concentration (bottom) for the CALCOFI dataset. Estimates were obtained using NDPI, with NDPI defined as (R443-R565)/R490, i.e. adapted to GLI wavelengths.

concentration. The error is similar for the three indices, except between 1 and 10 mgm^{-3} where the values are lower (35% instead of 50%) for R490/R555. Thus, the NDPI, compared with the reflectance ratio, appears to be similarly sensitive to phytoplankton type, especially below 1 mgm^{-1} (i.e. in most of the oceans).

The three indices were applied to CALCOFI data (marine reflectance, pigment concentration) acquired by Dr. Greg Mitchell and his Group off the California coast during the period August 1993-October 1996. The data were checked for quality, and only the data within boundaries delineated by the probable variability due to phytoplankton type (see previous paragraph) were selected. The performance statistics are summarized in Table 2.1. Cubic regressions were used for all the indices, based on NDPI directly and the logarithm of the reflectance ratios. The relative r.m.s. errors are 25% for all the indices, the correlation coefficients are above 0.8, and the absolute r.m.s. errors are about 1 mgm^{-3}. The performance is slightly better using R490/R555. This confirms the theoretical results on the sensitivity of the indices to phytoplankton type (see Fig. 2.3).

The same type of performance was obtained when using the wavelengths of 443, 490, and 565 (case of OCTS, POLDER, and GLI). The results are summarized in Table 2.1-b. In this case, only 110 points were used to compute the statistical parameters, because less data were collected at 565 nm. The normalized r.m.s. errors are slightly larger than those of Table 2.1-a (33-34%), but this might be due to the smaller number of points (110 instead of 277). Again, the correlation coefficients and absolute r.m.s. errors are similar for the three indices, with slighly better figures for R490/R565. In Fig. 2.4, NDPI is displayed as a function of pigment concentration (top), and estimated pigment concentrations are plotted against measured values (bottom), illustrating the good performance of the NDPI when applied to real data.

3. Neural Networks

a. Neural Network Architecture and Simulated Datasets

Multi-layered neural networks were educated to retrieve phytoplankton pigment concentration from marine reflectances at wavelengths of 412, 443, 490, 510, and 555 nm. These reflectances were computed using the model of Morel (1988) for pigment concentrations ranging between 0.03 and 30 mgm^{-3}. In terms of architecture, the networks had, in addition to the layers receiving the input and broadcasting the output, two intermediate layers (the hidden layers) containing six and four neurons, respectively (Fig. 3.1). Connections only went from lower layers to higher layers, and no connection linked cells within the same layer. This architecture was based on earlier feasibility studies performed by Dr. Carlos Mejia at the University of Pierre and Marie Curie in Paris, France. There are 69 parameters to adjust, since there is an extra neuron to trigger state changes. The weights of the connections were determined using the gradient-back-propagation algorithm.

Five types of datasets were created, varying in complexity (see Table 3.1). The first one (Type 1) included no variability in phytoplankton optical properties (constant bio-

optical model); the second one (Type 2) had a constant bio-optical model, but included atmospheric correction noise; the third one (Type 3) included variability in phytoplankton optical properties (varied bio-optical model), only; the fourth one (Type 4) included both variability in phytoplankton optical properties and atmospheric correction noise; and the fifth one (Type 5) included, in addition to variability in phytoplankton optical properties and atmospheric correction noise, uncertainties in pigment concentration (because this variable is not measured perfectly). For each type of datasets, 5,000 points were used in the learning phase and 3,000 to check/validate the learning phase. The educated neural nets were then applied to a test dataset of 10,000 points.

b. Performance of Neural networks on Simulated Datasets

In Table 3.2 the performance of the neural networks is compared to that of reflectance ratios R443/R555 and R490/R555. The neural networks generally provide much better results than reflectance ratios. For the Type 2 dataset, for example, the relative r.m.s. error is reduce by a factor of 4-5. In other words, the neural network handles very well errors due to atmospheric correction noise. For the most complex dataset (Type 5), the r.m.s. accuracy is reduced by a factor of about 2.

To check the coherence of the various neural networks, each neural network (i.e. educated with one type of data) was applied to all the datasets. The results are displayed in Table 3.3. The r.m.s. errors obtained with Type 2 and Type 3 networks allow one to verify that the residual atmospheric correction noise and the variability due to phytoplankton type are due to distinct processes which both need to be taken into account to build a generally applicable neural network (Type 4 or Type 5). On the other hand, pigment concentration errors appear as a minor problem, since the results obtained with Type 4 and Type 5 networks are similar when these networks are applied to Type 4 and Type 5 data.

c. Test using SeaBAM data

SeaBAM data provided by the SeaWiFS project were used to test the various neural networks, even though the networks were not optimized for in-situ data. The data consisted of sets of marine reflectances at 412, 443, 490, 510, and 555 nm and phytoplankton pigment concentration. The data were acquired in various oceans, but about one third of the data was collected by Dr. Greg Mitchell off the California coast during CALCOFI cruises. Table 3.4 gives the performance of the various neural networks on the data, and Fig. 3.2 gives the scatter plots of estimated versus prescribed pigment concentrations. Surprisingly, the best results are obtained with the network educated with Type 2 data, i.e. data that include atmospheric correction noise, but no phytoplankton type variability (average bio-optical model). This suggests that the atmospheric correction noise in the simulations encompasses the noise in the SeaBAM data, and that the SeaBAM data fit the average bio-optical model. Type 1 network, which does not include noise, does not perform well, indicating that the networks must be educated with noisy data. Type 2 network, when compared to Type 2 reflectance ratios (Fig. 3.3), provide much better results. The large

Test / Model Type	Type 1 distance RMS ($mg.m^{-3}$)	Type 2 distance RMS ($mg.m^{-3}$)	Type 3 distance RMS ($mg.m^{-3}$)	Type 4 distance RMS ($mg.m^{-3}$)	Type 5 distance RMS ($mg.m^{-3}$)
Type 1	0.02	0.09	8.95	8.98	8.98
Type 2	0.29	0.69	6.57	6.62	6.13
Type 3	0.22	11.11	0.44	19.41	19.41
Type 4	1.15	1.71	1.43	1.89	1.93
Type 5	1.00	1.70	1.39	1.90	1.94

Table 3 : RMS errors obtained with the neural networks when applied to various data types (simulated testing datasets). Each line displays the results obtained with one type of network, but different data types.

Bio-optical model

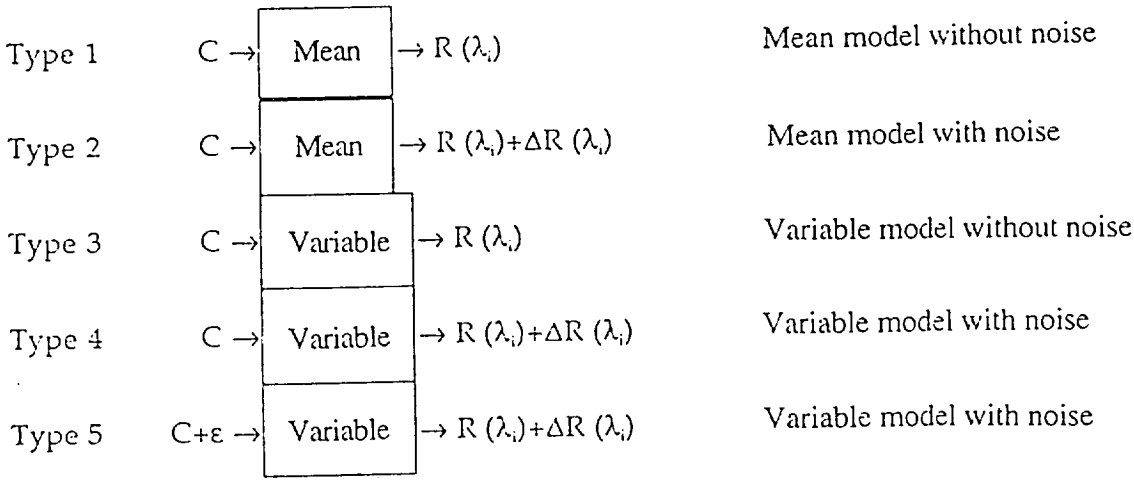

C : Phytoplankton pigment concentration (mgm^{-3})

$R(\lambda_i)$: Spectral marine reflectance

Table 3.2 Characteristics of the simulated datasets.

	Neural Network	R 443/R 555	R 490/R 555
Type 1 Data	RMS : 0.02 $mg.m^{-3}$ RMS rel : 0.14% r^2 : 99.99%	RMS : 1.28 $mg.m^{-3}$ RMS rel : 8.55% r^2 : 97.74%	RMS : 0.83 $mg.m^{-3}$ RMS rel : 5.13% r^2 : 98.98%
Type 2 Data	RMS : 0.69 $mg.m^{-3}$ RMS rel : 5.48% r^2 : 99.41%	RMS : 2.11 $mg.m^{-3}$ RMS rel : 18.43% r^2 : 91.34%	RMS : 1.68 $mg.m^{-3}$ RMS rel : 23.16% r^2 : 94.79%
Type 3 Data	RMS : 0.44 $mg.m^{-3}$ RMS rel : 17.01% r^2 : 99.78%	RMS : 3.25 $mg.m^{-3}$ RMS rel : 40.51% r^2 : 77.39%	RMS : 2.59 $mg.m^{-3}$ RMS rel : 33.32% r^2 : 85.59%
Type 4 Data	RMS : 1.89 $mg.m^{-3}$ RMS rel : 25.84% r^2 : 96.10%	RMS : 3.43 $mg.m^{-3}$ RMS rel : 42.80% r^2 : 75.03%	RMS : 2.80 $mg.m^{-3}$ RMS rel : 39.91% r^2 : 83.64%
Type 5 Data	RMS : 1.94 $mg.m^{-3}$ RMS rel : 26.35% r^2 : 95.83%	RMS : 3.46 $mg.m^{-3}$ RMS rel : 43.08% r^2 : 74.63%	RMS : 2.84 $mg.m^{-3}$ RMS rel : 40.68% r^2 : 83.20%

Table 3.3 Performance statistics of the neural networks and reflectance ratios when applied to simulated testing datasets.

Network Type	RMS (mgm^{-3})	RMS Rel. (%)	r^2
1	2.54	137.93	73.50
2	1.30	39.27	94.58
3	4.82	90.43	51.23
4	2.63	67.71	87.81
5	3.47	82.54	82.97

Table 3.4 Performance statistics of the neural networks when applied to SeaBAM data.

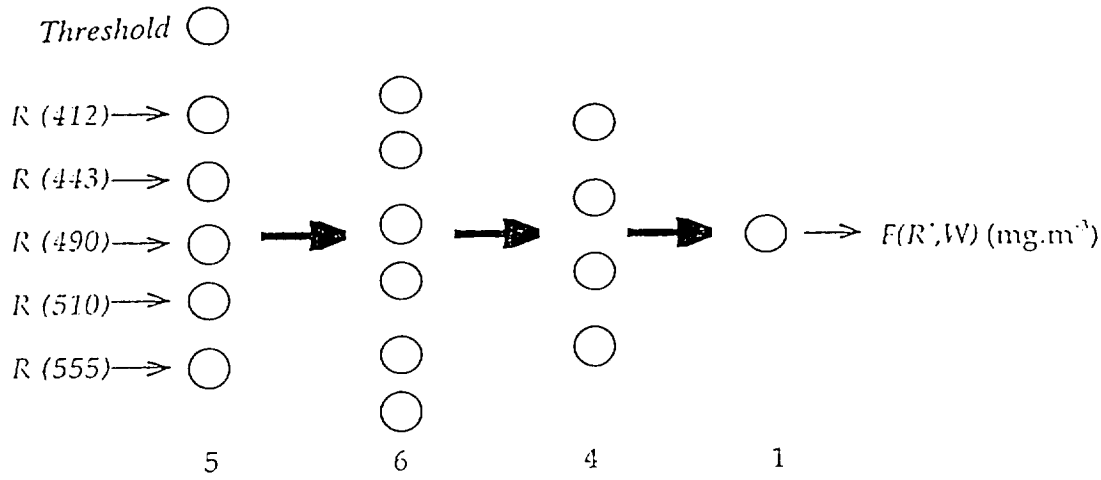

Fig. 3. | Architecture of the neural networks. The input is R at 412, 443, 490, 510, and 555 nm; the output is pigment concentration, C, expressed as a function F of R and the synaptic weights, W.

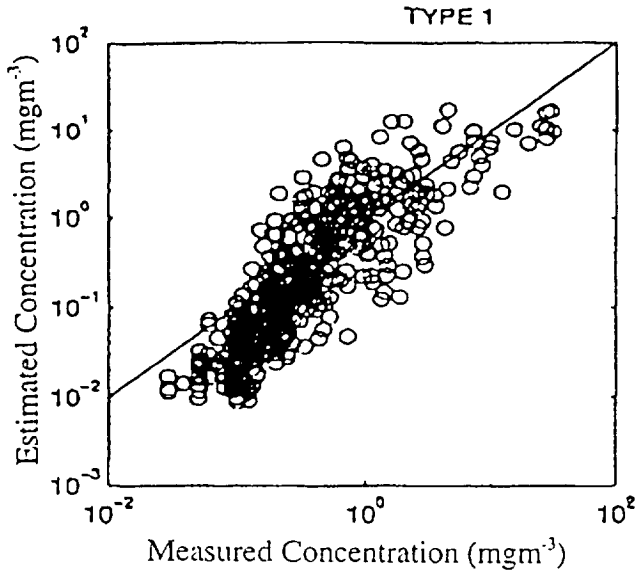

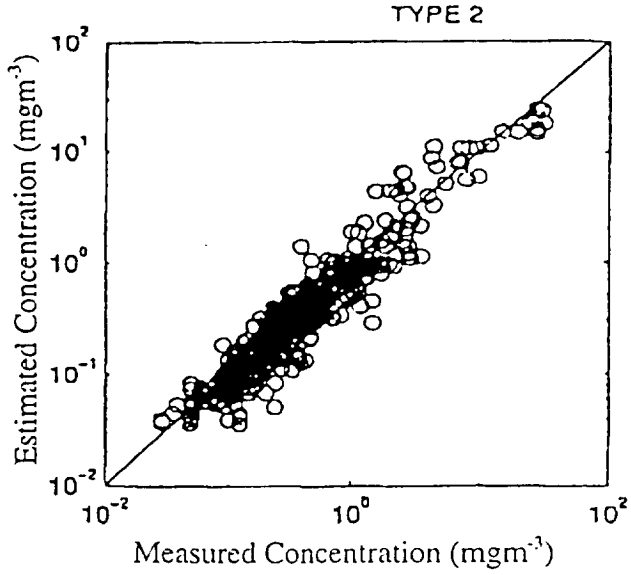

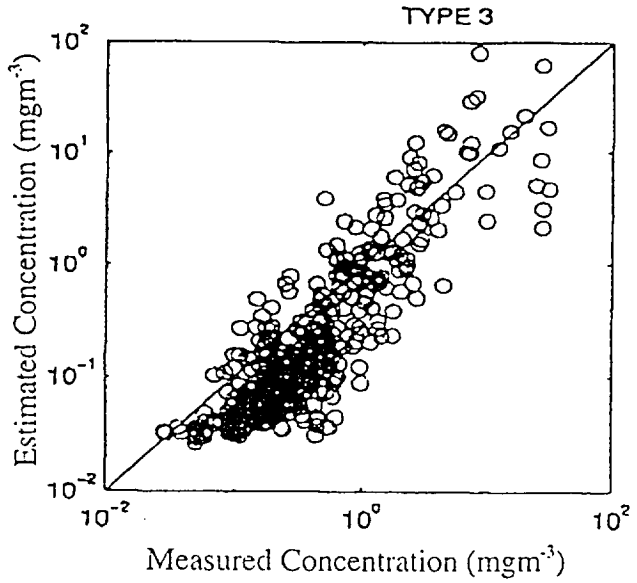

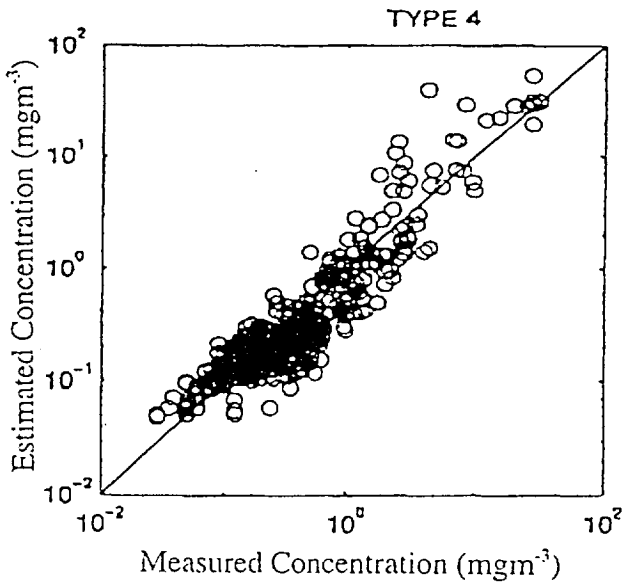

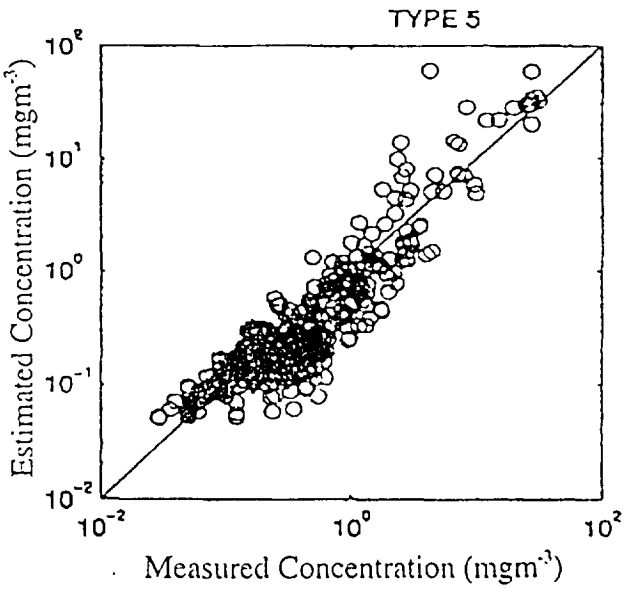

Fig.3.2 Scatter plots of estimated pigment concentration versus measured pigment concentration for the various neural networks applied to SeaBAM data.

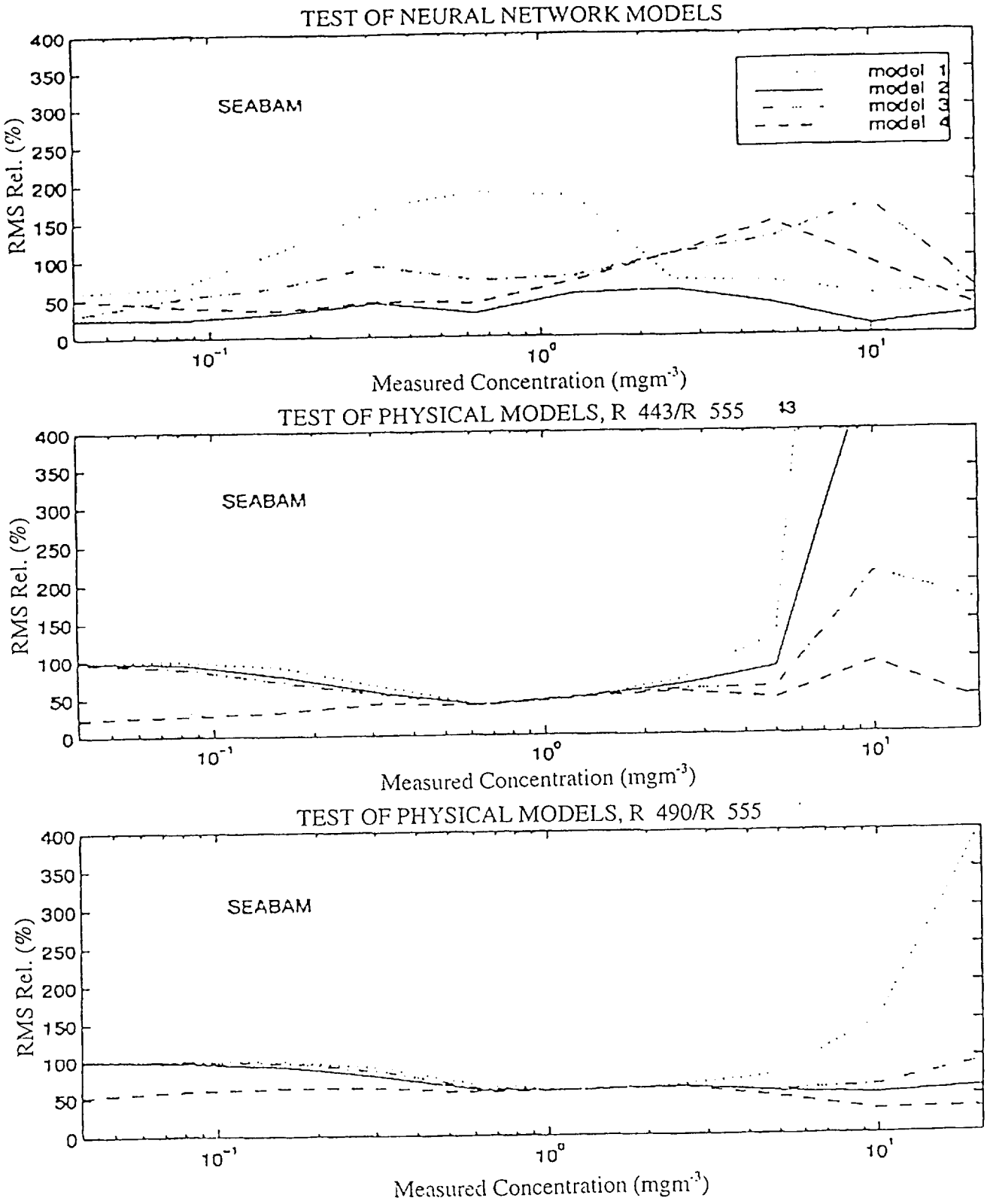

Fig.33 Relative RMS error as a function of pigment concentration for the neural networks and the reflectance ratios when applied to SeaBAM data.

discrepancies obtained with the Type 2 reflectance ratios at low pigment concentrations reflect the great sensitivity of the ratios to atmospheric correction noise. As this noise is not in the data, there is little hope that regressions based on simulations that include atmospheric correction noise would perform well on the data.

One would expect, however, a better performance with Type 4 or Type 5 networks. This is not the case, probably because the variability due to phytoplankton type is not simulated realistically in the Type 4 and Type 5 datasets. In other words, even though the average bio-optical model is included in these datasets, they also contain many unrealistic cases that the neural networks must account for in the learning process, and it might be better to educate the networks with an average model.

4. References

Gordon, H. R., and M. Wang, Retrieval of water-leaving radiance and aerosol optical thickness over the oceans with SeaWiFS: A preliminary algorithm, *Appl. Opt., 33*, 442-453, 1994.

Morel, A., 1988: Optical modeling of the upper ocean in relation to its biogenous matter content (case 1 waters). *J. Geophys. Res.*, 93, 10749-10768.

Pope, R. M., 1993: Optical absorption of pure water and sea water using the integrating cavity absorption meter. Ph.D. thesis, Texas University, College Station, Texas.

Shettle E. P., and R. W. Fenn, Models for the aerosols of the lower atmosphere and the effect of humidity variations on their optical properties, *AFGL-Rep. TR-79-0214*, Air Force Geophys. Lab., Bedford, Mass., 1979.

Appendix

Verification of Aerosol Models for Satellite Ocean Color Remote Sensing

Myriam Schwindling, Pierre-Yves Deschamps
Laboratoire d'Optique Atmosphérique
Université des Sciences et Technologies de Lille
Villeneuve d'Ascq, France

Robert Frouin
Scripps Institution of Oceanography
University of California San Diego
La Jolla, California

JGR-Oceans, PCC-0328, revised

May 1998

Abstract. *Direct atmospheric transmittance and sky radiance were measured spectrally at the coastal site of Scripps Institution of Oceanography Pier in La Jolla, California, during the Winters of 1993 and 1994. Direct atmospheric transmittance was also measured aboard R/V Wecoma and on Catalina Island during the 1994 CALCOFI winter cruise. The data were analyzed to (1) verify whether the aerosol models selected by Gordon and Wang (1994) for SeaWiFS are adequate for ocean color remote sensing from space, and (2) identify what type of in-situ atmospheric optics measurements should be performed to verify atmospheric correction algorithms. Aerosol optical thickness at 870 nm was generally low at La Jolla, with most values below 0.1 after correction for stratospheric aerosols. Values were even lower offshore (R/V Wecoma, Catalina Island), and no systematic correlation was found between aerosol characteristics and meteorological conditions. Sometimes, however, small (respectively high) Ångström coefficient values were associated with onshore airflow from the ocean (respectively offshore airflow from land). At such low optical thickness, variability in aerosol scattering properties cannot be determined, and a mean background model, specified regionally, may be sufficient for ocean color remote sensing from space. For optical thicknesses above 0.1, two modes of variability characterized by Ångström coefficients of 1.2 and 0.5 and corresponding to Tropospheric and Maritime models, respectively, were identified in the measurements. The aerosol models selected by Gordon and Wang (1994) allow one to fit, within measurement inaccuracies, the derived values of Ångström coefficient and "pseudo" phase function (the product of single scattering albedo and phase function), key atmospheric correction parameters. Additional aerosol models bring little more. The relationship between spectral dependence of the aerosol radiances, and Ångström coefficient predicted by the models, is not corroborated by the measurements, because of measurement uncertainties. Importantly, the "pseudo" phase function can be derived from measurements of the Ångström coefficient. This means that shipborne sun photometer measurements at the time of satellite overpass are usually sufficient to verify the atmospheric correction for ocean color.*

1. Introduction

Remote sensing of ocean color from space provides the only means to monitor phytoplankton pigment concentration and primary production on a global scale. Large-scale, long-term information on these parameters is necessary to improve our understanding of biogeochemical (carbon, nutrient) cycles (e. g., Joint Global Ocean Flux Study, JGOFS, 1987; Abbott et al., 1994). However, deriving marine spectral reflectances from top-of-atmosphere (TOA) radiances in the visible and near-infrared is not easy, because of the interference of atmospheric scattering and absorption. Typically, 90 % of the TOA signal is composed of photons that have not interacted with the water body (e. g., Viollier et al., 1980) and, thus, that do not contain information on water composition.

The difficulty of the atmospheric correction problem has been identified early with the Coastal Zone Color Scanner (CZCS), the first space experiment dedicated to ocean color (Hovis et al., 1980; Gordon et al., 1980). CZCS provided data from 1978 through 1986. The next generation of instruments, such as the Sea-viewing Wide Field-of-view Sensor (SeaWiFS) (Hooker at al., 1993; Hooker and Esaias, 1993), will improve the accuracy of the marine reflectance estimates. SeaWiFS has upgraded radiometric performance and additional wavelengths in the near-infrared for more efficient atmospheric correction (Gordon and Wang, 1994). The launch of the Ocean Color and Temperature Scanner (OCTS) and the POLarization and Directionality of Earth Reflectances (POLDER) radiometer (Deschamps et al., 1994) on ADEOS in 1996, of SeaWiFS on SeaStar (Hooker et al., 1993) in 1997, will be followed by the launch of the Moderate Resolution Imaging Spectrometer (MODIS) (Ardanuy et al., 1991) on the Earth Observing System (EOS) AM-1 platform in 1998, the Medium Resolution Imaging Spectrometer (MERIS) (Rast and Bézy, 1995) on ENVISAT in 1999, etc.

Atmospheric correction algorithms attempt to retrieve the actual value of the marine reflectance from TOA measurements. Some atmospheric effects are straightforward to correct, either because they can be computed using auxiliary data, or because they are weak. Molecular scattering is important at shorter wavelengths, but can be computed almost exactly knowing the surface pressure and the value of

the solar constant (Gordon et al., 1988; André and Morel, 1989). Ozone transmission can be computed accurately using an exogen total ozone content. Water vapor transmission is usually negligible in ocean color spectral bands. The concentration and composition of atmospheric aerosols, on the other hand, are highly variable in space and time, and the correction of their effects is a specific problem.

Because of the space and time variability of aerosols, *a-priori* or climatological knowledge of their optical properties is not sufficient to compute accurately their effects on the TOA signal. Aerosol parameters must be known at the time of the ocean color observations, and ideally should be derived from measurements by the same instrument. It was noted early that aerosol scattering behaved in first approximation like the product of optical thickness, single scattering albedo, and scattering phase function (Tanré et al., 1979), resulting in a smooth spectral dependence of the scattered radiance in the visible and near-infrared for the most common aerosol models. The general concept of the aerosol correction algorithm, therefore, is to observe the aerosol scattered radiance in the near-infrared where the marine reflectance is negligible, and to extrapolate the signal to the wavelengths in the visible (Viollier et al., 1980; Gordon and Clark, 1980).

Application of this type of algorithm to CZCS data has been limited because the only band usable for atmospheric corrections, close to the near-infrared, was centered at 670 nm in the red. One had to (1) assume a given aerosol type and spectral dependence of the aerosol scattered radiance, and (2) to restrict the processing to ocean cases where the marine reflectance at 670 nm could be neglected (Gordon et al., 1983). At least two measurements in the near-infrared at wavelengths above 700 nm are necessary to determine correctly the spectral dependence of the aerosol radiance and the aerosol type. From these measurements, the correction for aerosol scattering can be extrapolated to shorter wavelengths, either analytically (Deschamps et al., 1983) or with the help of aerosol models, as proposed by Gordon and Wang (1994).

The choice of aerosol models to guide the spectral extrapolation of aerosol radiance raises two main questions, which both require in-situ measurements:

(1) Are the models representative of aerosol conditions encountered ocean-wide?

(2) What type of in-situ measurements should be made to verify the atmospheric correction algorithm, i. e. to evaluate its performance?

In-situ atmospheric optics measurements are not easy to perform at sea, from a ship or any platform. A few sunphotometer measurements have been reported (Tomasi and Prodi, 1982; Hoppel et al., 1990; Korotaev et al., 1993; Villevalde, 1994), and they have provided information on aerosol optical thickness and its spectral variations in the various oceans. More extensive measurements have been made from land-surface sites to characterize tropospheric and stratospheric aerosol components (Bruegge, 1992; Herber et al., 1993; O'Neill et al., 1993; Smirnov et al.; 1994; Dutton et al., 1994; Kent et al., 1994), including coastal sites (Obleitner, 1992). Only a few studies address the problem of observing sky radiance, thus the path radiance in the backward direction, at a scattering angle corresponding to space observations (Kaufman, 1993; Kaufman et al., 1994).

To provide answers to the above questions (representation of the models, type of in-situ measurements), one needs to acquire atmospheric optics data under sufficiently varied aerosol conditions. The data should be collected prior to the launch of the ocean color instruments, so that recommendations and conclusions can be acted upon during the operational phase of the missions. It was our main motivation to establish, before the launch of SeaWiFS, the next ocean color sensor, a permanent atmospheric optics station on a coastal site in Southern California. The measurements were performed systematically during the winters of 1993 and 1994. The measured or directly derived physical variables included spectral aerosol optical thickness and sky radiance at wavelengths used in ocean color remote sensing, i. e. in the range 0.4 - 1 μm.

2. Background

2.1 . Atmospheric correction algorithms

The ocean color sensor measures the solar radiation reflected by the ocean-atmosphere system, namely the TOA radiance, L_i, in spectral bands centered at wavelength λ_i. For convenience, we will work with the spectral reflectance, ρ_i, i. e.

the spectral radiance, L_i, normalized by the solar spectral irradiance outside the atmosphere, E_{si}, and corrected for earth-sun distance variations:

$$\rho_i = \pi L_i / \mu_s E_{si} \quad (1)$$

where μ_s is the cosine of the solar zenith angle, θ_s. In the remainder of the paper, we will omit the wavelength index i whenever possible. The TOA reflectance can be modeled as the sum of several contributions:

$$\rho = \rho_w + \rho_m + \rho_a + \rho_f + \rho_g + \text{coupling terms} \quad (2)$$

where ρ_w is the contribution of scattering by the water body (the signal to be retrieved), ρ_f is the contribution of foam at the surface, ρ_g is the contribution of sun glint, and ρ_m and ρ_a are the contributions of scattering by air molecules and aerosols, respectively. Coupling terms result from multiple interactions between two or more of these individual contributions; they can be either neglected or computed knowing the aerosol model. We will assume that the measurements are made outside the directions contaminated by sun glint and, therefore, we will neglect ρ_g. We will also neglect ρ_f, though ρ_f cannot be neglected at wind speeds above 10 ms^{-1} (Estep and Arnone, 1994; Frouin et al., 1996). The atmospheric correction algorithm works on ρ_m and ρ_a. The molecular scattering reflectance, ρ_m, is easy to compute accurately, knowing the molecular thickness of the atmosphere, a function of the atmospheric pressure at sea level. The aerosol scattering reflectance, ρ_a, on the other hand, depends on the aerosol amount and type, parameters that are eminently variable in time and space, and ρ_a has to be estimated from the measurements themselves.

The first generation of atmospheric correction algorithms, applied to CZCS (Gordon et al. 1980), assumed that the aerosol reflectance, $\rho_a(\lambda)$, varied with wavelength according to the following power law:

$$\rho_a(\lambda) \sim \lambda^{-n} \quad (3)$$

This assumption was supported by the fact that, using the single scattering approximation, ρ_a can be expressed as:

$$\rho_a(\lambda) \cong \varpi_a(\lambda)\, \tau_a(\lambda)\, p_a(\theta_s,\theta_v,\varphi, \lambda) / 4\, \mu_s\, \mu_v \quad (4)$$

where the subscript a refers to scattering by aerosols, ϖ_a is the single scattering albedo, τ is the optical thickness, p is the scattering phase function, μ_v is the cosine of the viewing zenith angles, θ_v, and φ is the relative azimuth angle between solar and viewing directions. The scattering phase function and the single scattering albedo vary weakly with wavelength. The wavelength dependence of the aerosol reflectance $\rho_a(\lambda)$, therefore, is very similar to that of the aerosol optical thickness $\tau_a(\lambda)$, often given as a power law:

$$\tau_a(\lambda) \sim \lambda^{-\alpha} \quad (5)$$

where the exponent α is the Ångström coefficient (Ångström, 1961 and 1964), close to the exponent n in Eq. (3).

The CZCS had six spectral bands, five in the visible and near-infrared (centered at 443, 520, 550, 670 and 750 nm) and one in the thermal infra-red (10.5 to 12.5 μm). Only the first four channels had a good radiometric sensitivity and could be used for observation of ocean color. The first CZCS algorithm used the 670 nm channel to estimate $\rho_a(670)$ assuming a "black" ocean, $\rho_w(670) \cong 0$. The value of $\rho_a(670)$ was then extrapolated to the other wavelengths, with n corresponding to a mean aerosol model. In order to adapt the algorithm to different aerosol types, the clear-water radiance concept was developed and applied to CZCS data in the open ocean (Gordon and Clark, 1981). At low chlorophyll concentrations, $\rho_w(520)$ and

$\rho_w(550)$ are known with enough accuracy, so that not only $\rho_a(670)$, but also $\rho_a(520)$ and $\rho_a(550)$ can be derived, leading to a self determination of the wavelength dependence, hence the exponent n. Thus, in the clear ocean case, the CZCS algorithm could accommodate for variability of both aerosol loading and type, but the solution was limited and not optimum.

A major improvement of the atmospheric correction resides in the capability of next instruments like SeaWiFS to observe in the near infra-red and determine more independently the aerosol reflectance at 765 and 865 nm, with no reference to the clear-water concept. On the larger SeaWiFS spectral range, 412 to 865 nm, however, the approximation of Eq. (3) is now not accurate enough (Gordon and Wang, 1994) primarily because its generality is affected by multiple scattering and coupling terms. A new generation of atmospheric correction algorithms, based on aerosol models, has therefore been proposed by Gordon and Wang (1994) (see also Gordon, 1997).

Schematically, Gordon and Wang (1994) proposed first to compute exactly the radiative transfer in the ocean-atmosphere system for a set of reference aerosol models. Then, the wavelength dependence of the aerosol scattering is derived using the measurements in the near-infrared at 765 and 865 nm, and the (two) closest aerosol models are determined. Eventually, the aerosol correction at ocean color wavelengths is estimated by interpolation between the exact solutions for the two aerosol models and applied to the measurements. Multiple scattering is fully accounted for in this algorithm, but the algorithm relies strongly on the choice of the aerosol models. Gordon and Wang (1994) used 9 reference aerosol models, namely the Shettle and Fenn (1979) Maritime and Tropospheric models with a humidity variation of the aerosol optical properties and a Coastal aerosol model, actually a mixing of the Maritime and Tropospheric models. The humidity is set at 70, 90, and 98 %. These models may or may not be realistic. Shettle and Fenn (1979) developed their models using samples of aerosols for which they derived the optical characteristics. In atmospheric corrections, we are more interested by the optical behavior of the aerosols through the entire atmosphere.

2.2 . Aerosol models

Various sets of aerosols models have been proposed to compute the radiative transfer in the earth-atmosphere system, under varied geophysical conditions, for climate as well as remote sensing studies. They include the "Haze-type" models of Diermeidjan (1969), the models of Shettle and Fenn (1979), and the models of the World Meteorological Organization (WMO, 1986) (see description below). Particular applications have required other developments such as the global average model developed by Toon and Pollack (1976), to be used as input in global average radiative transfer calculations. The basic components and size distribution of this model vary with altitude and are supposed to represent an average of the most common aerosol conditions over the world. D'Almeida et al. (1991) established a global climatology of aerosols. They used the models of Shettle and Fenn (1979) and of WMO (1986) after some revisions and additions, namely a polar aerosol model, a desert aerosol model, and a "mixed aerosols" model. Nilsson (1979) developed a model with variable size distribution and refractive index depending on relative humidity.

The models of Shettle and Fenn (1979) hereafter referred to as the S&F models, and of WMO (1986) are based on the work of Shettle and Fenn (1976, 1979), who used ground-based as well as aircraft measurements of concentration, size distribution, and optical properties of tropospheric aerosols. Both types of models are mixtures of basic components referred to as "water soluble" and "dust-like", which are representative of mid-latitude soils, "soot-like", which results from combustion and industrial sources, and "oceanic", which is composed of sea water injected in the atmosphere by the wind. The main differences between the S&F and WMO models are in the relative amount and the way the components are mixed. In the case of the WMO models, Mie theory is applied to each component to compute the optical parameters. The size distribution is a log-normal law. These optical parameters are mixed to obtain the final aerosol models. In the case of the S&F models, the size distribution is a log-normal law with one or two modes applied to the mixtures of the basic components described above. The size distribution and the refractive index of the basic components both are altered by relative humidity. The mode radius of the size distribution, not its width, is

changed with relative humidity according to the work of Hänel (1976). As a result, Shettle and Fenn (1979) give an equivalent refractive index for specific relative humidities of 50 %, 70 %, 80 %, 90 %, 95 %, 98 %, and 99 %, as well as tables of scattering and absorption coefficients obtained from Mie scattering computations in the spectral range 0.2 - 40 μm.

As indicated in the previous section, the models selected by Gordon and Wang (1994) for the atmospheric correction of SeaWiFS data are the S&F Tropospheric and Maritime models for relative humidities of 70 %, 90 %, and 98 %. The Maritime models are actually the Tropospheric models with the addition of sea salt aerosols. Gordon and Wang (1994) add three additional Coastal models that contains half the fraction of sea salt aerosols of the Maritime models.

The phase functions at 870 nm for specific scattering angles of 60, 90, and 120° are given in Table 1, along with the single scattering albedo and the Ångström coefficient characterizing the wavelength dependence of the aerosol optical thickness between 400 and 1000 nm, for the WMO models and the nine S&F models selected by Gordon and Wang (1994) (Tropospheric, Maritime, and Coastal with humidities of 70, 90, and 98 %, referred to as T70, T90, T98, M70, M90, M98, C70, C90, and C98, respectively). For the WMO models, the Ångström coefficients vary from 0.22 (Maritime model) to 1.32 (Urban model). For the Maritime, Coastal, and Tropospheric S&F models, the variations are similar, from 0.10 to 1.46. Fig. 1 gives the scattering phase functions at 870 nm of the Continental, Urban, and Maritime WMO models, and four of the S&F models selected by Gordon and Wang (1994), namely Tropospheric and Maritime with humidity of 70 and 98 %, which represent extreme cases. Examining the S&F models, we see a general tendency, as we go from the small and dry particles of the T70 model to the large water particles of the M98 model, to decrease the Ångström coefficient, and the scattering phase function around 90°. Minima of the scattering phase functions are observed at angles 90-120° and are well marked below 0.1 for the aerosols of Maritime type. The WMO Maritime model is very similar to the S&F M90 model. The WMO Continental model is close to the S&F T70 model, but with comparatively smaller Ångström coefficient (α = 1.18) and larger absorption (ϖ_{0a} = 0.842). The WMO Urban model is an extreme model characterized by small particles, large scattering phase function,

large absorption (ϖ_{0a} = 0.591). If we exclude this last model the range of models selected by Gordon and Wang (1994) fits the range of the WMO models.

The physical quantity observed from space is the radiance at a scattering angle between 45° and 180°. To interpolate the aerosol signal from one wavelength λ_i, to another wavelength, λ_j, the useful parameter is the ratio of the aerosol reflectances, $\varepsilon(\lambda_i,\lambda_j)$, at these two wavelengths:

$$\varepsilon(\lambda_i,\lambda_j) = \rho_a(\lambda_i)/\rho_a(\lambda_j) \tag{6}$$

To compute the aerosol reflectances, we can use as a first approximation the single scattering approximation given by Eq. (4). This gives for $\varepsilon(\lambda_i,\lambda_j)$:

$$\varepsilon(\lambda_i,\lambda_j) \cong \varpi_{0a}(\lambda_i)\,\tau_a(\lambda_i)\,p_a(\theta_s,\theta_v,\varphi,\lambda_i) \,/\, \varpi_{0a}(\lambda_j)\,\tau_a(\lambda_j)\,p_a(\theta_s,\theta_v,\varphi,\lambda_j) \tag{7}$$

Note that Gordon and Wang (1994) include a surface reflection component in their definition of ε. Using Eq. (7) is appropriate for the purpose of the study, since we are analysing ground-based measurements (no surface effects). Fig. 2 displays ε(870,1020) as a function of the scattering angle for five S&F models (T70, T98, M70, M98 and C70) and three WMO models (Continental, Maritime and Urban) at 870 nm. We chose the wavelengths of 870 and 1020 nm because our measurements of aerosol reflectance are accurate at these wavelengths (see section 3.2). The mean value of ε(870,1020) roughly corresponds to the ratio of the optical thickness at 870 and 1020 nm, not shown on Fig. 2. The curves show little variations with geometry, except in the backward direction for the Maritime models.

2.3. Previous atmospheric optics measurements

a) Sun intensity

A radiometer with a small field-of-view for viewing the sun measures the intensity of direct solar radiation, thus the direct atmospheric transmittance. The aerosol optical thickness is derived after correcting the measurements for molecular scattering and absorption. Historically, the measurements have been made in broad spectral bands. More accurate measurements of the aerosol optical thickness are now performed in narrow spectral bands corresponding to atmospheric windows. The spectral measurements give the aerosol optical thickness and its spectral dependence, allowing one to derive the classical turbidity factors, namely the optical thickness normalized at the wavelength of 1 μm, β, which is directly related to the aerosol loading, and the Ångström coefficient, α, which characterizes the wavelength dependence and, thus, the aerosol type. The measurements were made initially in the visible and later extended to the near- and short-wave infrared, allowing more complex retrieval of the aerosol type. Ground-based sun photometer measurements have been widely performed to characterize the tropospheric and stratospheric aerosol components (see references in the introduction section).

b) Solar aureole

More information can be obtained from solar aureole observations, i. e. measurements of the sky radiance at forward scattering angles, typically less than 30°. Schematically, the aureole technique is sensitive to large particles (> 1 μm), while the Ångström coefficient is more sensitive to small particles (< 1 μm). The inversion of the two types of measurements, aureole and optical thickness, gives at least two modes of the aerosol size distribution (Nakajima et al., 1983 and 1986, Tanré et al., 1988). It is difficult, however to retrieve the refractive index from aureole measurements. So far, there has been no published report of solar aureole measurements at sea, although they have been attempted (Nakajima, personal communication). The main limitation is due to the severe requirements on platform stability, which must be maintained to better than 0.1° in three directions.

c) Sky radiance

Because of its remote sensing significance, the scattering phase function in the backward direction at angles between 90° to 180° has been measured directly.

This approach is better, at least in principle, than computing the phase function from the derived aerosol model; but accurate measurements from the ground are difficult to make at large scattering angles. Low elevations for the sun and the direction of observation are required, which restricts the measurements possible during the day. More importantly, multiple scattering increases rapidly at low elevation, limiting the accuracy of the scattering phase function retrieval. As a result, it is generally inaccurate to observe at angles above 150°. Also, the atmosphere may not be homogeneous between solar and viewing directions. Systematic observations at various time and locations (over land) have only been reported at the angle of 120° (Kaufman, 1993, and Kaufman et al. , 1994), an angle close to the minimum of the scattering phase function where it is very sensitive to the aerosol model (see models above). Like solar aureole, sky radiance is difficult to measure at sea, and no measurements over the ocean have been reported in the literature.

3 . Material and Methods

Extensive time series of atmospheric optics data were acquired during the winters of 1993 and 1994 (January through early March) at a coastal site, the Scripps Institution of Oceanography (SIO) Pier in La Jolla, California. The measurements included direct atmospheric transmittance in order to derive the aerosol optical thickness, and sky radiance to be interpreted in relation to the aerosol scattering phase function, and they were performed in the spectral range 440 to 1020 nm. To investigate the spatial variability of the atmospheric optical properties, measurements of direct atmospheric transmittance were also performed at other sites during a few days in January 1994. The other sites were located on Catalina Island off Long Beach, California and along the R/V Wecoma ship track during the 1994 CALifornia COoperative Fisheries Investigation (CALCOFI) winter cruise in the Southern California Bight.

3.1. Instrumentation

a) Description

The instrument used to investigate aerosol optical properties was a sun photometer-sky radiometer system developed by CIMEL Electronique (Holben et al., 1994). This instrument measures the direct atmospheric transmittance at 1020, 870, 670, 440 nm, and in additional bands located in the 940 nm water vapor absorption region. These additional bands were not used in this study. Sky radiance is also measured at 1020, 870, 670 and 440 nm. All the bands are 10 nm wide and the field of view is 1.2°. The CIMEL instrument, when taking sky radiance measurements, was used in a semi-automatic mode, i. e. the sky was scanned automatically at 40 different scattering angles. The angles of interest for our study were mainly 60, 90 and 120 degrees. The sun photometer-sky radiometer was installed at the end of the SIO Pier, in order to be as much as possible under marine conditions and to minimize coastal effects (ground reflectance influence). The measurements (sky radiance, atmospheric transmittance) were performed under clear sky conditions, generally from sunrise to sunset. The instruments used during the CALCOFI cruise and on Catalina Island were portable sun photometers also designed by CIMEL Electronique, but to perform optical thickness measurements at 1020, 870, 670 and 440 nm only.

Meteorological data were collected to correct the optical measurements and help with the analysis. They included wind speed, wind direction, and surface atmospheric pressure, measured every five minutes on the SIO Pier, and air and dew point temperatures have been measured hourly at several meteorological stations located in the San Diego area. The SIO Pier data and other meteorological data were made available by SIO staff and the National Center for Atmospheric Research, respectively.

b) Radiometric calibration

The automatic CIMEL instrument operating in sky radiance mode was calibrated in the field using a total irradiance plaque of known reflectance properties. The measurements were performed in very clear atmospheric conditions at Stevenson Peak (altitude: 1896 m), Laguna Mountains, California, on January 16, 1994. The sky-radiometer was viewing vertically the calibration plaque

placed horizontally. This method was also performed on the SIO Pier, during very clear days, for instance on January 29, 1994, and the results were in good agreement with those obtained in Laguna Mountains. Calibration of the CIMEL instrument operating in sun mode and of the hand-held CIMEL instruments was also performed on January 16, 1994 at Stevenson Peak, but using the Bouguer-Langley method.

For the radiance calibration, the downward irradiance on the plaque, including the contribution of photons that had interacted with the surface and the atmosphere, was computed using the successive orders of scattering code of Deuzé et al. (1989) and measurements of the aerosol optical thickness at the calibration site. Some assumptions were made about the type of aerosol and ground reflectance. Knowledge of these parameters is not critical, however, considering the low optical thickness of the aerosols and the fact that only a small fraction of photons reflected by the ground reached the scattering plaque.

Two additional radiance calibrations were performed in the laboratory on July 1993 and April 1994 using an integrating sphere of well-known leaving radiance. The results of these two types of calibration as well as the results of the Stevenson Peak and SIO Pier calibrations are presented in Table 2 for the two different gains used in the observation of sky radiance, "S" (Sky) for scattering angles of more than 6 degrees, and "A" (Aureole) for scattering angles of less than 6 degrees.

There is a good agreement between the calibration coefficients obtained with these two very distinct methods, field and laboratory (less than 10% in all cases except at 670 nm where there may have been a degradation of the filter between July 1993 and January 1994). The agreement is best between results on January 16, 1994, and April 1994 (most favorable conditions). The calibration coefficients obtained on-site (January 16 and 29, 1994) agree to within 1 %, but are lower than the coefficients obtained in the laboratory. The difference may be due to the decreasing performance of the lamps of the scattering sphere, which was not taken into account. On the other hand, the assumption made about aerosol type may introduce an error in the computation of the on-site calibration coefficients. Our results, however, are sufficiently accurate for the purpose of the study.

3.2 . Data processing

a) Aerosol optical thickness retrieval

An aerosol optical thickness is derived from the measurements of direct solar radiation after correction of gaseous processes, namely ozone absorption and molecular (Rayleigh) scattering. First, the direct atmospheric transmittance, T, is obtained from the sun intensity, measured by the sun photometer, I, by solving the following equation:

$$I = I_0 \, (D_0 / D)^2 \, T \qquad (9)$$

where I_0 is the sun intensity outside the atmosphere, actually the constant derived from the calibration after extrapolation to an airmass m = 0, and D and D_0 are the Sun-Earth distances on the days of the measurements and of the calibration, respectively. Then, T is corrected for atmospheric gas absorption. In the spectral range used for our measurements, the only band strongly affected by the absorption of gases is that centered at 670 nm (absorption by ozone). The total ozone content has been obtained from TOMS (Total Ozone Monitoring Sensor) data and was highly variable during the campaign. In the Winter of 1994, the total ozone content during the measurement days ranged from 0.287 atm.cm on January 10 to 0.353 atm.cm on February 19. In the Winter of 1993, the minimum was 0.247 atm.cm and the maximum 0.335 atm.cm. We noticed an increase of the total ozone content from the beginning to the end of the winter during the two years of campaign. Ozone absorption was computed using the Simulation of Satellite Signal in the Solar Spectrum (5S) code (Tanré et al., 1989).

At 1020 nm, the sensitivity of the detector is strongly affected by ambient temperature. For each measurement of sky radiance or direct transmission, the temperature of the detector was also measured. A correction was applied in order to take into account detector temperature variation between the day of calibration and the days of measurements.

The sun-earth distance factor D is computed according to Paltridge and Platt (1977):

$$D(J) = 1 - e \cos(0.017201\ (J - 4)) \tag{9}$$

where J is the Julian day, and e = 0.01673 is the eccentricity factor. The next step is to write:

$$T = \exp(-m\tau) \tag{10}$$

where m is the airmass and τ is the total (i. e. aerosols and molecules) atmospheric optical thickness. The airmass m has been computed according to Kasten and Young (1989):

$$m(\theta_s) = 1 / (\cos\theta_s + a\ (\theta_s + b)^{-c}) \tag{11}$$

with a=0.50572 and b=6.07995 for θ_s expressed in degrees, and c=1.6364. The aerosol optical thickness, $\tau_a(\lambda)$, is derived eventually by subtracting the Rayleigh optical thickness, $\tau_r(\lambda)$, from the total optical thickness, τ. The Rayleigh optical thickness is taken following Travis and Hansen (1974) and Gordon et al. (1988), but for a depolarization factor of 0.0279:

$$\tau_r(\lambda) = (\ 0.008524\ \lambda^{-4} + 0.0000963\ \lambda^{-6} + 0.0000011\ \lambda^{-8}\ )\ P / P_0 \tag{12}$$

where P is the surface atmospheric pressure, actually measured at SIO Pier, and P_0 = 1013.25 hPa is the standard atmospheric pressure.

The Ångström coefficient, α, is determined as the slope of a linear regression, on a log-log scale, between $\tau_a(\lambda)$ and λ, for the four wavelengths of the measurements, 440, 670, 870, and 1020 nm. Experimental results of such a regression are given in Fig. 3, for different values of the aerosol optical thickness. In Fig. 3 one

notices that the determination of α becomes more difficult at low aerosol optical thickness, simply because the errors on the derived $\tau_a(\lambda)$ are rather constant in absolute value, and then become increasingly important in relative value.

b) Aerosol scattering phase function retrieval

The aerosol phase function is derived from the measured sky radiances at given angles. First, for convenience, the sky radiance is converted in sky reflectance, ρ, according to Eq. (1). Second, the Rayleigh reflectance, ρ_r, is computed exactly for a pure molecular atmosphere using the successive orders of scattering code of Deuzé et al. (1989). In the computations, the Rayleigh optical thickness is given by Eq. (12), and the Rayleigh phase function is taken with a depolarization factor of 0.0279 according to Young (1981). Third, the Rayleigh reflectance is subtracted from the sky reflectance to derive an aerosol reflectance, ρ_a, using:

$$\rho_a = \rho - \rho_r \tag{13}$$

Finally the phase function, p_a, at the scattering angle θ of the observation, is derived from the aerosol reflectance, using the classic single scattering approximation (Tanré et al., 1979; Gordon et al., 1983):

$$\rho_a = \varpi_a \tau_a p_a(\theta) / 4 \mu_s \mu_v \tag{14}$$

Actually, the single scattering albedo, ϖ_a, remains unknown, and it is the product $\varpi_{0a} p_a$ which is derived and hereafter referred to as the "pseudo" phase function.

Eq. (14) is the first order of the development at low optical thickness of the exact single scattering formulation, given by, at the top of the layer, for observations from space:

$$\rho_a = \varpi_a p_a(\theta) \{ 1 - \exp[-\tau_a (1/\mu_s + 1/\mu_v)] \} / 4 (\mu_s + \mu_v) \tag{15}$$

or, at the bottom of the layer, for ground-based observations:

$$\rho_a = \varpi_a p_a(\theta) \{ 1 - \exp[-\tau_a (1/\mu_s + 1/\mu_v)] \} \exp(-\tau_a/\mu_v)/ 4 (\mu_s + \mu_v) \qquad (16)$$

Eq. (14) overestimates the single scattering effect and may be a good estimation of the multiple scattering effect (Tanré et al.; 1989). It is rather accurate at 870 and 1020 nm where the coupling term between aerosols and molecules is negligible. Because of the attenuation term $\exp(-\tau_a/\mu_v)$ in Eq. (16), we tested an alternative approximation for ρ_a at the bottom of the layer, with attenuation through the layer:

$$\rho_a = \varpi_a \tau_a P_a(\theta) \exp(-\tau_a/\mu_v)/ 4 \mu_s \mu_v \qquad (17)$$

Radiative transfer simulations were made to test the validity of Eqs. (14) and (17) for ground-based observations. The simulated atmosphere was a mixture of molecules and aerosols, with respective scale heights of 8 and 2 km, and a flat water surface at the bottom. The simulations were made at 870 nm for two of the above described models (Tropospheric with a relative humidity of 70 %, T70, and Maritime with a relative humidity of 98%, M98), two aerosol optical thicknesses of 0.1 and 0.2, and two solar zenith angle, 39.9° and 80.7°. An aerosol "pseudo" phase function was then derived from the simulation, using Eq. (14) or Eq. (17), after subtracting the Rayleigh scattering.

The actual and derived "pseudo" phase functions of aerosol models T70 and M98, are plotted on Figs. 4a and 4b, for $\tau_a = 0.1$ and two solar zenith angles, $\theta_s = 39.9°$, and 80.7°, respectively. Eq. (17) underestimates ρ_a because it includes a too large exponential attenuation, and leads to a systematic overestimation of the derived phase function in the backward directions. Eq. (14) gives far better results particularly at large scattering angles; but its accuracy is rapidly degraded at viewing zenith angles above 75°, for both solar zenith angles. For $\theta_s < 75°$, the worst case is

observed for the Maritime model M98, which gives a relative error of 10 and 20 % in the range of scattering angles 100-120°. The accuracy of Eq. (14) is limited by its ability to represent multiple scattering for such a phase function presenting a well marked minimum.

Tables 3a and 3b summarize for the above described conditions the exact and deduced "pseudo" aerosol phase function at a scattering angle of 60° as well as the relative error ([deduced - exact] / exact) induced by the approximations at 870 and 1020 nm, respectively. The relative error varies with the model and geometry, and increases roughly like the aerosol optical thickness representing the ratio of multiple (second order) to single scattering. At the other scattering angles, 90° and 120° (not shown here), aerosol scattering is lower and multiple scattering is dominated by aerosol-molecule scattering interactions. In this range of scattering angles, the ratio of multiple to single scattering depends on the molecular optical thickness but not on the aerosol optical thickness. As a result the relative error on the retrieval of the phase function is rather constant with optical thickness at large scattering angles and varies only with solar zenith angle and aerosol type.

4. Results

4.1. Aerosol optical thickness and Ångström coefficient frequencies

The aerosol optical thickness at 870 nm and Ångström coefficient have been derived from the 4 spectral measurements of the direct atmospheric transmission made by the CIMEL instrument in bands centered at 440, 670, 870, and 1020 nm. The measurements were performed systematically when the sky could be considered as clear, actually when the cloud cover was estimated to be one tenth or less, allowing for sky radiances measurements in the principal plane. When several measurements were made within 15 minutes, the derived aerosol optical thicknesses at 870 nm and Ångström coefficients were averaged. Twenty five (25) and thirty four (34) days of data were acquired during the periods January 23-March 11, 1993, and January 7-March 9, 1994, respectively.

Figs. 5a and 5b present the frequency histograms of the aerosol optical thickness at 870 nm, $\tau_a(870)$, during 1993 and 1994. More than 50 % of the observed optical thicknesses are about 0.1 or less. The values of $\tau_a(870)$ in 1993 are slightly higher than in 1994. This simply illustrates the influence of stratospheric aerosols. According to the SAGE II observations during the period following the eruption of the Pinatubo volcano, the stratospheric optical thickness at 870 nm, $\tau_{a,strato}(870)$, had a mean value of respectively 0.04 and 0.02 during the 1993 and 1994 winters (see Table 4, courtesy of Brogniez, 1995). After subtraction of the stratospheric component, one may deduce the tropospheric component of the aerosol optical thickness, $\tau_{a,tropo}(870)$, which is presented on Fig. 5c. Most of the values of $\tau_{a,tropo}(870)$ are below 0.1.

As detailed below (section 5), the accuracy of the aerosol optical thickness retrieved from the measurements is a few 10^{-3}. The stratospheric aerosol contribution derived from SAGE data is known with an accuracy of better than 0.005, which represents the dispersion of the measurements acquired in the vicinity of La Jolla (Table 4).

The aerosol variability must be analyzed in terms of not only its load, represented by its optical thickness, but also of its type , represented by the Ångström coefficient. In Figs. 7a and 7b are displayed scatter plots of Ångström coefficient versus aerosol optical thickness for the measurements made in 1993 and 1994. They confirm the previous analysis. At low optical thickness the measurements tend to a limit which should be the sum of stratospheric and background tropospheric aerosol components. This limit appears better defined in 1994, with $\tau_a = 0.03$ and α around 1.2.

The Ångström coefficient of the stratospheric component is also well known from the SAGE experiment (see Table 4). Values of α_{strato} are lower in 1993 than in 1994. This is explained by the post-Pinatubo conditions in 1993, with large particles injected by the eruption into the stratosphere. The estimated stratospheric conditions are indicated by a solid circle in Fig. 6.

The inaccuracy of the derived Ångström coefficient, also discussed below, (section 5) increases when τ_a decreases, roughly like $1/\tau_a$. Typical errors are 0.2 when τ_a = 0.1, 0.4 when τ_a = 0.05, and 1 when τ_a = 0.02. This illustrates the difficulties in estimating accurately the Ångström coefficient at low optical thickness. Accordingly, at the lowest optical thicknesses, i. e. at $\tau_a < 0.1$, the values of the derived Ångström coefficient are widely spread all over the geophysical range of possible values, 0 to 1.5. Thus the discussion about aerosol types is limited at low optical thickness. It is only at aerosol optical thickness above 0.1 that some trends in the Ångström coefficients and, thus, aerosol type are detectable. For both years, when τ_a increases, one identifies two modes in Fig. 6: one with α around 1.2, which would correspond to a tropospheric model, and the other with α around 0.2, which would correspond to the maritime model.

The relationship between Ångström coefficient and meteorological variables (wind speed and direction, relative humidity) has been examined, using measurements performed during the most turbid days (aerosol optical thickness above 0.1 at 870 nm). A correlation was found between Ångström coefficient and east-west component of the wind, but only in the presence of established or sustained winds. In these conditions, low Ångström coefficients (<0.8) are associated with westerly flow and high coefficients (>0.8) with easterly flow. When wind speed is low (<2 ms^{-1}), however, the Ångström coefficient is variable, and the correlation with wind direction is not significant. Also, the data did not show a clear relationship between Ångström coefficient and relative humidity, a factor of aerosol growth and, therefore, an indicator of particle size. Even though relationships between aerosol optical variables and meteorological variables may be found, they are not general, presumably because atmospheric changes (vertical mixing, diurnal breeze effects) may result in varied combinations of maritime, continental, and urban aerosols at the SIO Pier.

Regarding spatial variability, aerosol optical measurements made concomitantly at the SIO Pier, on Catalina Island, and in the Southern California Bight during a two-week period starting in late January 1994 (CALCOFI winter cruise) have been analysed. R/V Wecoma was at least 200 km offshore during clear

days, except on January 28 (80 km). Optical thickness was always low (τ_a<0.07 at 870 nm) on Catalina Island, located about 40 km off the mainland, and most of the time lower than optical thickness at the SIO Pier. The highest values were measured on January 20, 1994, the day of highest aerosol load (τ_a of 0.15-0.2 at 870 nm) at the SIO Pier. The highest value measured onboard R/V Wecoma is 0.055, and it was obtained on January 29. The Ångström coefficient often was very low (<0.2) at the R/V Wecoma location, which is consistent with the predominance of maritime aerosols, and generally lower on Catalina Island than at the SIO Pier. On January 29, however, Ångström coefficients of about 1.2 were observed about 240 km from the coast, indicating the presence of aerosols of continental origin. Thus on some occasions, the influence of the continent and coastal urban areas may be felt far offshore.

4.2. Sky radiances

a) Phase function and Ångström coefficient

Phase functions derived from the sky radiance measurements at 870 nm were computed using the procedure described in section 3. This procedure implies some simplifications: a single scattering approximation for the expression of the aerosol radiance is used, the ground effect is neglected, and the result is actually the product of the phase function and the single scattering albedo ("pseudo" phase function). The analysis has been restricted to the morning data, before local noon, to minimize the ground effect: at scattering angles of 90° and 120 °, the atmospheric path is above the ocean surface, and, therefore, the reflection from the land is reduced (but not negligible). Because the retrieval of both the "pseudo" phase function and the Ångström coefficient are increasingly inaccurate as the aerosol optical thickness decreases, the analysis has only been applied to observations involving an aerosol optical thickness above 0.075 at 870 nm.

As shown by the models of S&F, as well as those of WMO, there is a tendency for the phase function to decrease around its minimum at about 100°, when the Ångström coefficient decreases (see Table 1 and Fig. 1 a and 1 b). This is the classical

result of increasing the size of the particles whatever the refractive index, that one can check against the observations.

"Pseudo" phase functions at scattering angles of 60°, 90°, and 120° are plotted versus the Ångström coefficient in Figs. 7a-c for the S&F models and the observations. The values for the models are taken from Table 1. The relationship between Ångström coefficient and "pseudo" phase functions is analyzed by linear regression. The correlation coefficient for the models, R^2, varies from 0.74 at 60° to 0.79 at 120°, and the corresponding "pseudo" phase functions of the selected models can be retrieved from the Ångström coefficient with an accuracy of 0.081, 0.030, and 0.016, at 60°, 90°, and 120°, respectively. Thus, the model "pseudo" phase functions, which influence directly the sky radiance, can be predicted rather accurately by the Ångström coefficient.

This is confirmed by the observations also given in Figs. 7a-c for the same angles as the models. The linear regressions performed on the data show very similar intercepts and slopes at 90° and 120 °, and coefficients smaller by 20% at 60° when compared to the models. The data may be classified in 3 groups, see Table 5: a large group of 45 measurements around α = 1.3, a smaller group of 14 measurements around α = 0.5, and 3 measurements only around α = 0. The first group fits the S&F T90 model; the second typifies the S&F Coastal model. It is not clear whether the 3 measurements in the last group correspond to very maritime conditions or to undetected thin clouds. Table 5 gives the mean and standard values of the observed phase functions for each data set. The standard deviation of the "pseudo" phase functions is about 0.02 at 90° and 120 ° for the two main significant data sets. This value of 0.02 can be retained as indicative of the accuracy of the phase function retrieval from the Ångström coefficient.

Previous investigators (Kaufman, 1993; Kaufman et al., 1994) have also attempted to retrieve the phase function at the scattering angle of 120 ° from sky radiance measurements. Table 1 of Kaufman (1993) gives the measurements of aerosol optical thickness, Ångström coefficient, and sky radiance at 613 nm, for several continental locations. The optical thickness range is 0.03 - 1.53, and the Ångström coefficient varies between 0.09 to 1.94. After correcting the data for molecular scattering, we have not been able to establish a relationship between α

and $\varpi_{0a}\, p_a(120°)$ at 613 nm, and we have only been able to retrieve a mean value of 0.2 for $\varpi_{0a}\, p_a(120°)$ at 613 nm. This value is slightly larger than that predicted by most models, see Table 1. Kaufman et al. (1994) in their Table 1 provide other results of a more thorough investigation at 5 locations. They also give values of the phase function at 870 nm for a scattering angle of 120°. Their derived phase functions are higher than those of most models, but some relationship with the Ångström coefficient appears to exist, except for one of the sites, located in Brazil. Our study gives results at several scattering angles, which better agree with models than previously reported elsewhere.

In summary, two main points emerge from the analysis: (1) within the accuracy of the measurements, the S&F models do allow one to describe the observed Ångström exponents and phase functions; and (2) the phase function can be predicted from the Ångström coefficient with a typical accuracy of 0.02 at scattering angles in the range 90° - 120 °.

b) Wavelength dependence of the aerosol radiance

Computed values for the S&F models show a relationship between the spectral dependence of the aerosol sky radiances, $\varepsilon_a(870, 1020)$, and the Ångström coefficient, α (Figs. 8a-c). The analysis of the actual measurements, however, has been rather disappointing on that point. The data set was carefully restricted to aerosol optical thicknesses around 0.1 (from 0.08 to 0.12) in order to avoid an effect of the optical thickness. Aerosol radiances were derived at 670, 870, and 1020 nm, after subtracting the computed molecular radiances, for scattering angles θ = 60°, 90°, and 120°. Then, the ratio of two aerosol radiances at two wavelengths, $\varepsilon_a(670, 870, \theta)$ or $\varepsilon_a(870, 1020, \theta)$, was calculated.

The only significant correlation between α and ε_a is obtained with $\varepsilon_a(870, 1020, \theta)$ for the scattering angle of 60° (R^2 = 0.40), and to a lesser degree of 120° (R^2 = 0.14), as shown in Figs. 8a-c. The agreement between measurements and models is rather good again for the scattering angle of 60°. In all other cases, the inaccuracy of the derived coefficients limits the interpretation and does not allow one to conclude

definitely about the representation of the models. Kaufman (1993) and Kaufman et al. (1994) also report data on the spectral dependence, between 613 or 620, and 870 nm, of the aerosol radiance for the scattering angle of 120°, but they hardly show any correlation with α. Despite the limitation due to inaccuracy of the measurements, our data set is the first one to show that the spectral dependencies of the aerosol optical thickness and radiance are related according to the models.

It is important to note that, even though the S&F models appear to represent the observations adequately, a major problem for atmospheric correction of satellite ocean color imagery is extrapolation to the visible of the aerosol information obtained using spectral bands in the near-infrared. The aerosol signal in the near-infrared is mainly affected by the coarse particle mode of aerosols; it contains little information about the accumulation mode. Yet the accumulation mode has strong scattering effects in the visible. Evaluating the accuracy of the extrapolation to the visible, however, is beyond the scope of the present study.

5. Accuracy of the Measurements

Accuracy of the derived parameters, i. e. aerosol optical thickness, Ångström coefficient, phase function, and spectral dependency of the aerosol reflectance has been estimated. The various types of error have been regrouped into two major categories: (1) errors due to instrumentation and methods such as calibration, stability of the detectors, accuracy of the formulas and of the exogen parameters used in the computations and (2) errors due two geophysical conditions such as the presence of clouds, stratospheric aerosols, or interaction between ground and atmosphere.

In the following, errors in the computation of solar zenith angle, airmass, and Sun-Earth distance factor have been neglected. When no sign precedes the error, the error can be positive or negative.

5.1. Errors due to instrumentation and methods

a) Aerosol optical thickness

The accuracy on the calibration coefficient $\Delta(\ln I_0)$ m has been estimated using the 5 most regular Langley plots of all the 1994 campaign obtained with the automatic CIMEL instrument . The accuracy on the Rayleigh optical thickness, $\Delta\tau_r$, has been computed assuming a one percent relative error on the computation of Rayleigh optical thickness at standard pressure and a ±10 hPa error on pressure. Error on the gaseous transmission $\Delta(t_g)/t_g$ has been neglected, except at 670 nm where it has been computed as the result of a 1 nm error on wavelength and of a 20 % relative error on ozone content. Finally, a 5 °C error on the temperature of the detector has been assumed, resulting in a relative error of $\Delta S/S = 0.01$ on the sensitivity of the detector at 1020 nm.

The total error is the quadratic sum of the above parameters. The final results are displayed in Table 6a. The retrieval of the Ångström coefficient is affected by the errors on the optical thicknesses, increasingly when the aerosol optical thickness decreases. The absolute error on τ_a does not depend on the actual value of τ_a. Thus the relative error on τ_a varies like $1/\tau_a$ and becomes very large for low values of the optical thickness (e. g., 60% at 440 nm when $\tau_a = 0.05$).

b) Aerosol reflectance

The study has been performed at 870 and 1020 nm only. The error $\Delta\rho_a$ on the aerosol reflectance is the sum of the error $\Delta\rho$ on the measured reflectance, $\Delta\rho = \rho \Delta K/K$ where K is the calibration coefficient, all other error sources being negligible, and the error $\Delta\rho_r$ on the molecular reflectance. The relative error on the calibration coefficient is about 2%. The relative error $\Delta\rho_r/\rho_r$ has been simulated for a scattering angle of 90° and shows weak variations with solar zenith angle for solar zenith angles smaller than 80°. At 870 nm, as well as 1020 nm, the inaccuracy on ρ_r is less than 2%. The relative error $\Delta\rho_a/\rho_a$ has been simulated using the S&F model C70 for an aerosol optical thickness of 0.03, 0.05, 0.1, and 0.2. The results are displayed in Table 6b. The inaccuracy decreases with increasing aerosol optical thickness, from 9 to 3% at 870 nm and 6 to 3 % at 1020 nm.

c) Spectral dependency

The relative error on the spectral dependency ε of the aerosol reflectance is the sum of the relative error on the aerosol reflectance at the two wavelengths used to compute ε, i. e. 870 and 1020 nm in our case:

$$\Delta\varepsilon_a(870,1020) / \varepsilon_a(870,1020) = \Delta\rho_a(870)/\rho_a(870) + \Delta\rho_a(1020)/\rho_a(1020) \qquad (18)$$

The results are dependent upon aerosol optical thickness, indeed (see Table 6b). As for the aerosol reflectance, the error on ε_a decreases with increasing optical thickness, from 16% at $\tau_a = 0.03$ to 6% at $\tau_a = 0.2$.

d) Aerosol "pseudo" phase function

The relative error on the retrieved aerosol "pseudo" phase function is the sum of the relative error on the aerosol optical thickness and on the aerosol reflectance. An additional error results from the approximation of the aerosol reflectance (e. g. single scattering approximation) and has been simulated for the model C70 and a scattering angle of 90°. Both errors are represented in Table 6c. Inaccuracy is large for small aerosol amount (up to 50% for $\tau_a = 0.03$) and decreases with increasing aerosol optical thickness.

5.2. Errors due to geophysical conditions

Errors due to geophysical conditions are more difficult to estimate. The presence of stratospheric aerosols perturbs the retrieval of tropospheric aerosol parameters. We have seen (section 4.1) that a significant relative amount of stratospheric aerosol exists. Another perturbation may be the presence of clouds, either contaminating sun measurements, sky measurements, or both. We concentrated our measurements during clear days but the presence of invisible thin cirrus is always possible. A third type of error, which can occur during retrieval of phase function from ground-based measurements, is due to interaction between

ground and atmosphere (Yang et al.; 1994). This interaction does not exist or is negligible for observations from a boat or a small island, but are crucial for ground-based measurements performed in coastal (or continental) regions.

Since the coastline is approximately in the north-south direction at the SIO Pier, the sun is above the land surface in the morning and the sky radiance measurements of $\rho(60°)$ to $\rho(120°)$ are made with the instrument viewing above the ocean surface. In this configuration, the ground effect is negligible. In the afternoon, $\rho(60°)$ to $\rho(120°)$ are measured over the land surface, and interaction between surface reflection and atmospheric scattering may not be negligible any more.

Simulations were performed in order to study the land surface effect. Sky radiances, as seen from the ground, were simulated at 870 nm for the models T70 and M98 with two aerosol amounts ($\tau_a = 0.1$ and $\tau_a = 0.2$ at 870 nm) for a solar zenith angle of 39.9°, 62.1°, and 80.7°. Several values of the ground reflectance were used, namely 0, 0.2, 0.5, and 1 (academic case). Table 6d summarizes the results and gives the normalized radiance of the sky, R_n, and the relative error, [deduced - exact] / exact, due to neglecting the coupling term. Neglecting the interaction between land surface reflection and atmospheric scattering overestimates the derived aerosol phase function. We can also notice that in Table 6d the coupling between ground and atmosphere is more important for a small solar zenith angle.

Interaction between glitter and atmosphere was also studied. At our coastal site, where land is to the east, during the morning the glitter can only influence the directions at a lower elevation from the direction of specular reflection, but these directions are not used for sky radiance measurement. During the afternoon, however, the glitter influence is effective. The normalized radiance of the sky for models T70 and M98 has been computed, for a scattering angle of 90°, a black surface and no glitter (a flat water surface), and a water surface agitated by a wind speed of 10 ms^{-1}. For the relation between wind speed and wave slope we used the theory developed by Cox and Munk (1955). We found (see Table 6e) that the effect of interaction between glitter and atmosphere is small compared to that of interaction between ground and atmosphere, except at large sun zenith angles.

6. Discussion

6.1. Aerosol loading

Measurements at SIO Pier during the 1993 and 1994 Winters indicate a high frequency of aerosol optical thicknesses below 0.1 with values often around 0.05 at 870 nm. This is well below what is considered as a tropospheric background in most of the comprehensive models (Handbook of Geophysics and the Space Environment, 1985; WMO, 1986).

Such low values have been reported in the literature for ground-based measurements in the Antarctic (Obleitner, 1992, Herber et al., 1993), or satellite surveys using NOAA AVHRR over the Pacific (Stowe, 1991). Some ground-based measurements, however, did not reveal low tropospheric backgrounds. In Kaufman (1993), only 25 % of the measured aerosol optical thicknesses are below 0.12 at 613 nm (0.1 at 870 nm) with a large contribution of Australian sites, while the other sites are mainly European. The SIO Pier site is under the influence of an eastward airflow, and far from any main terrestrial source (Asia). Natural deposition and scavenging by rainfall occurs during the long westerly journey, and these Asian aerosols do not reach the west coast of the United States. The only aerosol sources are local, maritime when there is a strong west wind regime, and urban when the breeze regime brings offshore the local production of San Diego and Los Angeles agglomerations.

Over the ocean, Hopel et al. (1990) show some values of β, the aerosol optical thickness at 1 μm, which are lower than 0.08 in the western section of their cruise across the North Atlantic Tropical Ocean, i. e. the Sargasso Sea. These results were confirmed by Korotaev et al. (1993) over the North Atlantic. In the North Atlantic, Saharan dust outbreaks affect large zones offshore Morocco, Mauritania and Senegal, increasing the aerosol loading. The earliest report on low aerosol optical thickness at sea is found in the Indian Ocean by Tomasi and Prodi (1982), where they only found occasional value of β below 0.1. In the Pacific Ocean, Villevalde et al. (1994) report some measured optical thicknesses at 551 nm which are predominantly

below 0.2, and 50 % of them below 0.13 at 551 nm, with the lowest optical thickness observed for a low wind speed.

It should be noted that our measurements were made during the winter season, only. One expects similar results for the other seasons, however, because the region does not experience drastic weather changes during the year. In Summer, sea breezes are well developed, and they produce thick coastal fog that can extend inland. Subsidence generates strong temperature inversions, with pollutants and moisture concentrated under the base of the inversion, resulting in stratocumulus clouds. These pollution conditions, however, can hardly be sampled using sun photometry, because of the cloud cover. In Winter, the subsidence and temperature inversions are weaker, and they may be destroyed by the passage of cyclones, facilitating the dispersion of pollutants. In the Fall and early Winter, the Pacific High occasionally extends eastward, producing a southwestward flow across California. In the Los Angeles basin, the resulting wind is calm and the effect is more high temperatures and low relative humidities (Santa Ana conditions). We may not have sampled Santa Ana conditions, but many of our measurements were made in the presence of easterly winds.

The level of aerosol loading, via the aerosol optical thickness, does affect directly the accuracy of the retrieval of ocean (color) reflectances from space. The (normalized) radiance scattered by the aerosol, ρ_a, varies linearly like τ_a:

$$\rho_a \sim \tau_a \, p_a(\theta) \, / \, 4 \, \mu_v \qquad (19)$$

where p_a is the other aerosol optical parameter of interest. From our results, we would take mean values of $\tau_a \sim 0.05$ and of $p_a \sim 0.1$ at a scattering angle of 120°, so that $\rho_a \sim 0.002$, which is far less than currently admitted. At this level of ρ_a, the atmospheric correction for aerosol scattering is no more a challenge. Usually, the spectral behavior of R_a is determined in the near infrared and extrapolated at visible wavelengths (Gordon and Wang, 1994). A relative 10 % inaccuracy on this extrapolation would give an error of 0.0002 on ρ_a that meets the requirement for an ocean color mission. Simulations of the atmospheric correction scheme have been

done by Gordon and Wang (1994) for a typical aerosol optical thickness of 0.2 at 870 nm. This value appears to be several times higher than standard conditions at sea, thus the errors on the marine reflectance retrievals which are assessed in the same study are also overestimated by the same factor. Results given by Gordon and Wang (1994) are more typical of marginal conditions when the background aerosol is increased by a strong local source, likely terrestrial.

6.2 Aerosol models for atmospheric correction of ocean color

For atmospheric correction of satellite ocean color radiances, Gordon and Wang (1994) propose to use models derived from Shettle and Fenn (1979), namely two basic components, Maritime and Terrestrial models, and a mixture of these two components, a Coastal model. In each of these models, physical and optical properties are parameterized as a function of humidity. We have examined whether the selected models are representative of realistic conditions and whether they should be complemented by other models, such as WMO or any other models.

Some of our findings are illustrated in Fig. 7, which gives the "pseudo" phase function versus the Ångström coefficient as obtained from models and derived from measurements. These two parameters are key atmospheric correction parameters: the product of the "pseudo" phase function and aerosol optical thickness gives the amplitude of the perturbation, and the Ångström coefficient determines roughly the spectral variation of the perturbation. Thus Fig. 7, which shows "pseudo" phase function as a function of Ångström coefficient, does allow one to visualize the main parameters of the atmospheric correction at a specific scattering angle.

Based on our analysis of data and models, we can also make the following remarks:

(1) additional WMO models bring very little variability to the S&F models,

(2) measurements and S&F model results do agree significantly within the accuracy of the retrieved parameters,

(3) different aerosol models can only be identified from the measurements under marginal conditions, i. e. when the aerosol optical thickness is large,

(4) under normal conditions, the aerosol optical thickness is low and the measurements suggest a single background aerosol model, and
(5) the background model is strongly influenced by the stratospheric component, which in 1994 was different from that in 1993.

These findings and remarks might help design the atmospheric correction scheme. At low optical thickness, under stable stratospheric conditions, it would be appropriate to specify the background model regionally. At larger optical thickness, more variability in the models would be useful to account for the different local sources of aerosols, and thus of perturbations.

6.3. Recommendations for in-situ ship borne measurements.

Accurate measurements of aerosol optical thickness and Ångström coefficient can be made at sea using hand-held sun photometers, as indicated by the results obtained during the CALCOFI 1994 winter cruise. Are these measurements sufficient or not to verify the atmospheric correction and, if not, what other measurements are necessary?

Using sky radiances measured from a terrestrial station, thus in much more stable conditions than at sea, we have not been able to improve the determination of the aerosol type better than by only using the Ångström coefficient. In most cases, at low aerosol optical thicknesses, the sky radiance measurements are simply not accurate enough to provide useful information. More effort is needed to improve the accuracy of ground-based sky radiance measurements before making those measurements at sea. Our results suggest that Ångström coefficient measurements are sufficient to verify the determination of the aerosol models by the algorithm proposed by Gordon and Wang (1994) and, hence, the amplitude of the atmospheric perturbation on satellite ocean color radiances.

7. Summary and Conclusions

Direct atmospheric transmittance and sky radiance were measured at 440, 670, 870 and 1020 nm on the Scripps Institution of Oceanography Pier during the

Winters of 1993 and 1994. Additional measurements of direct solar transmittance have been made in 1994 on Catalina Island (about 40 km offshore) and during the CALCOFI 1994 Winter cruise. The total and aerosol optical thicknesses, and the spectral dependency of the aerosol optical thickness (Ångström coefficient), were derived from the measurements of the direct atmospheric transmittance. The aerosol scattering "pseudo" phase functions, and their spectral dependency between 870 and 1020 nm, were derived from the measurements of the sky radiances at the scattering angles of 60°, 90°, and 120 °. The optical measurements were performed under varied atmospheric conditions and, therefore, in the presence of diversified aerosol types, including maritime, terrestrial, and urban.

This comprehensive data set on aerosol scattering properties was gathered with respect to two specific objectives. The first objective was to validate the selection of aerosol models used in the algorithms for the atmospheric correction of space-based ocean color observations, such as those of the SeaWiFS mission (Gordon and Wang, 1994). The second objective was to identify what type of atmospheric optics measurements should be performed to verify atmospheric correction algorithms.

The analysis of data and aerosol models has provided the following main findings and conclusions:

(1) Low aerosol optical thicknesses have been observed in the study area, consistent with previous measurements over the oceans. The τ_a values are influenced by the stratospheric aerosol content, higher in 1993 than in 1994. After correction of the stratospheric content, most of the τ_a values, i. e. $\tau_{a,tropo}(870)$, are below 0.1. In such conditions, it is impossible to identify the variability in the aerosol scattering properties, and one has to rely on a mean background model including the stratospheric component in the atmospheric correction algorithms.

(2) Some variability of the aerosol scattering properties has been identified for high optical thickness, i. e. above 0.1 at 870 nm. Two modes can be clearly identified. The first mode has an Ångström coefficient, α, around 1.2, corresponding to a Tropospheric model. The second mode has α below 0.5 and tending to 0.2, corresponding to a Maritime model.

(3) Measurements confirm the relationship between $\varpi_a p_a$ and α predicted by the models. The dispersion, however, is larger in the measurements than in the model results. The agreement is not good for the relationship between ε and α, partly because of the uncertainties in the derived ε values. These findings indicate that, within the accuracy of the measurements, the S&F model allow one to describe the observations of Ångström coefficient and phase function. Additional models bring little more. Furthermore, and importantly from a practical point of view, the phase function can be predicted from measurements of α. Therefore, shipborne measurements of α appear sufficient to validate the aerosol model used in the algorithms. Such measurements were performed during the CALCOFI cruise and they proved reliable.

(4) There is no definite relationship between aerosol characteristics and meteorological conditions, but in some instances, small α values are associated with onshore airflow from the ocean and high α values with offshore flow from the land. Spatial variations of τ_a and α have been observed. In general, τ_a and α are lower offshore than along the coast, suggesting that the atmospheric correction offshore is much simplified.

Acknowledgments

This work has been supported by the Centre National d'Etudes Spatiales, the Centre National de la Recherche Scientifique, and the Région Nord/Pas de Calais in France, and by the National Aeronautics and Space Administration under grants NAGW-2666 and -3498 (to R. Frouin) and the California Space Institute. The authors wish to thank Dr. Eric Pouliquen and Ms. Stéphanie Schaeffer, who collected sun photometer aboard R/V Wecoma and in Catalina Island, respectively, Mr. J.-Y. Balois, who helped calibrate and maintain the instrumentation, and Mr. Rony Hermanto and Mr. John McPherson, who helped to process the sky radiance datasets.

References

Abbott, M. R., O. B. Brown, R. H. Evans, H. R. Gordon, K. L. Carder, F. E. Müller-Karger, and W. E. Esaias, Ocean color in the 21st Century: A strategy for a 20-year time series, *NASA Technical memorandum 104566, Vol. 17, June 1994*, 20 pp., available from the NASA Center for Aerospace Information, 800 Elkridge Road, Linthicum Heights, M 21090-2934, 1994.

André, J. M., and A. Morel, Simulated effects of barometric pressure and ozone content upon the estimate of marine phytoplankton from space, *J. Geophys. Res.*, 94, 1029-1037, 1989.

Ångström, A., Techniques of determining the turbidity of the atmosphere, *Tellus, 13*, 214-223, 1961.

Ångström, A., The parameters of atmospheric turbidity, *Tellus, 16*, 64-75, 1964.

Ardanuy, P. E., D. Han, and V. V. Salomonson, The Moderate Resolution Imaging Spectrometer (MODIS) science and data system requirements, *IEEE Trans. Geosci. Remote Sensing*, 29, 75-88, 1991.

Bruegge, C. J., R. N., B. Markham, M. Spanner, and R. Wrigley, Aerosol optical depth retrievals over the Konza Prairie, *J. Geophys. Res.*, 97, 18743-18758, 1992.

D'Almeida, Koepke, and Shettle, Atmospheric aerosols. *Global climatology and radiative characteristics*, A Deepak Pub., Hampton, Virginia, 561 pp., 1991.

Diermeidjan, D., *Electromagnetic scattering on spherical dispersions*, Elsevier, New-York, 290 pp., 1969.

Deschamps, M. Herman, and D. Tanré, Modeling of the atmospheric effects and its application to the remote sensing of ocean color, *Appl. Opt.*, 23, 3751-3758, 1983.

Deschamps, P. Y., F. M. Bréon, M. Leroy, A. Podaire, A. Bricaud, J. C. Buriez, and G. Sèze, The POLDER Mission: Instrument characteristics and scientific objectives, *IEEE Trans. Geosci. Remote Sensing*, 32, 598-615, 1994.

Deuzé, J. L., M. Herman, and R. Santer, Fourier series expansion of the transfer equation in the atmosphere ocean system, *J. Quant. Spectr. Rad. Transfer*, 41, 483-494, 1989.

Dutton, E. G., P. Reddy, S. Ryan, and J. DeLuisi, Features and effects of aerosol optical depth observed at Mauna Loa, Hawaii: 1982-1992, *J. Geophys. Res., 99*, 8295-8306, 1994.

Estep, L., and R. Arnone, Effect of whitecaps on determination of Chlorophyll concentration from satellite data, *Rem. Sens. Environ., 50*, 328-334, 1994.

Frouin, R., P.-Y. Deschamps, and M. Schwindling, Spectral reflectance of sea foam in the visible and near-infrared: in-situ measurements and remote sensing implications. *J. Geophys. Res., 101*, 14361-14371, 1996.

Gordon, H. R., Atmospheric correction of ocean color imagery in the Earth Observing System era. *J. Geophys. Res., 102*, 17081-17106, 1997.

Gordon, H. R., and D. K. Clark, Atmospheric effects in the remote sensing of phytoplankton pigments, *Boundary-Layer Meteorol., 18*, 299-313, 1980.

Gordon H. R., and D. K. Clark, Clear water radiances for atmospheric correction of Coastal Zone Color Scanner, *Appl. Opt., 20*, 4175-4180.

Gordon, H. R., and M. Wang, Retrieval of water-leaving radiance and aerosol optical thickness over the oceans with SeaWiFS: A preliminary algorithm, *Appl. Opt., 33*, 442-453, 1994.

Gordon, H. R., D. K. Clark, J. L. Mueller, and W. A. Hovis, Phytoplankton pigments derived from the Nimbus-7 CZCS: initial comparisons with surface measurements, *Science, 210*, 63-66, 1980.

Gordon, H. R., D. K. Clark, J. W. Brown, O. B. Brown, R. H. Evans, and W. W. Broenkow, Phytoplankton pigment concentration in the middle Atlantic Bight: comparison between ship and Coastal Zone Color Scanner estimates, *Appl. Opt., 22*, 20-36, 1983.

Gordon, H. R., J. W. Brown, and R. H. Evans, Exact Rayleigh scattering calculations for use with the Nimbus 7 Coastal Zone Color Scanner, *Appl. Opt., 27*, 862-871, 1988.

Handbook of Geophysics and the Space Environment, A. S. Jursa, Ed., Air Force Geophysics Laboratory, Air Force Systems Command, Available from National Technical Information Service, VA, 1985.

Hänel, G., The real part of the mean complex refractive index and the mean density of samples of atmospheric aerosol particles, *Tellus, 20*, 371-379, 1968?? 1972

Hänel, G., The properties of atmospheric aerosol particles as functions of the relative humidity at thermodynamic equilibrium with the surrounding moist air, *Adv. Geophys., 19,* 77-188, 1976.

Herber, A., L. W. Thomason, V. F. Radionov, and U. Leiterer, Comparison of trends in the tropospheric and stratospheric aerosol optical depths in the Antarctic, *J. Geophys. Res., 98,* 18441-18447, 1993.

Holben, B. N., T. F. Eck, I. Slutsker, D. Tanré, J. P. Buis, A. K. Setzer, E. Vermote, J. A. Reagan, Y. A. Kaufman, Multi-band automatic sun and sky scanning radiometer system for measurement of aerosols, *in Coll. Signatures Spectrales, Val d'Isère, Janvier 1994, ESA,* 75-83, 1994.

Hooker, S. B., and W. Esaias, An overview of the SeaWiFS project, *EOS Trans. AGU, 74,* 241 and 245-246, 1993.

Hooker, S. B., C. R. McClain, and A. Holmes, Ocean Color Imaging: CZCS to SeaWiFS, *Mar. Technol. Soc. J., 27,* 3-15, 1993.

Hoppel, W. A., J. W. Fitzgerald, G. M. Frick, and R. E. Larson, Aerosol size distributions and optical properties found in the marine boundary layer over the Atlantic Ocean, *J. Geophys. Res., 95,* 3659-3686, 1990.

Hovis, W. A., D. K. Clark, E. Anderson, R. W. Austin, W. H. Wilson, E. T. Baker, D. Ball, H. R. Gordon, J. L. Mueller, S. Z. El-Sayed, B. Sturm, R. C. Wrigley, and C. S. Yentsch, Nimbus-7 Coastal Zone Color Scanner: System description and initial imagery, *Science, 210,* 60-63, 1980.

Joint Global Ocean Flux Study (JGOFS), The Joint Global Ocean Flux Study: Background, Goals, Organization and Next Steps, *Scientific Committee on Oceanic Research, International Council of Scientific Unions,* Paris, 1987.

Kasten F., and A. T. Young, Revised optical air mass tables and approximation formula, *Applied Optics, 28,* 1989.

Kaufman, Y. J., A. Gitelson, A. Karnieli, E. Ganor, R. S. Fraser, T. Nakajima, S. Mattoo, and B. N. Holben, Size distribution and scattering phase function of aerosol particles retrieved from sky brightness measurements, *J. Geophys. Res., 99,* 10341-10356, 1994.

Kaufman, Y. J., Aerosol optical thickness and atmospheric path radiance, *J. Geophys. Res., 98,* 2677-2692, 1993.

Kent, G. S., M. P. McCormick, and P.-H. Wang, Validation of Stratospheric Aerosol and Gas Experiments I and II satellite aerosol optical depth measurements using surface radiometer data, *J. Geophys. Res., 99*, 10333-10339, 1994.

Korotaev, G. K., S. M. Sakerin, A. M. Ignatov, L. L. Stowe, and E. P. McClain, Sun-photometer observations of the aerosol optical thickness over the North Atlantic from a Soviet Research Vessel for validation of satellite measurements, *J. Atmos. Ocean. Technol., 10*, 725-735, 1993.

Nakajima, T., M. Takamura, M. Yamano, M. Shiobara, T. Yamanuchi, R. Goto, and K. Murai, Consistency of aerosol size distribution inferred from measurements of solar radiation and aureole, *J. Meteorol. Soc. Jap., 64*, 765-776, 1986.

Nakajima, T., M. Tanaka, and T. Tamaguchi, Retrieval of the optical properties of aerosols from aureole and extinction data. *Appl. Opt., 22*, 2951-2959, 1983.

Nilsson, Meteorological influence on aerosol extinction in the 0.2-40 μm wavelength range, *Appl. Opt., 18*, 3457, 1979.

O'Neill, N. T., A. Royer, P. Coté, and L. J. B. McArthur, Relations between optically derived aerosol parameters, humidity, and air-quality parameters in an urban atmosphere, *J. Appl. Meteorol., 32*, 1484-1498, 1993.

Obleitner, F., Atmospheric turbidity at the Antarctic Coastal Station Georg-von-Neumayer (70°S, 8°W, 40 m MSL), *J. Appl. Meteorol., 31*, 1202-1209, 1992.

Paltridge G. W., and Platt C. M. R., Radiative Processes in Meteorology and Climatology, *Development in Atmospheric Science, Elsevier Scientific Pub. Co. New-York, NY 10017*, 1977.

Rast, M. and J.-L. Bézy, The ESA medium resolution imaging spectrometer (MERIS): requirements to its mission and performance of its system. In RSS95, *Remote Sensing in Action*, Proc. 21st Annual Con. Remote Sensing Soc., 11-14 September 1995, University of Southampton, P. J. Curran and Y. C. Robertson, Eds., 125-132, 1995.

Shettle and Fenn, E. P., and R. W. Fenn, Models of the atmospheric aerosols and their optical properties, *in Optical propagation in the atmosphere*, AGARD-CP-183, 1976.

Shettle E. P., and R. W. Fenn, Models for the aerosols of the lower atmosphere and the effect of humidity variations on their optical properties, *AFGL-Rep. TR-79-0214*, Air Force Geophys. Lab., Bedford, Mass., 1979.

Smirnov, A., A. Royer, N. T. O'Neill, and A. Tarussov, A study of the link between synoptic air mass and atmospheric optical parameters, *J. Geophys. Res., 99*, 20967-20982, 1994.

Stowe, L. L., Cloud and aerosol products at NOAA/NESTS, *Global and Planetary Change, 4*, 25-32, 1991.

Tanré D., C. Deroo, P. Duhaut, M. Herman, J.-J. Morcrette, J. Perbos, P.-Y. Deschamps, 1990. Description of a computer code to simulate the signal in the solar spectrum: the 5S code. *Int. J. Remote Sensing, 11*, 659-668.

Tanré, D., C. Devaux, M. Herman, R. Santer, and J. Y. Gac, Radiative properties of desert aerosols by optical ground-based measurements at solar wavelengths, *J. Geophys. Res., 93*, 14,223-12,231, 1988.

Tanré, D., M. Herman, P.-Y. Deschamps, and A. De Leffe, Atmospheric modeling for space measurements of ground reflectances, including bi-directional properties, *Appl. Opt., 18*, 3587-3594, 1979.

Tomasi, C., and F. Prodi, Measurements of atmospheric turbidity and vertical mass loading of particulate matter in marine environments, *J. Geophys. Res., 87*, 1279-1286, 1982.

Toon, O. B., and J. B. Pollack, A global average model of atmospheric aerosols for radiative transfer calculations, *J. Appl. Meteorol., 15*, 225-246, 1976.

Travis, L. D., and J. E. Hansen, 1974, Light scattering in planetary atmospheres, *Space Sci. Rev.*, 16, 527-..., 1974.

Villevalde, V. Yu., A. V. Smirnov, N. T. O'Neill, S. P. Smyshlyaev, and V. V. Yakovlev, Measurement of aerosol optical depth in the Pacific Ocean and the North Atlantic, *J. Geophys. Res., 99*, 20883-20988, 1994.

Viollier, M., D. Tanré, and P. Y. Deschamps, An algorithm for remote sensing of water color from space, *Boundary-Layer Meteorol., 18*, 247-267, 1980.

WMO, A preliminary cloudless standard atmosphere for radiation computation, *WCP-112 and WMO/TD No. 24*, March 1986, 53 pp., 1986.

Yang H., H. R. Gordon, and T. Zhang, 1994. Island perturbation to the sky radiance over the ocean - simulations. *Applied Optics, 34*, 8354-8362, 1995.

Young, A. T., On the Rayleigh-scattering optical depth of the atmosphere, *J. Appl. Meteorol., 20*, 328-330, 1981.

model	Ångström coefficient	$p_a(60°)$ at 870 nm	$p_a(90°)$ at 870 nm	$p_a(120°)$ at 870 nm	ϖ_{0a}
T70	1.46	0.991	0.328	0.197	0.935
T90	1.35	0.811	0.239	0.141	0.970
T98	1.22	0.718	0.201	0.118	0.984
C70	0.63	0.676	0.208	0.125	0.977
C90	0.40	0.505	0.134	0.091	0.992
C98	0.27	0.438	0.105	0.077	0.996
M70	0.40	0.611	0.184	0.111	0.986
M90	0.21	0.458	0.118	0.084	0.995
M98	0.12	0.405	0.093	0.072	0.998
WMO Mar.	0.22	0.527	0.150	0.096	0.986
WMO Cont.	1.18	0.906	0.310	0.191	0.842
WMO Urb.	1.32	0.979	0.356	0.234	0.591

Table 1: Optical properties of the aerosol models of Shettle and Fenn (1979) and WMO (1986).

channel nm	gain	K plaque Jan. 16, 94 Stev. Pk.	K plaque Jan. 29, 94 SIO Pier	K sphere July 93	K sphere April 94	Error max.	Plaque/ sphere
1020	S	$8.45\ 10^{-5}$	$8.36\ 10^{-5}$	$9.02\ 10^{-5}$	$9.02\ 10^{-5}$	0.08	0.07
	A		$8.57\ 10^{-4}$	$8.96\ 10^{-4}$	$9.37\ 10^{-4}$	0.10	0.10
870	S	$7.82\ 10^{-5}$	$7.73\ 10^{-5}$	$8.23\ 10^{-5}$	$8.11\ 10^{-5}$	0.07	0.04
	A		$8.82\ 10^{-4}$	$9.15\ 10^{-4}$	$9.42\ 10^{-4}$	0.07	0.07
670	S	$8.20\ 10^{-5}$	$8.35\ 10^{-5}$	$9.14\ 10^{-5}$	$8.67\ 10^{-5}$	0.12	0.06
	A		$1.05\ 10^{-3}$	$1.13\ 10^{-3}$	$1.10\ 10^{-3}$	0.08	0.05
440	S	$6.18\ 10^{-5}$	$6.24\ 10^{-5}$	$6.63\ 10^{-5}$	$6.25\ 10^{-5}$	0.08	0.02
	A		$6.69\ 10^{-4}$	$6.68\ 10^{-4}$	$6.61\ 10^{-4}$	-0.02	-0.02

Table 2: Calibration coefficient, K (in W/m2/sr/nm/numerical count), of the automatic CIMEL instrument. The two last columns give the maximum relative error, (Kmax - Kmin)/Kmin, and the relative error between the plaque field calibration on January 16, 1994 and the sphere laboratory calibration on April 1994.

τ_a	θ_s (°)	Aerosol model	Actual	Retr'ved (Eq. 14)	Rel. Err. (Eq. 14)	Retr'ved (Eq. 17)	Rel. Err. (Eq. 17)
0.1	39.9	T70	0.928	0.903	-0.03	1.004	0.09
		M98	0.404	0.402	-0.01	0.448	0.11
	62.17	T70	0.928	0.889	-0.05	0.982	0.06
		M98	0.404	0.402	-0.01	0.444	0.10
	80.72	T70	0.928	0.738	-0.21	0.822	-0.12
		M98	0.404	0.363	-0.11	0.404	0
0.2	39.9	T70	0.928	0.879	-0.06	1.088	0.18
		M98	0.404	0.402	-0.01	0.497	0.24
	62.17	T70	0.928	0.850	0.09	1.039	0.12
		M98	0.404	0.400	-0.01	0.488	0.21
	80.72	T70	0.928	0.617	-0.34	0.765	-0.18
		M98	0.404	0.336	-0.17	0.416	0.03

Table 3 a: Comparison between the actual and retrieved (by approximate Eqs. 14 and 17) values of the "pseudo" phase function $\varpi_a\, p_a(60°)$ at 870 nm, for aerosol models T70 and M98 and for a scattering angle of 60°.

τ_a	θ_s (°)	Aerosol model	Actual	Retr'ved by Eq. 14	Rel. Err. by Eq. 14	Retr'ved by Eq. 17	Rel. Err. by Eq. 17
0.1	39.9	T70	0.941	0.920	-0.03	0.997	0.06
		M98	0.404	0.403	-0.01	0.447	0.11
	62.17	T70	0.941	0.911	-0.04	0.982	0.05
		M98	0.404	0.403	-0.01	0.445	0.11
	80.72	T70	0.941	0.799	-0.16	0.866	-0.08
		M98	0.404	0.372	-0.08	0.414	0.03
0.2	39.9	T70	0.941	0.901	-0.05	1.058	0.13
		M98	0.404	0.403	-0.01	0.497	0.24
	62.17	T70	0.941	0.880	-0.07	1.023	0.09
		M98	0.404	0.402	-0.01	0.490	0.22
	80.72	T70	0.941	0.693	-0.27	0.815	-0.14
		M98	0.404	0.346	-0.15	0.427	0.06

Table 3 b: Same as Table 3 a, but at 1020 nm.

	Nb. of SAGE Obs.	Observed $\tau_{a,strato}(\lambda)$ at 1 μm	Observed $\tau_{a,strato}(\lambda)$ at 525 nm	Derived $\tau_{a,strato}(\lambda)$ at 870 nm	Derived α_{strato}
1993: z > 13.5 km	8	0.0432 ± 0.0056	0.0472 ± 0.0064	.0442	0.136
1994: z > 9.5 km	7	0.0178 ± 0.0045	0.0275 ± 0.0072	0.0199	0.675
1994: z > 13.5 km	10	0.0114 ± 0.0036	0.0184 ± 0.0044	0.0129	0.738

Table 4: Stratospheric aerosol optical thicknesses, from SAGE II observations. (Courtesy of Colette Brogniez, 1995.)

N	α	τ_a	$\varpi_a\, p_a(60°)$	$\varpi_a\, p_a(90°)$	$\varpi_a\, p_a(120°)$
45	1.251 ± 0.137	0.151 ± 0.044	0.676 ± 0.062	0.248 ± 0.027	0.162 ± 0.025
14	0.503 ± 0.057	0.094 ± 0.025	0.402 ± 0.066	0.141 ± 0.019	0.116 ±0.022
3	0.034 ± 0.029	0.409 ± 0.237	0.277 ± 0.192	0.148 ± 0.105	0.059 ± 0.039

Table 5: Summary of the three types of aerosols identified in the morning measurements. N is the number of measurements.

wavelength (nm)	$\Delta(\ln I_0)/m$	$\Delta\tau_r$	$\Delta(t_g)/m\ t_g$	$\Delta(S)/m\ S$	$\Delta\tau_a$
1020	0.0079	0.00016	-	0.0078	0.0111
870	0.0094	0.0030	-	-	0.0094
670	0.0164	0.00088	0.02	-	0.0259
440	0.0306	0.0048	-	-	0.0310

Table 6 a: Accuracy on the retrieval of aerosol optical thickness, $\Delta\tau_a$. The total error, $\Delta\tau_a$, is the quadratic sum of error resulting from the determination of the calibration coefficient, I_0, the Rayleigh optical thickness, ,τ_r, the ozone transmission, t_g, and the temperature correction in the 1020 nm band, S. Note that $\Delta\tau_a$ does not depend on the actual value of the optical thickness τ_a.

	$\tau_a = 0.03$	$\tau_a = 0.05$	$\tau_a = 0.1$	$\tau_a = 0.2$
$\Delta\rho_a\ /\ \rho_a(870)$	$9.2\ 10^{-2}$	$6.3\ 10^{-2}$	$4.1\ 10^{-2}$	$3.0\ 10^{-2}$
$\Delta\rho_a\ /\ \rho_a\ (1020)$	$6.4\ 10^{-2}$	$4.6\ 10^{-2}$	$3.3\ 10^{-2}$	$2.7\ 10^{-2}$
$\Delta\varepsilon\ /\ \varepsilon$	$15.6\ 10^{-2}$	$10.9\ 10^{-2}$	$7.4\ E10^{-2}$	$5.7\ 10^{-2}$

Table 6 b: Relative accuracy on the retrieval of the aerosol reflectance, ρ_a, at 870 and 1020 nm, and on its wavelength dependence $\varepsilon(870,1020)$. The scattering angle is 90°.

λ (nm)	τ_a = 0.03		τ_a = 0.05		τ_a = 0.1		τ_a = 0.2	
	A	B	A	B	A	B	A	B
870	0.43	+0.11	0.27	+0.12	0.15	+0.14	0.08	+0.17
1020	0.47	-0.04	0.29	-0.03	0.16	-0.01	0.09	+0.04

Table 6 c: Relative accuracy on the retrieval of the aerosol "pseudo" phase function for the model C70 for the scattering angle of 90°. Column A gives the relative error due to errors on aerosol optical thickness and aerosol reflectance. Column B gives the relative error due to the single scattering approximation.

τ_a	θ_s (°)	Aerosol model	R_n $\rho_s = 0$	R_n $\rho_s = 0.2$	Rel. error	R_n $\rho_s = 0.5$	Rel. error	R_n $\rho_s = 1.0$	Rel. error
0.1	39.90	T70	0.0176	0.0234	0.33	0.0322	0.83	0.0475	1.70
		M98	0.0089	0.0129	0.45	0.0189	1.13	0.0292	2.29
	62.17	T70	0.0126	0.0146	0.16	0.0176	0.40	0.0228	0.81
		M98	0.0064	0.0079	0.24	0.0100	0.57	0.0138	1.16
	80.72	T70	0.0097	0.0101	0.05	0.0108	0.12	0.0120	0.24
		M98	0.0053	0.0057	0.08	0.0063	0.19	0.0072	0.36
0.2	39.90	T70	0.0313	0.0406	0.30	0.0551	0.76	0.0810	1.59
		M98	0.0138	0.0198	0.44	0.0292	1.12	0.0456	2.31
	62.17	T70	0.0221	0.0251	0.14	0.0299	0.36	0.0382	0.73
		M98	0.0099	0.0119	0.21	0.0151	0.53	0.0206	1.08
	80.72	T70	0.0149	0.0156	0.05	0.0165	0.11	0.0183	0.23
		M98	0.0076	0.0081	0.07	0.0088	0.16	0.0101	0.33

Table 6 d: Computed normalized sky radiance, R_n, for different ground reflectances, ρ_s = 0, 0.2, 0.5, and 1, and a scattering angle of 90°.

τ_a	θ_s (°)	Aerosol model	R_n $\rho_s = 0$ V=0 ms^{-1}	R_n $\rho_s = 0$ V= 10 ms^{-1}	Rel. error
0.1	39.90	T70	0.0176	0.0186	0.06
		M98	0.0089	0.0097	0.09
	62.17	T70	0.0126	0.0137	0.09
		M98	0.0064	0.0076	0.19
	80.72	T70	0.0097	0.0116	0.20
		M98	0.0053	0.0068	0.28
0.2	39.90	T70	0.0313	0.0330	0.05
		M98	0.0138	0.0150	0.09
	62.17	T70	0.0221	0.0239	0.08
		M98	0.0099	0.0116	0.17
	80.72	T70	0.0149	0.0168	0.13
		M98	0.0076	0.0091	0.20

Table 6 e: Computed normalized sky radiance, R_n, for a ground reflectance, ρ_s, of zero, a scattering angle of 90°, and a wind speed, V, of 0 and 10 ms^{-1}.

Figure Captions

Fig. 1: "pseudo" phase function of aerosol models at 870 nm. a) maritime, urban, and continental models of WMO; b) models of Shettle and Fenn: T70, T98, M70 and M98.

Fig. 2: Spectral dependency of the aerosol reflectance between 870 and 1020 nm as a function of scattering angle. The aerosol reflectance is computed using the single scattering approximation. a) for five models of Shettle and Fenn: T70, T98, M70, M98, and C70; b) for maritime, urban, and continental models of WMO.

Fig. 3: Measured aerosol optical thickness versus wavelength for selected days.

Fig. 4: Actual and retrieved (using approximate Eqs. 14 and 17) "pseudo" phase functions at 870 nm, for models T70 and M98 with $\tau_a = 0.1$ and a) $\theta_s = 39.9°$, b) $\theta_s = 80.72°$.

Fig. 5: Histogram of the aerosol optical thickness at 870 nm, N, for data collected a) in 1993, b) in 1994 and c) in 1993 and 1994 after subtraction of the stratospheric component.

Fig. 6: Ångström coefficient versus aerosol optical thickness at 870 nm: measurements (crosses) collected in a) 1993 and b) 1994. The stratospheric component, given by SAGE data, is identified by a circle.

Fig. 7 a-c: Aerosol "pseudo" phase function at 870 nm versus Ångström coefficient: models of Shettle and Fenn (solid circles) and measurements (crosses) at a scattering angle of a) 60°, b) 90° and c) 120°.

Fig. 8 a-c: Aerosol reflectance spectral dependency $\varepsilon(870,1020)$ versus Ångström coefficient: models of Shettle and Fenn (solid circles) and measurements (crosses) for $\tau_a = 0.1$ and $\theta_s = 60°$, at a scattering angle of a) 60°, b) 90° and c) 120°.

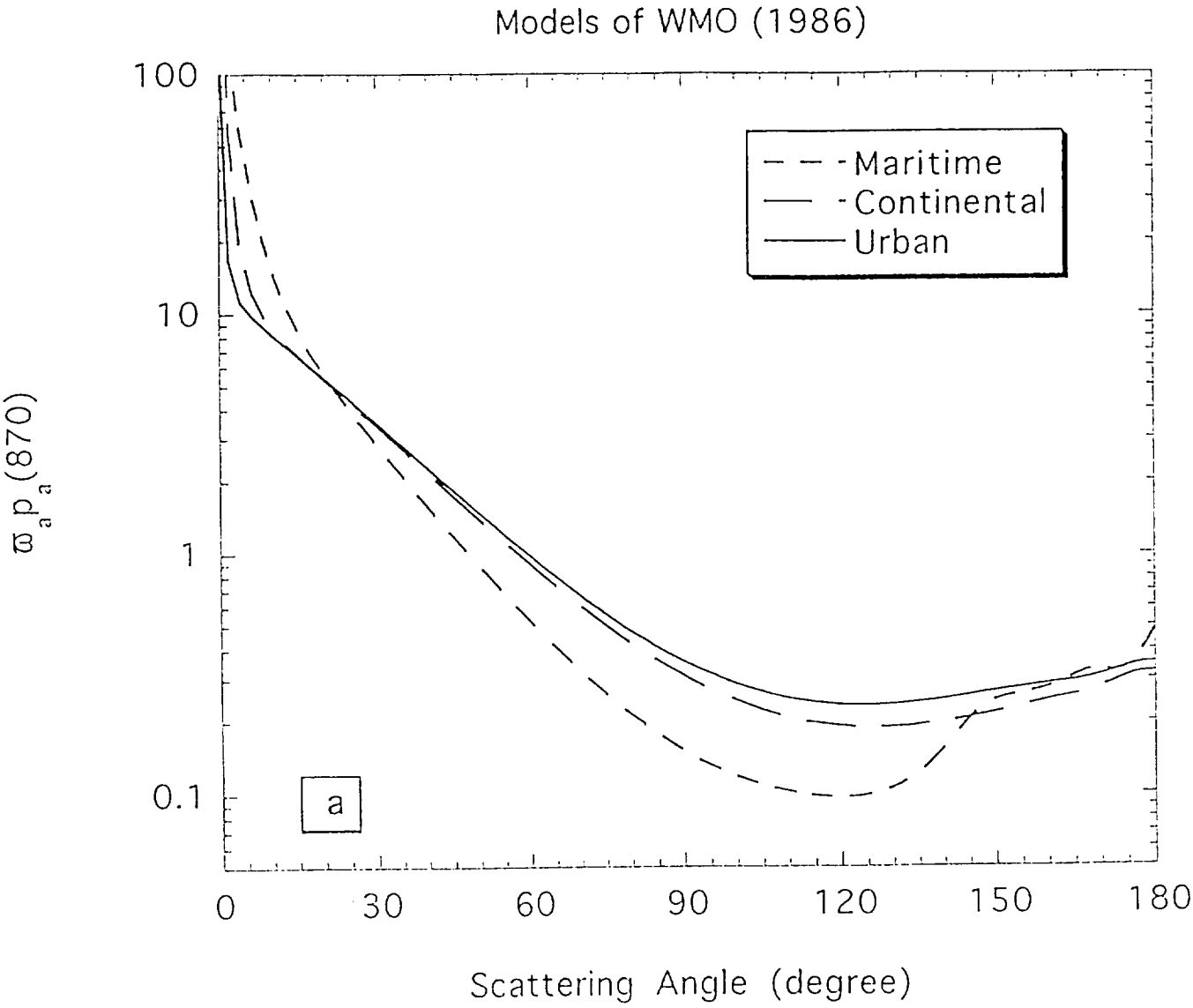
Models of WMO (1986)
100
10
1
0.1
$\varpi_a p_a(870)$
Maritime
Continental
Urban
a
0
30
60
90
120
150
180
Scattering Angle (degree)

Fig. 1a

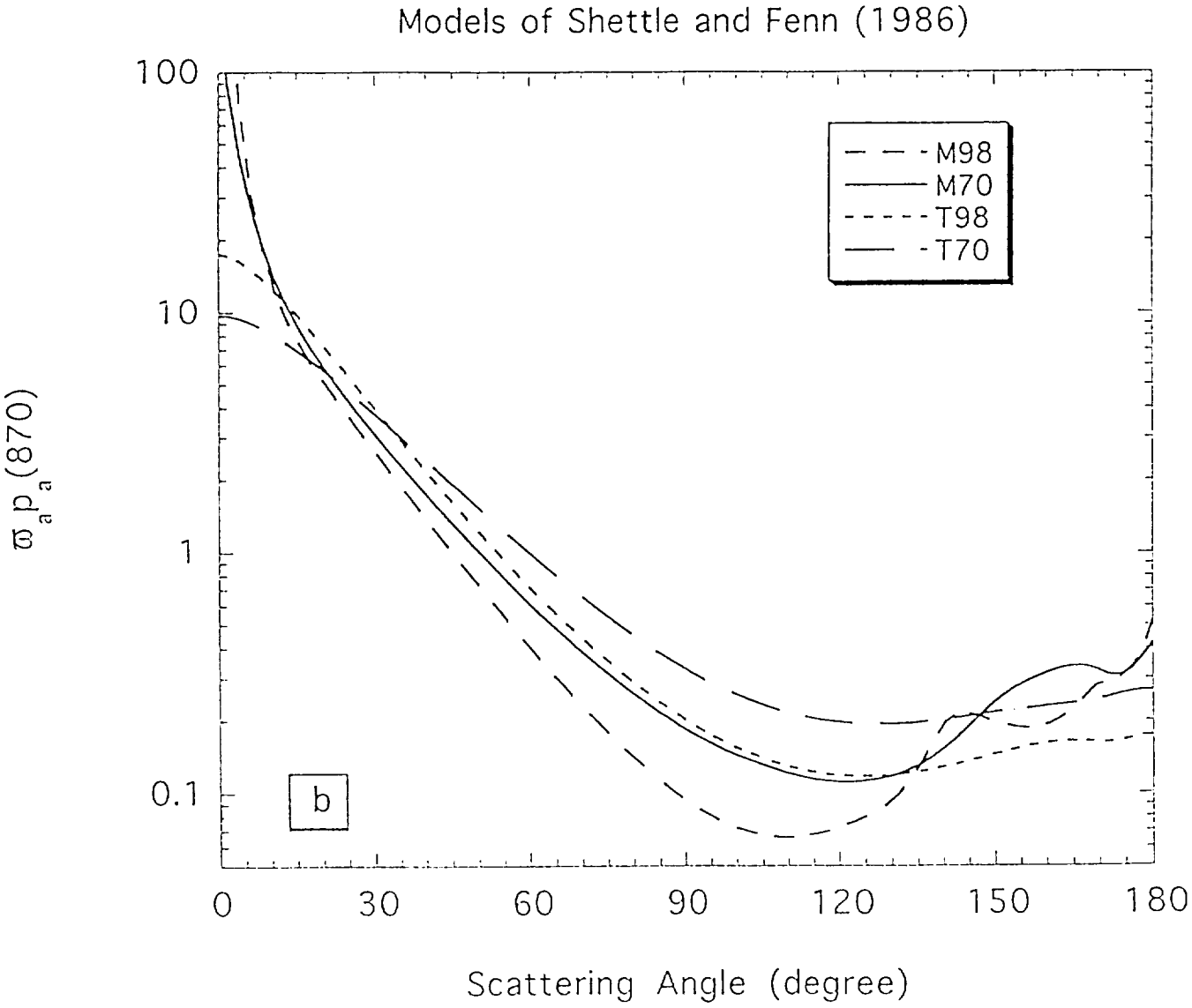
Models of Shettle and Fenn (1986)
100
10
1
0.1
$\varpi_a p_a(870)$
M98
M70
T98
T70
b
0
30
60
90
120
150
180
Scattering Angle (degree)

Fig. 1b

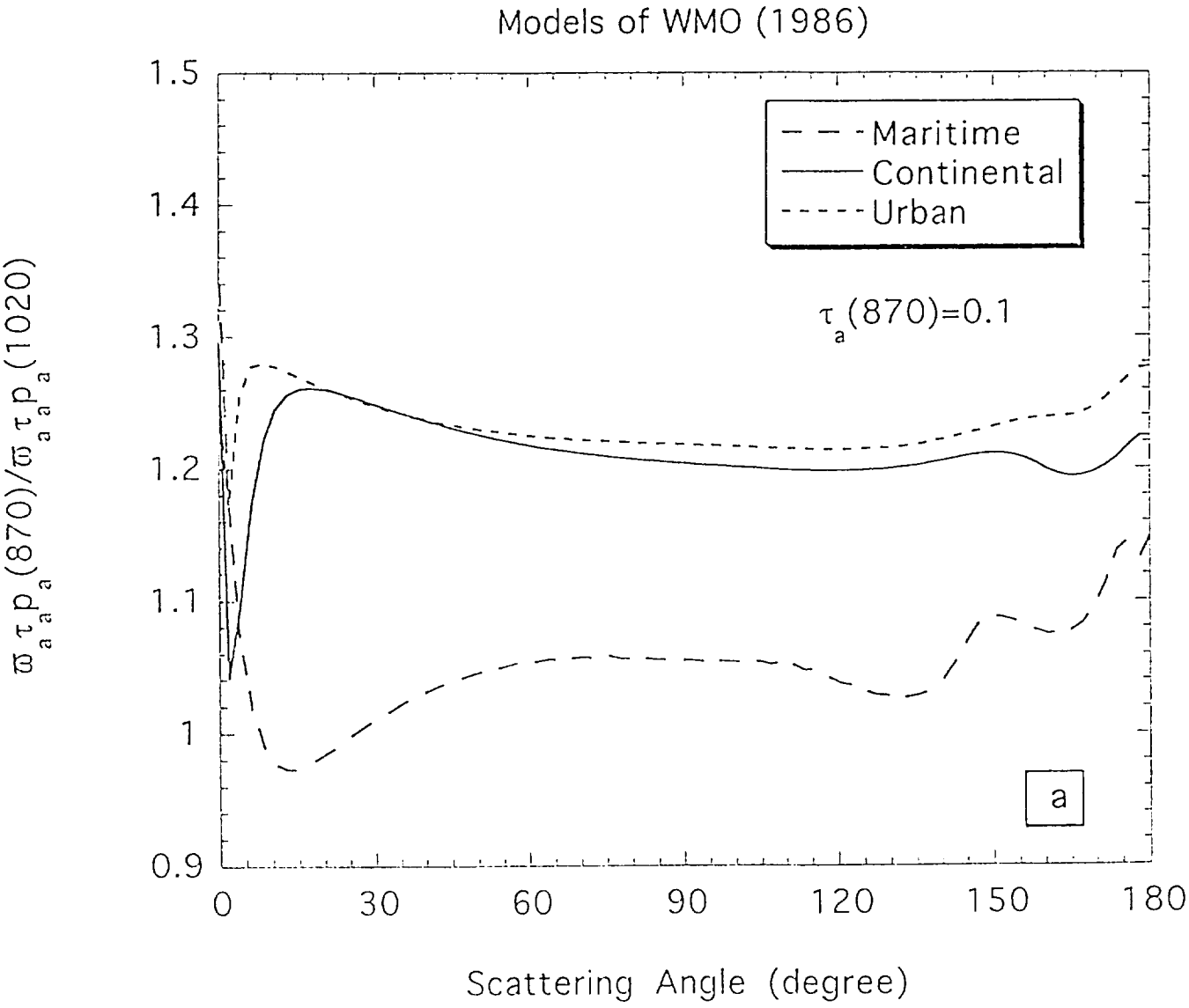
Models of WMO (1986)
Maritime
Continental
Urban
$\tau_a(870)=0.1$
a
1.5
1.4
1.3
1.2
1.1
1
0.9
0
30
60
90
120
150
180
$\varpi_{aa}\tau_a p_a(870)/\varpi_{aa}\tau_a p_a(1020)$
Scattering Angle (degree)

Fig. 2a

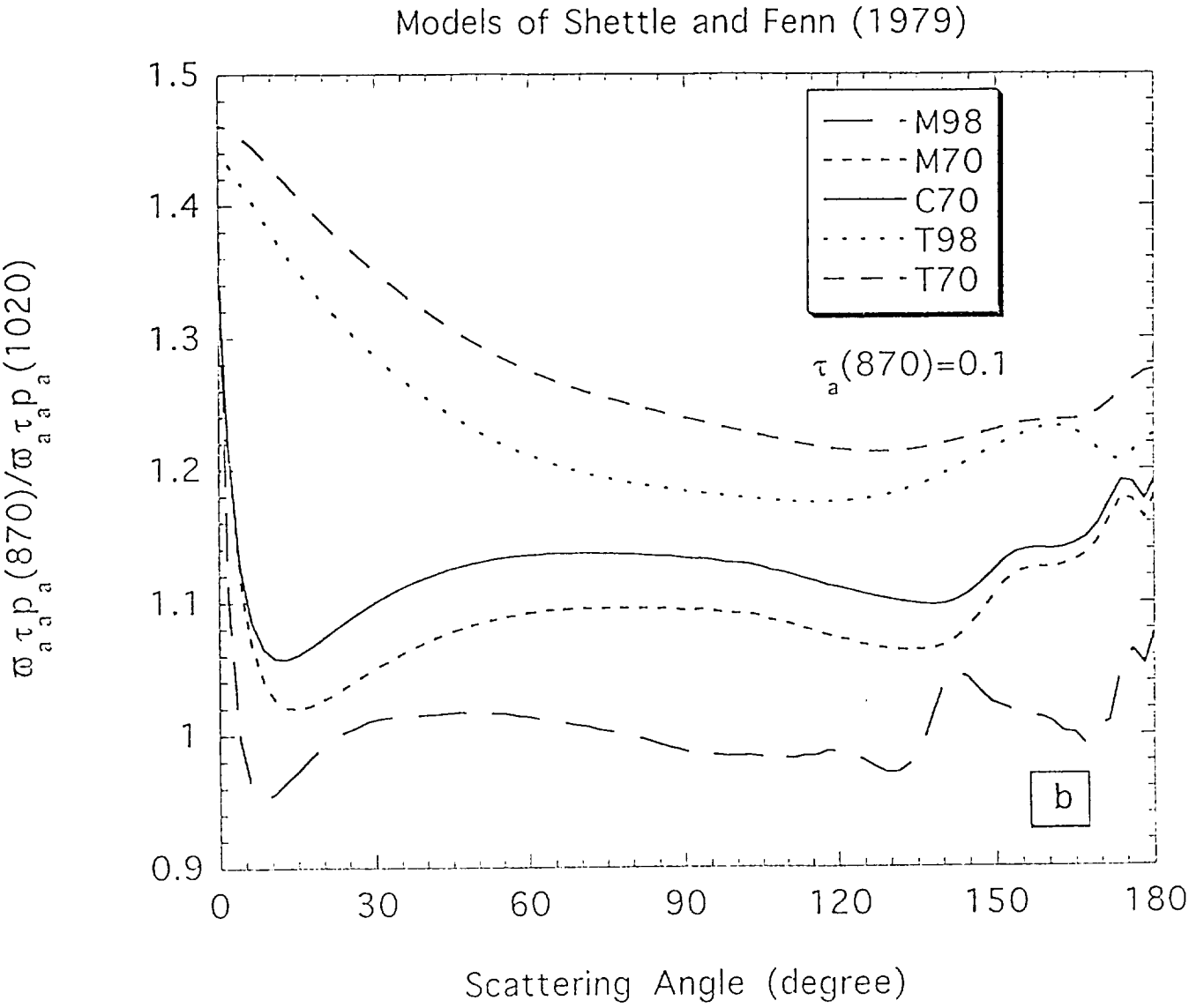
Models of Shettle and Fenn (1979)
M98
M70
C70
T98
T70
$\tau_a(870)=0.1$
b
1.5
1.4
1.3
1.2
1.1
1
0.9
0
30
60
90
120
150
180
Scattering Angle (degree)
$\omega_a \tau_a p_a(870)/\omega_a \tau_a p_a(1020)$

Fig. 2b

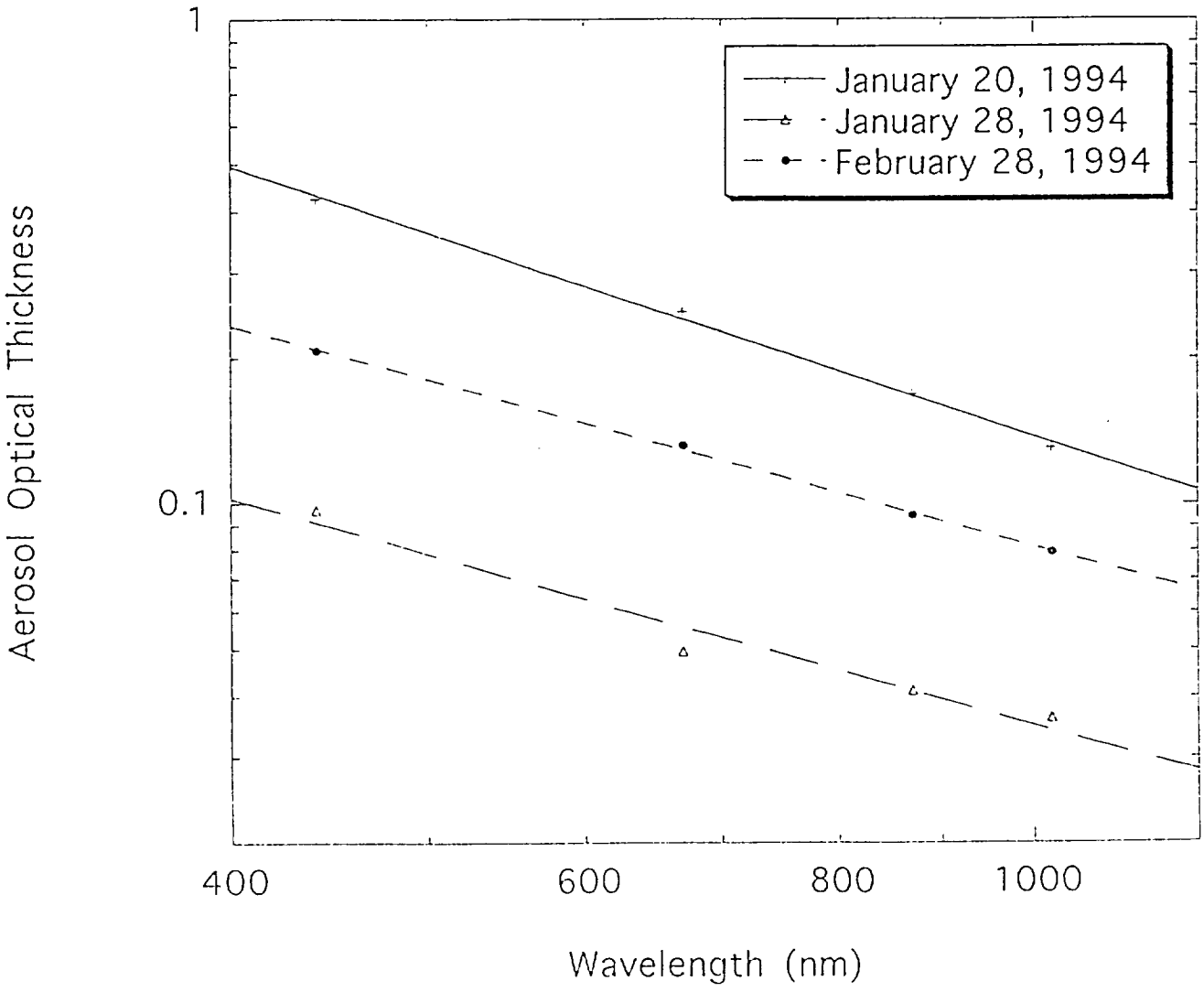
1
0.1
Aerosol Optical Thickness
January 20, 1994
January 28, 1994
February 28, 1994
400
600
800
1000
Wavelength (nm)

Fig. 3

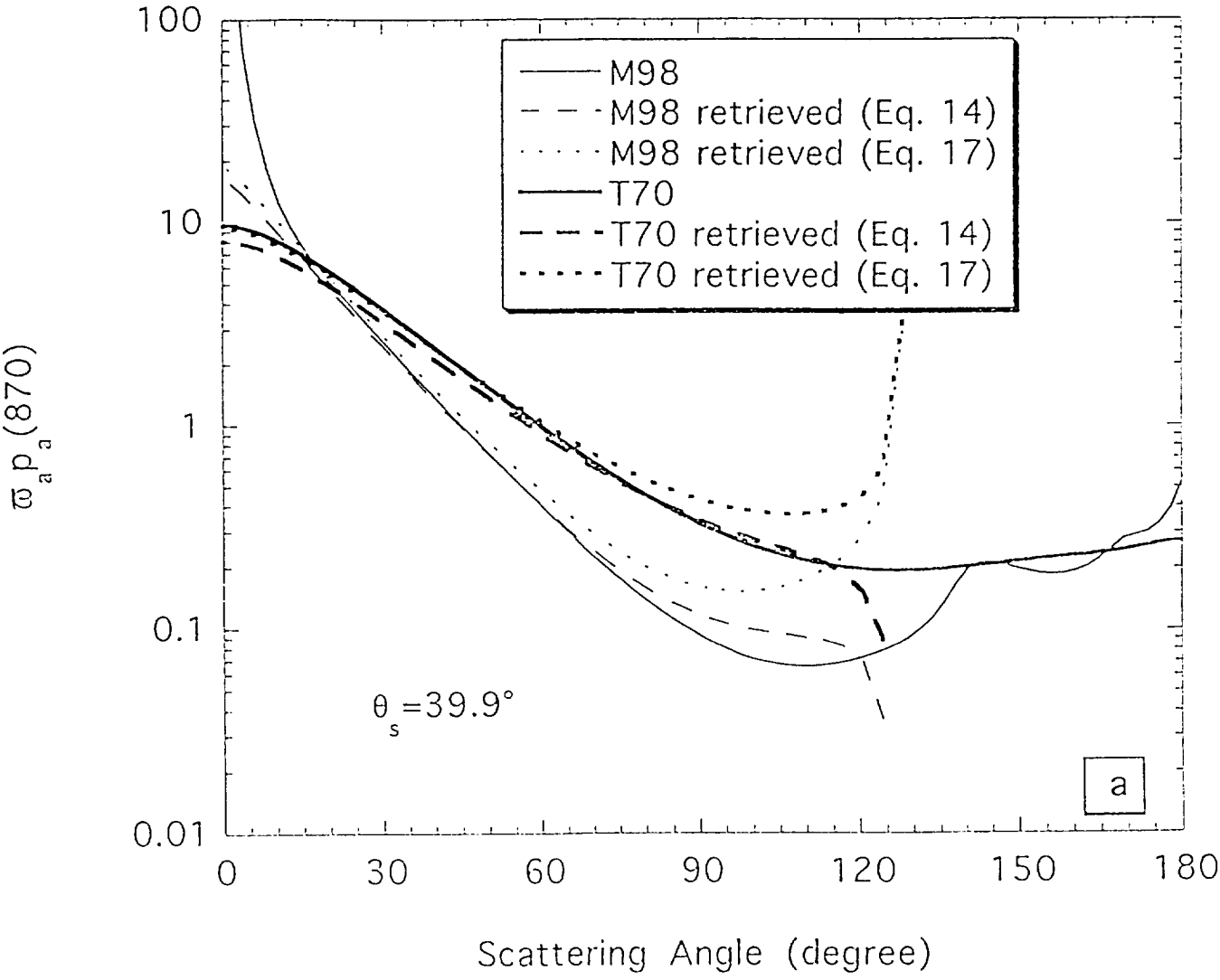
100
10
1
0.1
0.01
$\varpi_a p_a(870)$
M98
M98 retrieved (Eq. 14)
M98 retrieved (Eq. 17)
T70
T70 retrieved (Eq. 14)
T70 retrieved (Eq. 17)
θ_s=39.9°
a
0
30
60
90
120
150
180
Scattering Angle (degree)

Fig. 4a

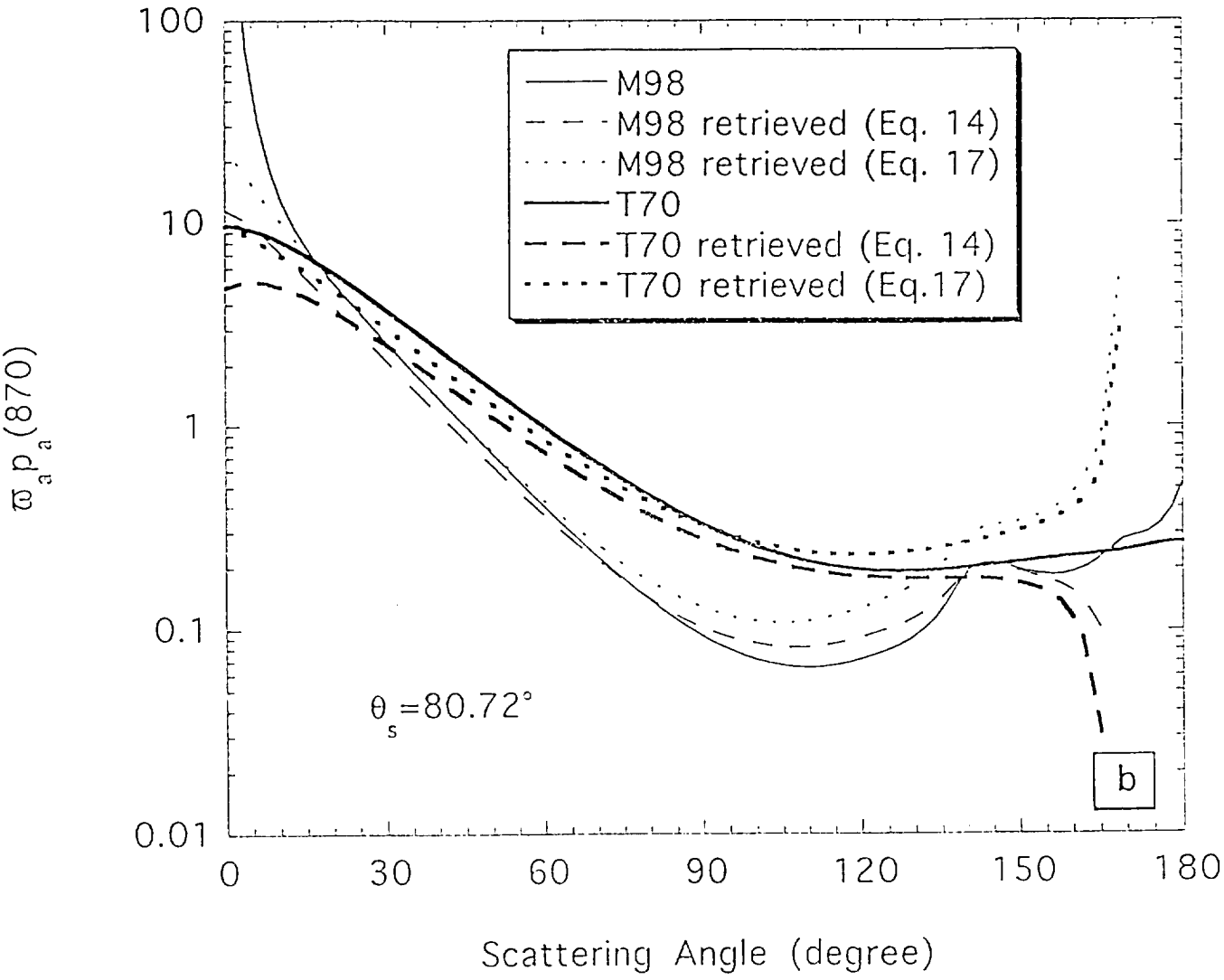
100
10
1
0.1
0.01
$\varpi_a p_a(870)$
M98
M98 retrieved (Eq. 14)
M98 retrieved (Eq. 17)
T70
T70 retrieved (Eq. 14)
T70 retrieved (Eq.17)
θ_s=80.72°
b
0
30
60
90
120
150
180
Scattering Angle (degree)

Fig. 4b

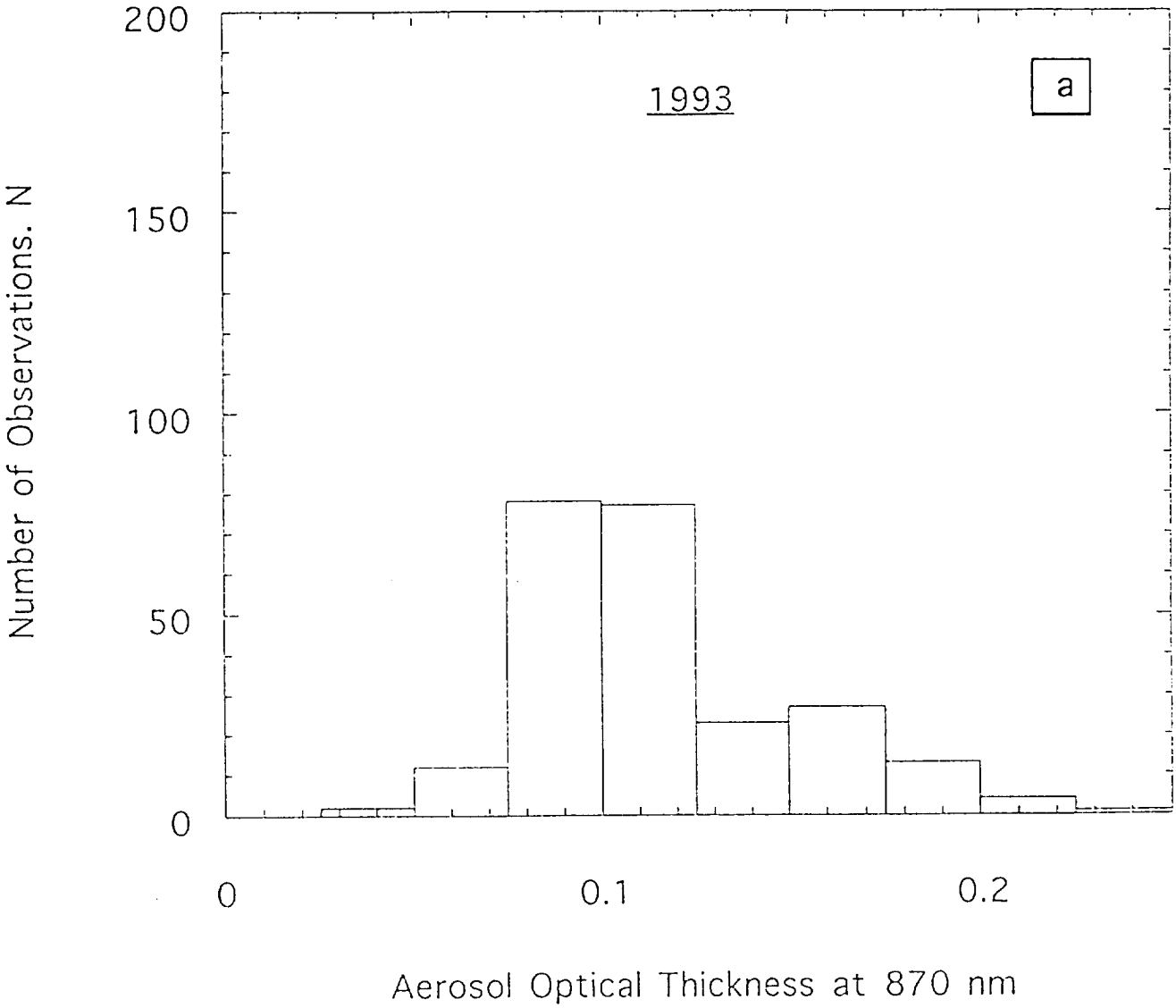
200
150
100
50
0
Number of Observations. N
1993
a
0
0.1
0.2
Aerosol Optical Thickness at 870 nm

Fig. 5a

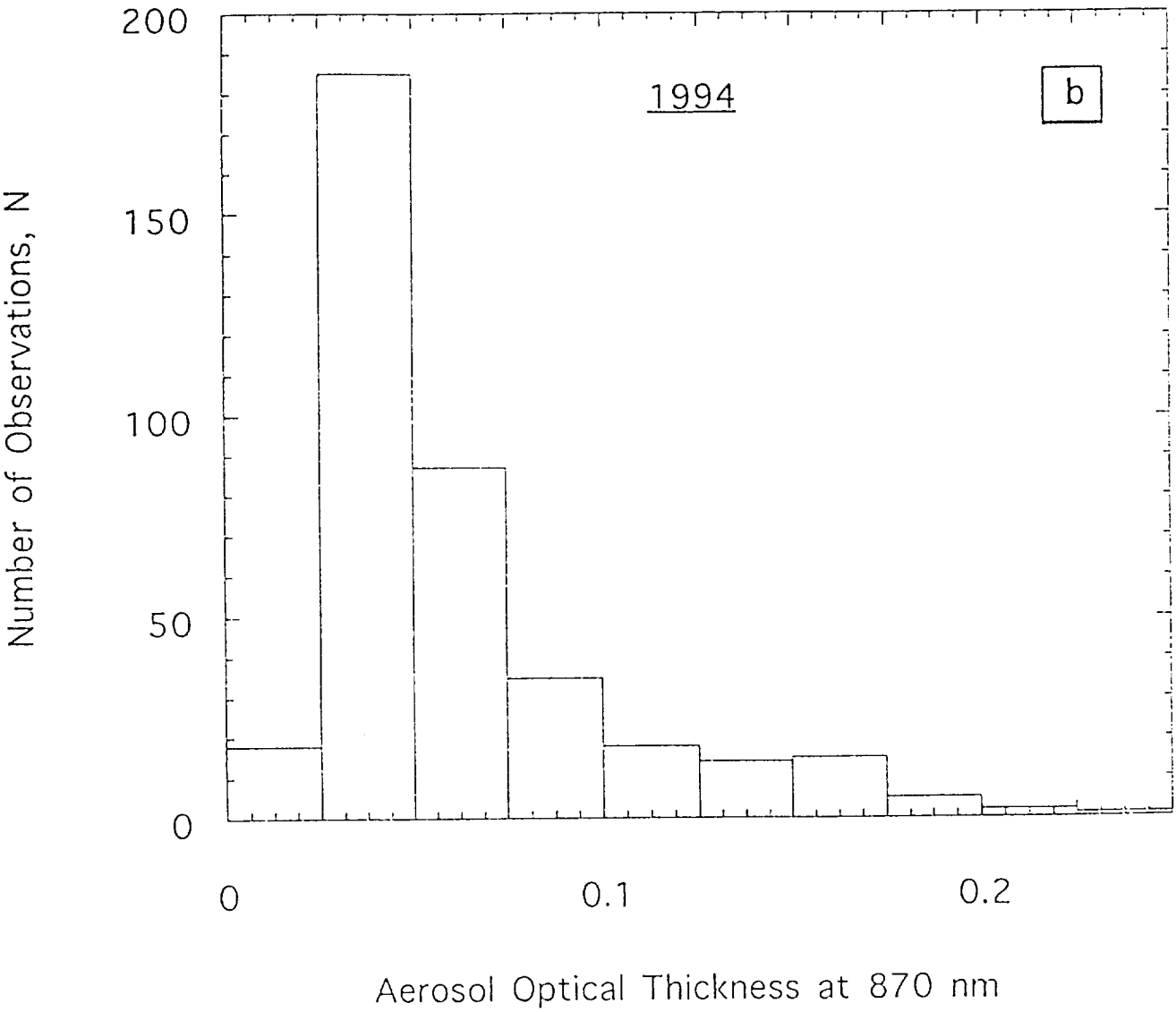
200
150
100
50
0
1994
b
Number of Observations, N
0
0.1
0.2
Aerosol Optical Thickness at 870 nm

Fig. 5b

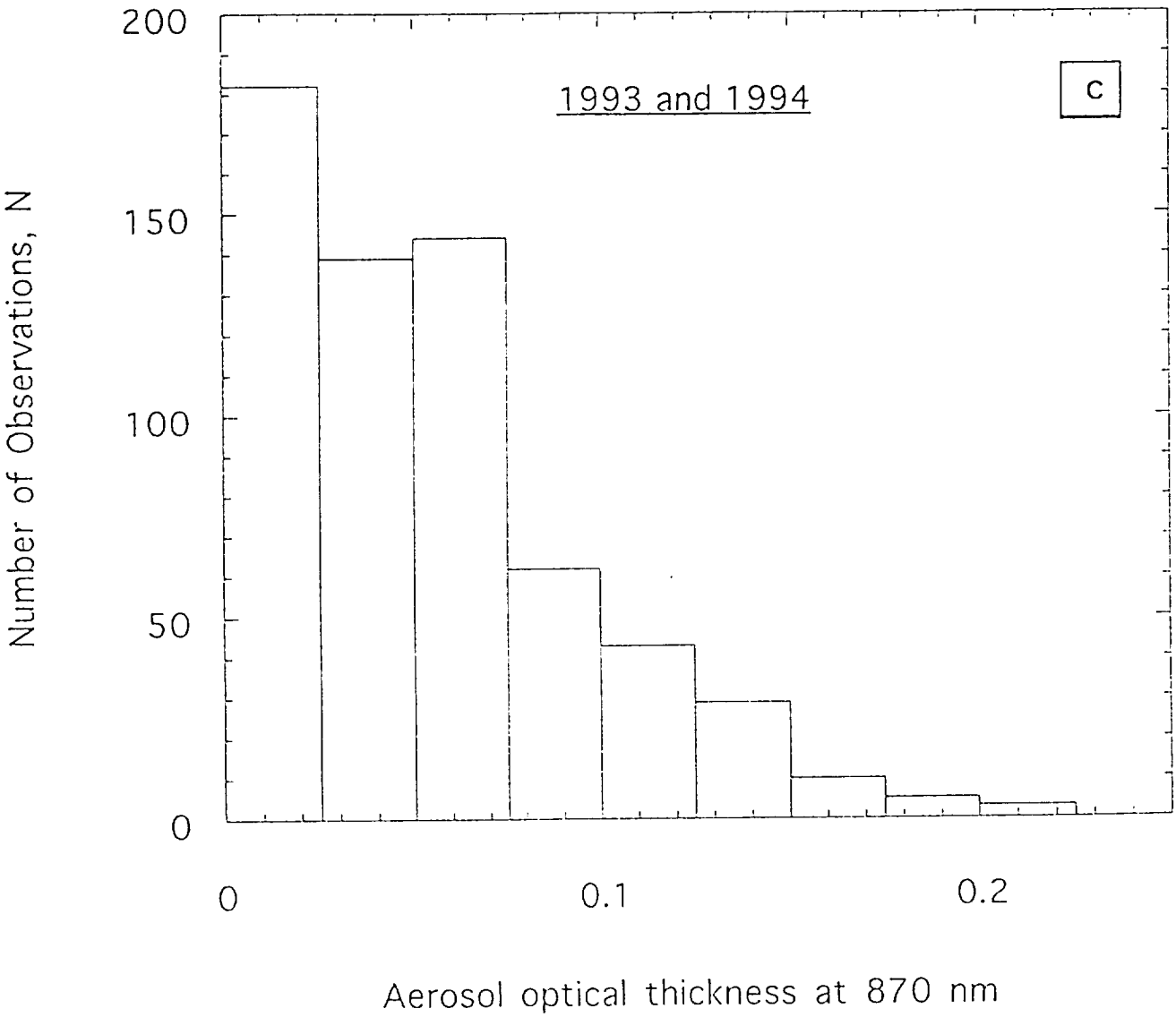
200
150
100
50
0
1993 and 1994
c
Number of Observations, N
0
0.1
0.2
Aerosol optical thickness at 870 nm

Fig. 5c

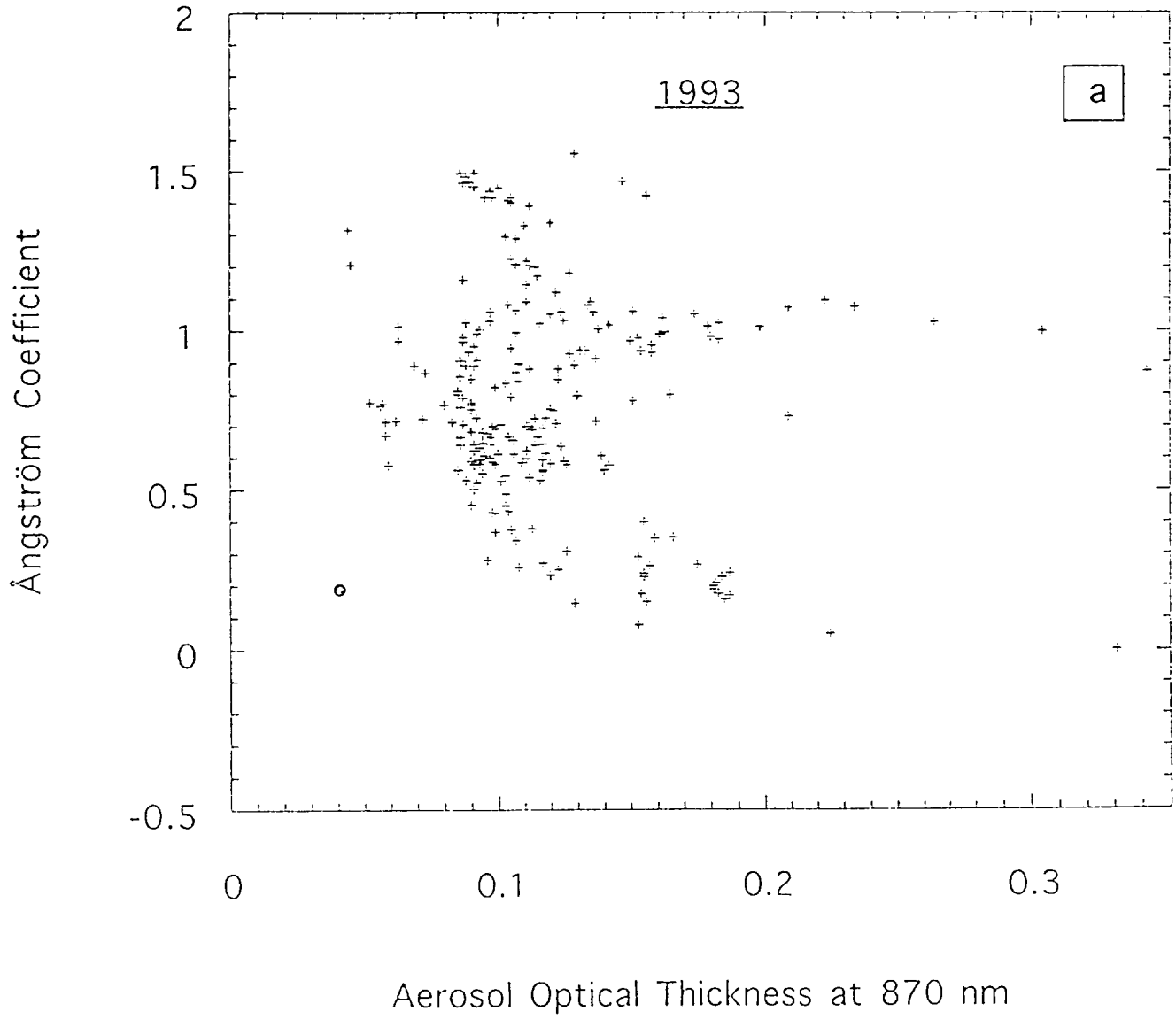
1993
a
Ångström Coefficient
2
1.5
1
0.5
0
-0.5
0
0.1
0.2
0.3
Aerosol Optical Thickness at 870 nm

Fig. 6a

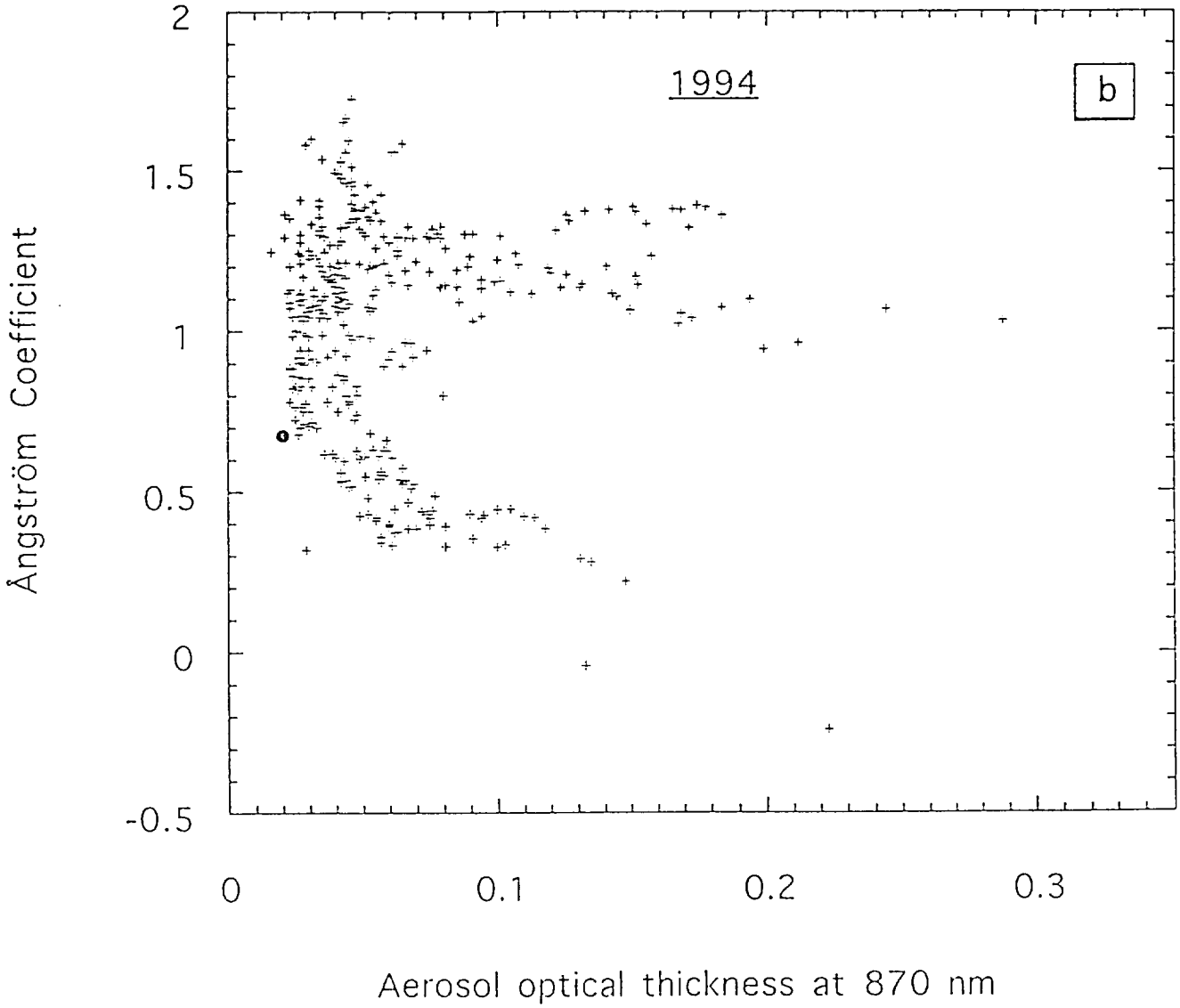
1994
b
2
1.5
1
0.5
0
-0.5
0
0.1
0.2
0.3
Ångström Coefficient
Aerosol optical thickness at 870 nm

Fig. 6b

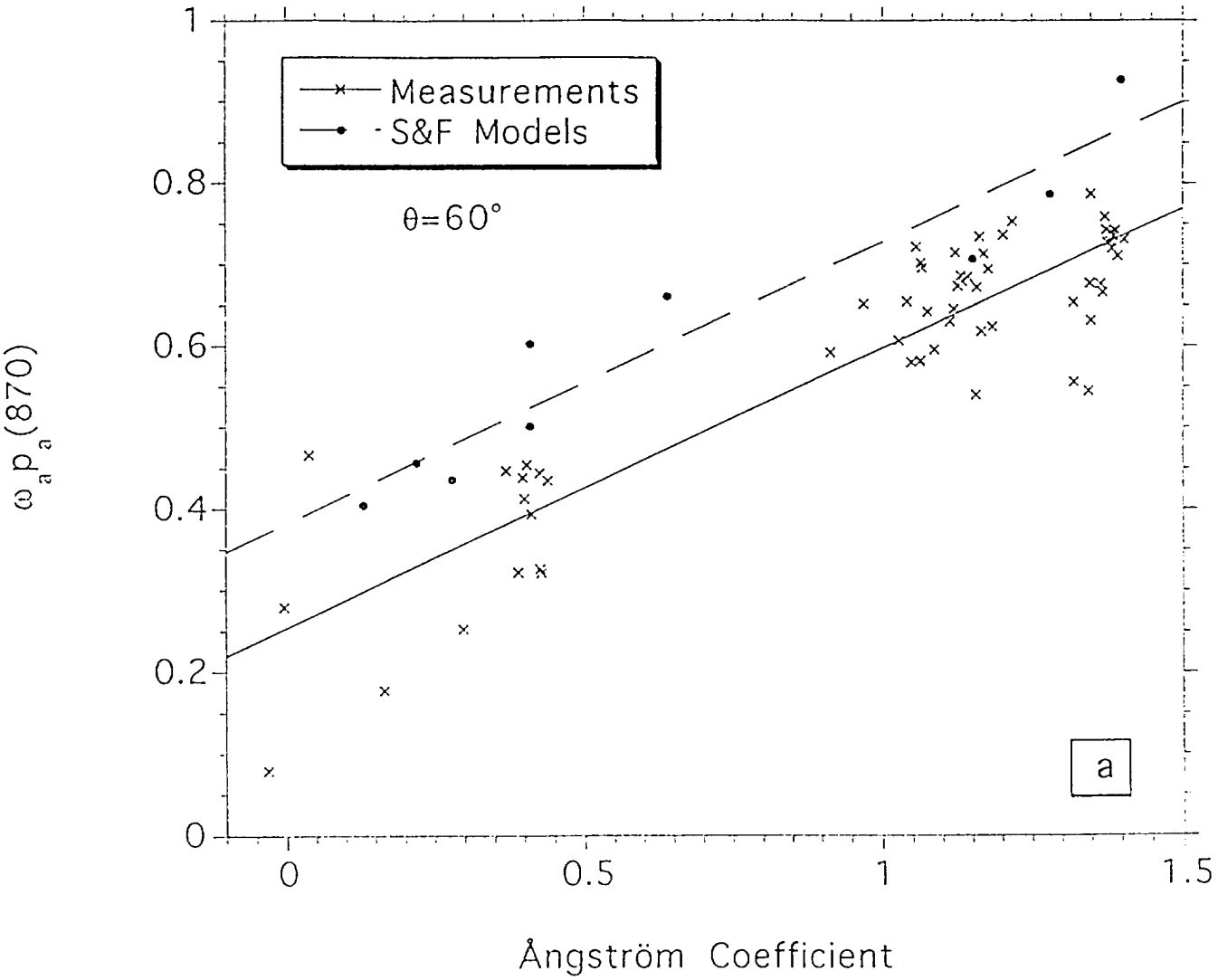
Measurements
S&F Models
θ=60°
a
1
0.8
0.6
0.4
0.2
0
0
0.5
1
1.5
$\omega_a p_a(870)$
Ångström Coefficient

Fig. 7a

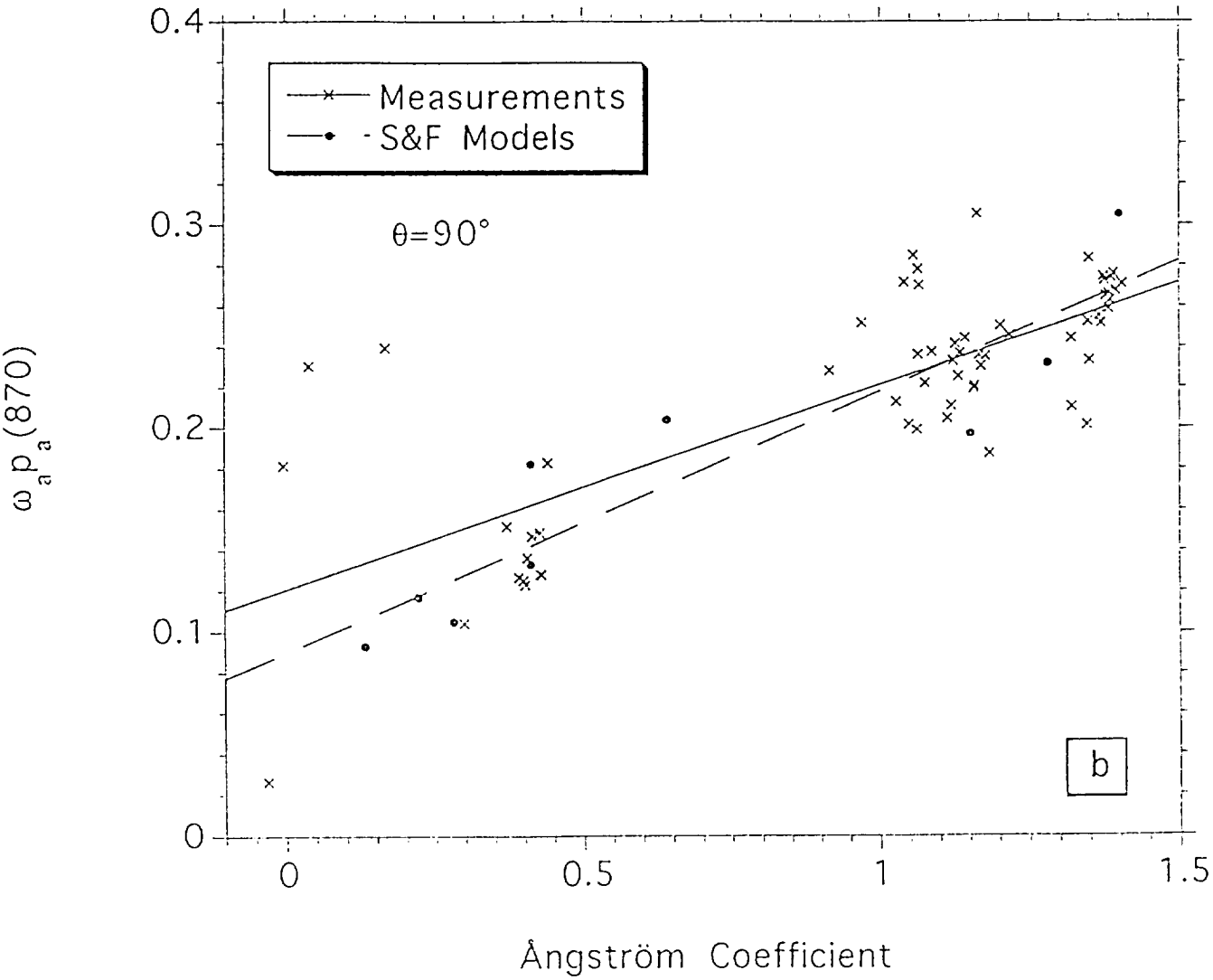
0.4
0.3
0.2
0.1
0
0
0.5
1
1.5
Measurements
S&F Models
θ=90°
b
$\omega_a p_a(870)$
Ångström Coefficient

Fig. 7b

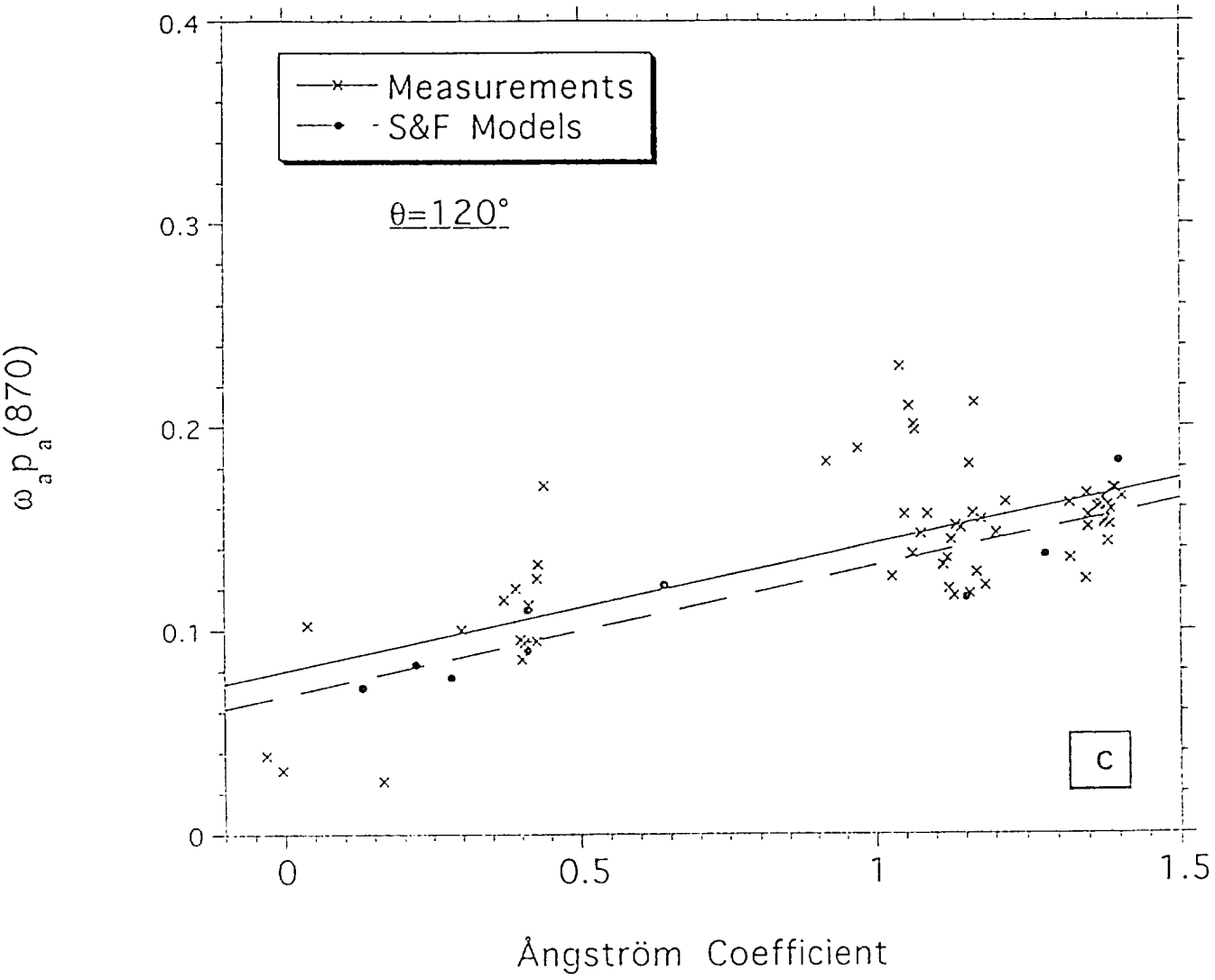
Measurements
S&F Models
θ=120°
c
0.4
0.3
0.2
0.1
0
0
0.5
1
1.5
$\omega_a p_a(870)$
Ångström Coefficient

Fig. 7c

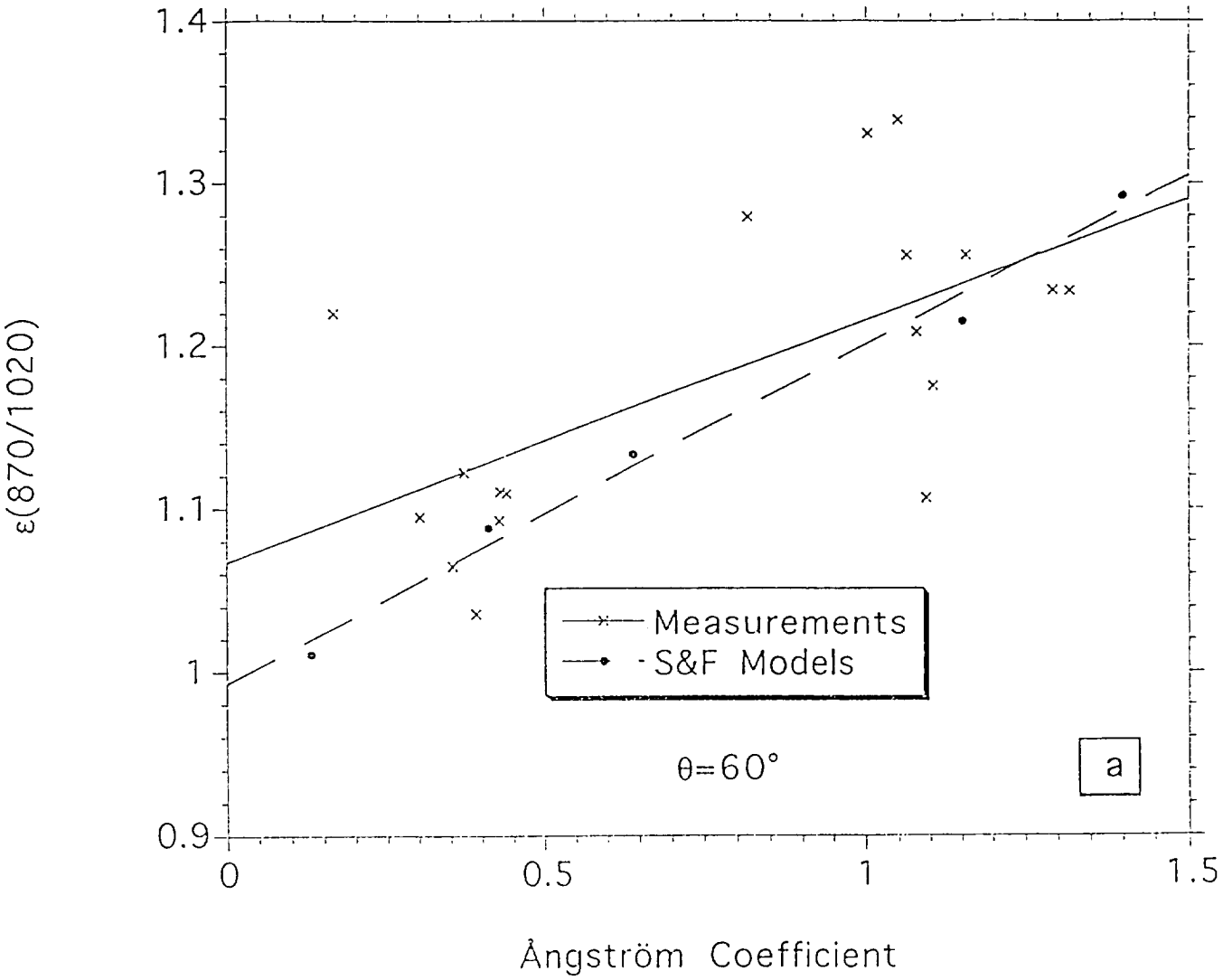
1.4
1.3
1.2
1.1
1
0.9
0
0.5
1
1.5
ε(870/1020)
Ångström Coefficient
Measurements
S&F Models
θ=60°
a

Fig. 8a

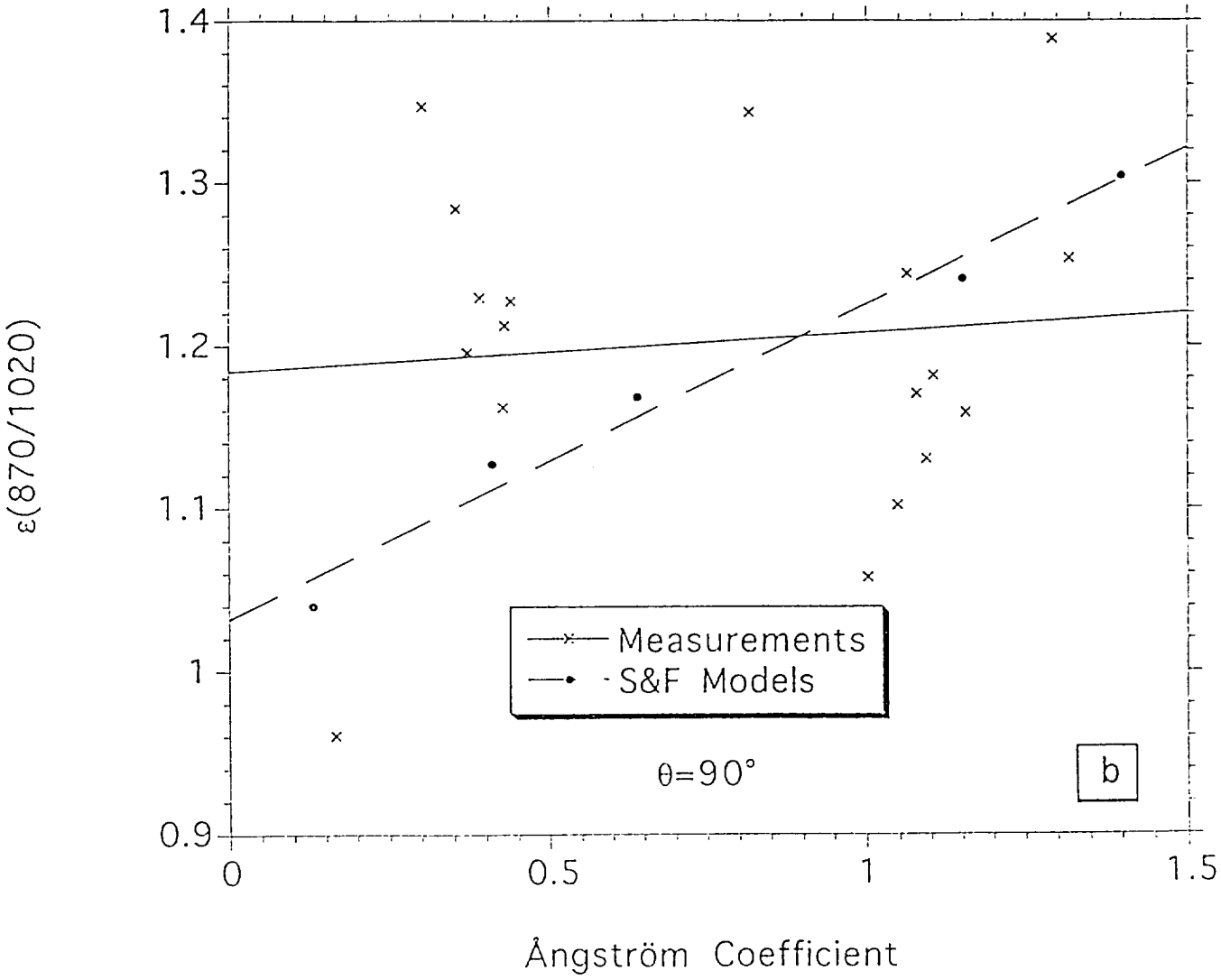
1.4
1.3
1.2
1.1
1
0.9
ε(870/1020)
0
0.5
1
1.5
Ångström Coefficient
Measurements
S&F Models
θ=90°
b

Fig. 8b

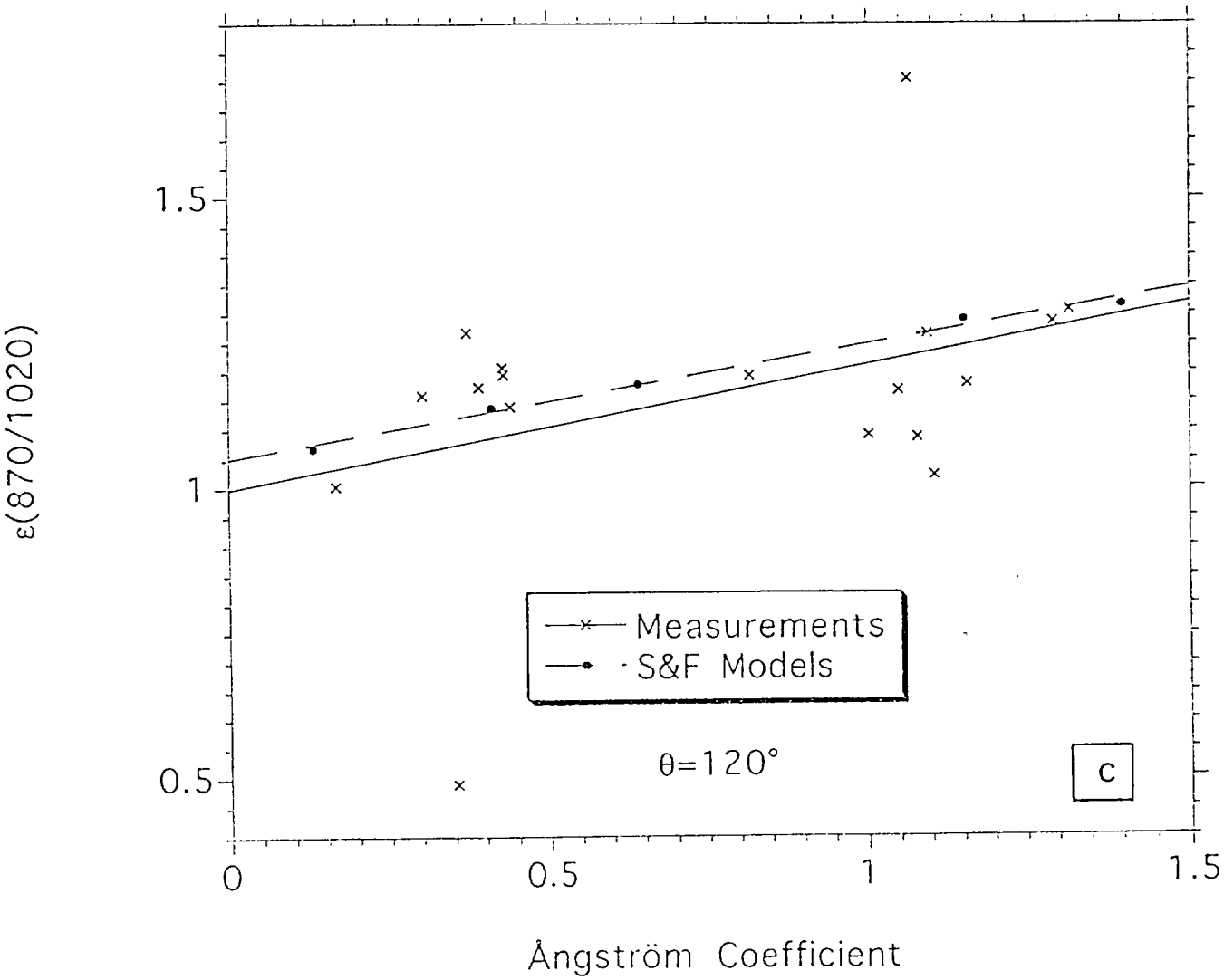
ε(870/1020)
1.5
1
0.5
0
0.5
1
1.5
Ångström Coefficient
Measurements
S&F Models
θ=120°
c

Fig. 8c